

# CANADIAN THESES ON MICROFICHE

I.S.B.N.

# THESES CANADIENNES SUR MICROFICHE



National Library of Canada  
Collections Development Branch

Canadian Theses on  
Microfiche Service

Ottawa, Canada  
K1A 0N4

Bibliothèque nationale du Canada  
Direction du développement des collections.

Service des thèses canadiennes  
sur microfiche.

## NOTICE

The quality of this microfiche is heavily dependent upon the quality of the original thesis submitted for microfilming. Every effort has been made to ensure the highest quality of reproduction possible.

If pages are missing, contact the university which granted the degree.

Some pages may have indistinct print especially if the original pages were typed with a poor typewriter ribbon or if the university sent us a poor photocopy.

Previously copyrighted materials (journal articles, published tests, etc.) are not filmed.

Reproduction in full or in part of this film is governed by the Canadian Copyright Act, R.S.C. 1970, c. C-30. Please read the authorization forms which accompany this thesis.

THIS DISSERTATION  
HAS BEEN MICROFILMED  
EXACTLY AS RECEIVED

## AVIS

La qualité de cette microfiche dépend grandement de la qualité de la thèse soumise au microfilmage. Nous avons tout fait pour assurer une qualité supérieure de reproduction.

S'il manque des pages, veuillez communiquer avec l'université qui a conféré le grade.

La qualité d'impression de certaines pages peut laisser à désirer, surtout si les pages originales ont été dactylographiées à l'aide d'un ruban usé ou si l'université nous a fait parvenir une photocopie de mauvaise qualité.

Les documents qui font déjà l'objet d'un droit d'auteur (articles de revue, examens publiés, etc.) ne sont pas microfilmés.

La reproduction, même partielle, de ce microfilm est soumise à la Loi canadienne sur le droit d'auteur, SRC 1970, c. C-30. Veuillez prendre connaissance des formules d'autorisation qui accompagnent cette thèse.

LA THÈSE A ÉTÉ  
MICROFILMÉE TELLE QUE  
NOUS L'AVONS REÇUE



National Library of Canada

Bibliothèque nationale du Canada

Canadian Theses Division

Division des thèses canadiennes

Ottawa, Canada  
K1A 0N4

67306

0-310-19398-0

### PERMISSION TO MICROFILM — AUTORISATION DE MICROFILMER

• Please print or type — Écrire en lettres moulées ou dactylographier

Full Name of Author — Nom complet de l'auteur

BOBAN KURIAKUSE JOHN

Date of Birth — Date de naissance

14 FEBRUARY 1957

Country of Birth — Lieu de naissance

INDIA

Permanent Address — Résidence fixe

VADARKAN HOUSE CHILAVANNCOR ROAD  
KADAVANTHRA P.O., COCHIN-20 INDIA - 682020

Title of Thesis — Titre de la thèse

Part I DENSITY MATRIX SIMULATION OF TWO-DIMENSIONAL AND  
MULTIPLE-PULSE NMR EXPERIMENTS

Part II NUCLEAR RELAXATION STUDY OF HEXAMETHYLPHOSPHURAMIDE

University — Université

UNIVERSITY OF ALBERTA, EDMONTON

Degree for which thesis was presented — Grade pour lequel cette thèse fut présentée

Ph.D. CHEMISTRY

Year this degree conferred — Année d'obtention de ce grade

1984

Name of Supervisor — Nom du directeur de thèse

PROF. R. E. D. McCLUNG

Permission is hereby granted to the NATIONAL LIBRARY OF CANADA to microfilm this thesis and to lend or sell copies of the film.

L'autorisation est, par la présente, accordée à la BIBLIOTHÈQUE NATIONALE DU CANADA de microfilmer cette thèse et de prêter ou de vendre des exemplaires du film.

The author reserves other publication rights, and neither the thesis nor extensive extracts from it may be printed or otherwise reproduced without the author's written permission.

L'auteur se réserve les autres droits de publication; ni la thèse ni de longs extraits de celle-ci ne doivent être imprimés ou autrement reproduits sans l'autorisation écrite de l'auteur.

Date

31 May 1984

Signature

THE UNIVERSITY OF ALBERTA

PART 1: DENSITY MATRIX SIMULATION OF TWO-DIMENSIONAL  
AND MULTIPLE-PULSE NMR EXPERIMENTS

PART 2: NUCLEAR RELAXATION STUDY OF  
HEXAMETHYLPHOSPHORAMIDE

by

BOBAN KURIAKOSE JOHN

A THESIS

SUBMITTED TO THE FACULTY OF GRADUATE STUDIES AND RESEARCH  
IN PARTIAL FULFILMENT OF THE REQUIREMENTS FOR THE DEGREE  
DOCTOR OF PHILOSOPHY

DEPARTMENT OF CHEMISTRY

EDMONTON, ALBERTA

FALL, 1984

T H E U N I V E R S I T Y O F A L B E R T A

RELEASE FORM

NAME OF AUTHOR BOBAN KURIAKOSE JOHN

TITLE OF THESIS PART 1: DENSITY MATRIX SIMULATION OF TWO-  
DIMENSIONAL AND MULTIPLE-PULSE,  
NMR EXPERIMENTS.

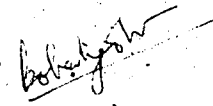
PART 2: NUCLEAR RELAXATION STUDY OF  
HEXAMETHYLPHOSPHORAMIDE

DEGREE FOR WHICH THESIS WAS PRESENTED Ph.D..

YEAR THIS DEGREE GRANTED 1984.

Permission is hereby granted to THE UNIVERSITY OF  
ALBERTA LIBRARY to reproduce single copies of this  
thesis and to lend or sell such copies for private,  
scholarly or scientific research purposes only.

The author reserves other publication rights, and  
neither the thesis nor extensive extracts from it may  
be printed or otherwise reproduced without the author's  
written permission.

  
(Signed)

PERMANENT ADDRESS:


Vadakkan House  
Chilavannoor Road  
Kadavanthra P.O.  
Cochin-20, INDIA-682020

DATED

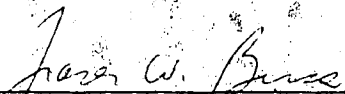
May 17, 1984.

THE UNIVERSITY OF ALBERTA  
FACULTY OF GRADUATE STUDIES AND RESEARCH

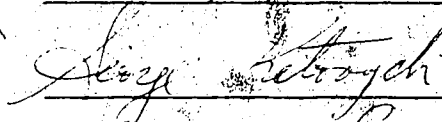
The undersigned certify that they have read, and recommend to the Faculty of Graduate Studies and Research, for acceptance, a thesis entitled PART 1: DENSITY MATRIX SIMULATION OF TWO-DIMENSIONAL AND MULTIPLE-PULSE NMR EXPERIMENTS; PART 2: NUCLEAR RELAXATION STUDY OF HEXA METHYL PHOSPHORAMIDE submitted by BOBAN KURIAKOSE JOHN in partial fulfilment of the requirements for the degree of DOCTOR OF PHILOSOPHY.

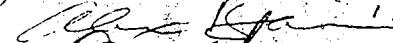


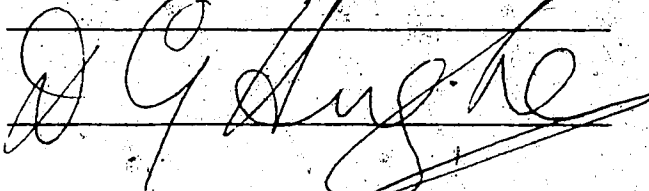
Supervisor











DATE May 17, 1984.

TO MY LOVED ONES

---

## ABSTRACT

This thesis consists of two parts:

Part 1: Density Matrix Simulation of Two-Dimensional and Multiple-Pulse Experiments

A simulation program to analyze multiple-pulse and two-dimensional FT NMR experiments using density matrix theory has been implemented. The program computes analytical expressions for NMR signals arising from an  $I_m S_n$  spin system (where I and S are spin 1/2 nuclei and  $1 < n, m < 3$ ), after the application of a pulse sequence specified by the input data. The simulation program has been designed to be quite general and incorporates a number of features including irradiation from a broadband decoupler, effects of phase cycling of the pulses and receiver, and pulses of any given flip angle.

The state of a spin system during a multiple-pulse experiment is followed by monitoring the evolution of the density matrix. During each step in the sequence, the effective Hamiltonian operator will be time independent in a suitable rotating frame, and the equation of motion for the density matrix in this frame can be solved in a straightforward manner. The evolution of the density matrix through a pulse sequence is thereby reduced to a series of successive transformations on the density

matrix. The simulation program has been implemented in such a manner that the transformations of the density matrix, under radiofrequency pulses, free-precession periods, periods of broadband decoupling, etc., are effected by various independent program modules which have access to the density matrix data structure.

A detailed investigation of the effects of ordinary noise decoupling and spherical randomization decoupling on the elements of the density matrix for  $I_m S_n$  spin systems has been carried out. It has been shown that under strong decoupler irradiation, the density matrix elements reach steady state values in the rotating frame of the decoupled nuclei. The steady state values are found to be linear combinations of the density matrix at the beginning of the decoupling period, and often involve mixing of populations with multiple quantum coherences, and mixing of the perpendicular components of the magnetization with higher coherences. The transformation of the density matrix during the decoupling period is carried out by the linear combination procedure using coefficients stored in the program.

The application of the program in the analysis of multiple-pulse and two-dimensional experiments has been demonstrated by simulating the distortionless enhanced polarization transfer (DEPT) experiment, a two-dimensional



version of the DEPT experiment for multiplet-selective heteronuclear shift correlation, the INADEQUATE experiment and three variants of the gated decoupler 2D J- $\delta$  resolved experiment which illustrate certain unexpected effects of spin decoupling. These examples demonstrate the usefulness of the program in simulating experiments in which the spin dynamics cannot always be followed using classical magnetization vector diagrams.

Part 2: Nuclear Relaxation Study of Hexamethyl-  
Phosphoramidate

The spin-lattice relaxation times of  $^{31}\text{P}$ ,  $^{14}\text{N}$  and  $^1\text{H}$  in hexamethylphosphoramidate (HMPA) and of  $^{31}\text{P}$  and  $^2\text{H}$  in the deuterated analog (HMPD) have been measured over the temperature range 290 K - 450 K. The relaxation of the  $^{31}\text{P}$  nucleus in HMPD has been assumed to be entirely due to spin-rotation interactions and the angular momentum correlation time ( $\tau_J$ ) has been determined. It has been found that the quadrupolar interaction in  $^{14}\text{N}$  in HMPA is modulated by a time dependence characterized by two correlation times: the overall molecular tumbling correlation time ( $\tau_\theta$ ) and that for the internal rotation about the P-N bond ( $\tau_i^{\text{PN}}$ ).  $\tau_\theta$  was determined using the Hubbard relation with  $\tau_J$  obtained from the  $^{31}\text{P}$  data in HMPD.  $\tau_i^{\text{PN}}$  has been determined from the  $^{14}\text{N}$  data. The

activation energy for the internal motion was found to be  $3.4 \pm 0.2$  kcal/mole.

The relaxation rate of  $^2\text{H}$  in HMPD was found to be governed by three correlation times:  $\tau_0$ ,  $\tau_1^{\text{PN}}$  and that for the rotation of  $\text{CD}_3$  groups ( $\tau_1^{\text{CN}}$ ). The rotation of  $\text{CD}_3$  groups was found to possess a relatively high activation energy  $3.0 \pm 0.1$  kcal/mole. The delineation of the contributions to the relaxation rate of  $^{31}\text{P}$  in HMPA was carried out using the above results and data from the temperature studies of the diffusion coefficient of HMPA.

## ACKNOWLEDGEMENTS

I take this opportunity to express my deep gratitude to Professor R.E.D. McClung for his guidance and enthusiasm during the course of this work. He has patiently spent countless hours leading me through the rough terrain of density matrix and spin relaxation theories.

I owe special gratitude to Dr. T.T. Nakashima for many stimulating discussions and collaboration in many experiments.

I am also grateful to Professor R.B. Jordan for his help with instrumentation and experimental aspects.

I thank Dr. J. Ripmeester for measuring the  $^1\text{H}$  NMR spectrum of solid hexamethylphosphoramide.

Special thanks are due to Annabelle Wiseman for her expert help in typing this manuscript.

To all my friends, I express my sincere appreciation, especially to Dipak Ghosh and Swapan Chowdhury for their continuous support.

Financial assistance from the Department of Chemistry and Natural Science and Engineering Research Council of Canada is gratefully acknowledged. 7

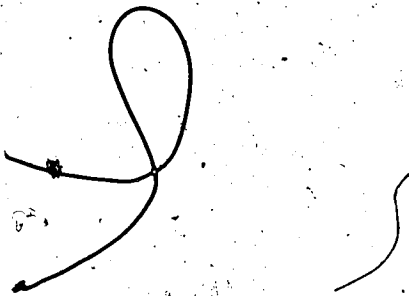


TABLE OF CONTENTS

CHAPTER	PAGE
PART 1: DENSITY MATRIX SIMULATION OF TWO-DIMENSIONAL AND MULTIPLE-PULSE NMR EXPERIMENTS.....	1
I. APPLICATION OF DENSITY MATRIX THEORY IN PULSED FT NMR .....	2
I.1 Introduction.....	2
I.2 Definition of Density Matrix and Equations for Physical Observables.....	3
I.3 Equation of Motion of the Density Matrix.....	5
I.4 Rotating Frame Transformation.....	7
I.5 Inclusion of Relaxation Effects and Chemical Exchange.....	12
I.6 Density Matrix Method and Bloch Equations Approach.....	14
I.7 Applications to Pulsed FT NMR.....	17
I.8 Analysis of a Simple FT Experiment.....	22
I.9 Summary.....	28
II. DESCRIPTION OF THE SIMULATION PROGRAM.....	30
II.1 Introduction.....	30
II.2 Objectives of the Simulation Program....	31

CHAPTER		PAGE
II.3	Implementation of the Simulation Program.....	33
	a. Description of Input Commands.....	39
II.4	Choice of Basis Set.....	49
II.5	Construction of Spin Operator Representation Matrices.....	50
II.6	Computation of the Thermal Equilibrium Density Matrix.....	53
II.7	Transformation of the Density Matrix by rf Pulse Operators.....	55
II.8	Transformation of the Density Matrix During Free Precession Periods.....	61
II.9	Transformation of Density Matrix During Broad-Band Decoupling.....	62
II.10	Computation and Simplification of Signal Expressions.....	63
II.11	Identification of $\nu_I$ and $\nu_S$ as Frequency Offsets from Transmitter.....	66
II.12	Other Features of the Simulation Program.....	75
II.13	Limitations of and Suggested Extensions to the Simulation Program.....	76
II.14	Summary.....	78

CHAPTER	PAGE
III. THEORY AND IMPLEMENTATION OF THE HETERONUCLEAR NOISE DECOUPLING SCHEME.....	80
III.1 Introduction.....	80
III.2 Theoretical Treatment.....	81
a. IS <sub>2</sub> Spin System.....	83
b. IS and IS <sub>3</sub> Spin Systems.....	91
c. Spherical Randomization Decoupling..	95
III.3 General Effects of Noise Decoupling on the Density Matrix.....	100
III.4 Implementation of the Decoupling Scheme.....	102
III.5 Summary.....	104
IV. APPLICATIONS.....	106
IV.1 Introduction.....	106
IV.2 Simulation of Experiments.....	107
a. DEPT Experiment.....	107
b. Selective 2D Heteronuclear Shift Correlation Experiment.....	130
c. INADEQUATE Experiment.....	140
d. Unexpected Effects of Spin Decoupling.....	149
IV.3 Summary.....	174

CHAPTER	PAGE
PART 2: NUCLEAR RELAXATION STUDY OF HEXAMETHYL- PHOSPHORAMIDE.....	176
V. DESCRIPTION OF SPIN RELAXATION MECHANISMS.....	177
V.1 Introduction.....	177
V.2 Spin Relaxation and Applications of Relaxation Studies.....	177
V.3 Spin Relaxation Mechanisms.....	182
a. Dipolar Interactions.....	184
1. Random Rotation.....	186
2. Translational Motion.....	188
b. Spin-Rotation Interaction.....	189
c. Nuclear Quadrupole Interaction.....	191
V.4 Brief Review of Rotational Diffusion Models.....	193
V.5 Objectives of the Project.....	198
V.6 Summary.....	199
VI. EXPERIMENTAL.....	200
VI.1 Introduction.....	200
VI.2 Sample Preparation.....	200
VI.3 Instrumentation.....	201
VI.4 Measurement of $T_1$ Relaxation Time.....	204
a. Inversion Recovery Experiment.....	204
b. Triplet Sequence.....	205

CHAPTER		PAGE
VI.5	Measurement of Translational Diffusion Coefficients.....	207
VI.6	Summary.....	211
VII.	RESULTS AND DISCUSSION.....	212
VII.1	Introduction.....	212
VII.2	$^{31}\text{P}$ $T_1$ (HMPD) Results and Analysis.....	212
VII.3	$^{14}\text{N}$ $T_1$ Results and Analysis.....	221
VII.4	$^2\text{H}$ $T_1$ Results and Analysis.....	230
VII.5 <sup>a</sup>	$^{31}\text{P}$ $T_1$ (HMPA) Results and Analysis.....	236
	a. Calculation of Spin-Rotation Relaxation Rates.....	239
	b. Calculation of Intermolecular Dipolar Relaxation Rates.....	241
	c. Calculation of the Intramolecular Dipole Relaxation Rates.....	243
	d. Comparison of Calculated and Experimental Relaxation Rates.....	244
VII.6	Conclusions.....	246
VII.7	Summary.....	249

\*\*\*\*\*

REFERENCES.....	250
-----------------	-----



LIST OF TABLES

TABLE	DESCRIPTION	PAGE
1	Program input format for density matrix elements.....	49
2	Relaxation data and results for $^{31}\text{P}$ in HMPD.....	214
3	Relaxation data and results for $^{14}\text{N}$ in HMPA.....	222
4	Relaxation Data and Results for $^2\text{H}$ Nucleus.....	231
5	Relaxation Data for $^{31}\text{P}$ in HMPA.....	238
6	Comparison of calculated and observed $^{31}\text{P}$ relaxation rates in HMPA.....	241
7	Translational diffusion coefficients of HMPA.....	242

## LIST OF FIGURES

FIGURE	DESCRIPTION	PAGE
1	Block diagram of the simulation program....	37
2	Pulse sequence for calibration of pulse width.....	68
3	Pulse sequence and input data for simulation of the CH DEPT experiment.....	108
4	Output of the DEPT simulation for CH system.....	110
5	Magnetization diagrams for CH DEPT experiment.....	112
6	Input data and output from the simulation of CH coupled DEPT experiment....	118
7	Simulation of $\theta$ -pulse angle dependence in CH DEPT experiment.....	119
8	Density matrix and output from the simulation of CH <sub>2</sub> DEPT experiment.....	121
9	Density matrix and output from the simulation of CH <sub>3</sub> DEPT experiment.....	122
10	Magnetization diagrams for CH <sub>2</sub> DEPT experiment.....	123
11	Magnetization diagrams for CH <sub>3</sub> DEPT experiment.....	124

FIGURE	DESCRIPTION	PAGE
12	Output from the simulation of CH <sub>2</sub> coupled DEPT experiment.....	126
13	Simulation of $\theta$ -pulse angle dependence in CH <sub>2</sub> DEPT experiment.....	127
14	Output from the simulation of CH <sub>3</sub> coupled DEPT experiment.....	129
15	Simulation of $\theta$ -pulse angle dependence in CH <sub>3</sub> DEPT experiment.....	130
16	The selective 2D heteronuclear chemical shift correlation pulse sequence.....	132
17	Input data and output from the simulation of CH selective shift correlation experiment.....	134
18	Input data and output from the simulation of CH <sub>2</sub> selective shift correlation experiment.....	135
19	Input data and output from the simulation of CH <sub>3</sub> selective shift correlation experiment.....	136
20	Input data and output from the 4-phasecycle CH selective shift correlation experiment.....	139

FIGURE	DESCRIPTION	PAGE
21	Pulse sequence and input data for simulation of the INADEQUATE experiment on $^{13}\text{C}$ - $^{13}\text{C}$ fragment.....	141
22	Output data from simulation of INADEQUATE experiment on $^{13}\text{C}$ - $^{13}\text{C}$ fragment.....	143
23	Output data from simulation of INADEQUATE experiment on $^{13}\text{C}$ - $^{12}\text{C}$ fragment..	146
24	Output data from simulation of INADEQUATE experiment on $^{13}\text{C}$ - $^{13}\text{C}$ - $^{13}\text{C}$ fragment.....	148
25	2D gated decoupler $^{13}\text{C}$ J- $\delta$ resolved pulse sequences.....	152
26	Input data and output from simulation of gated decoupler pulse sequences A and B on CH system.....	154
27	Output data from simulation of gated decoupler pulse sequence A on $\text{CH}_2$ system...	155
28	Output data from simulation of gated decoupler pulse sequence B on $\text{CH}_2$ system...	156
29	Output data from simulation of gated decoupler pulse sequences A and B on $\text{CH}_3$ system.....	157

FIGURE	DESCRIPTION	PAGE
30	2D J- $\delta$ resolved spectrum of 2-butanol obtained with pulse sequence C (with decoupled acquisition).....	163
31	Input data and output from simulation of gated decoupler pulse sequence C (with decoupled acquisition) on CH system.....	164
32	Output data from simulation of gated decoupler pulse sequence C (with decoupled acquisition) on CH <sub>2</sub> system.....	165
33	Output data from simulation of gated decoupler pulse sequence C (with decoupled acquisition) on CH <sub>3</sub> system.....	166
34	2D J- $\delta$ resolved spectrum of 2-butanol obtained with pulse sequence C (with coupled acquisition).....	170
35	Output data from simulation of gated decoupler pulse sequence C (with coupled acquisition) on CH system.....	171
36	Output data from simulation of gated decoupler pulse sequence C (with coupled acquisition) on CH <sub>2</sub> system.....	173
37	Output data from simulation of gated decoupler pulse sequence C (with coupled acquisition) on CH <sub>3</sub> system.....	174

FIGURE	DESCRIPTION	PAGE
38	Observed relaxation rates of $^{31}\text{P}$ in HMPD...	215
39	Observed $^{31}\text{P}$ spectrum of solid HMPD.....	219
40	Observed relaxation rates of $^{14}\text{N}$ in HMPA...	223
41	Variation of $\tau_{\theta}$ with $\tau_{\text{J}}$ for HMPD.....	227
42	Observed relaxation rates of $^2\text{H}$ in HMPD....	232
43	Comparison of calculated and observed $^{31}\text{P}$ relaxation rates in HMPA.....	237

"The outcome of any serious research can only be to  
make two questions grow where only one grew before."

Thorstein Veblen, 1919

PART 1

DENSITY MATRIX SIMULATION OF TWO-DIMENSIONAL AND  
MULTIPLE-PULSE NMR EXPERIMENTS



## CHAPTER I

### APPLICATION OF DENSITY MATRIX THEORY IN PULSED FT NMR

#### I.1 Introduction

This chapter discusses the application of the density matrix method in analyzing pulsed FT NMR experiments. A brief review of the basic aspects of density matrix theory is given, starting with the definition of the density matrix, prescriptions for the derivation of physical observables from the density matrix, the equation of motion of the density matrix and its solution, followed by a discussion of the incorporation of relaxation and chemical exchange phenomena into the equation of motion. The differences between the density matrix method and the classical approach, Bloch equations, are pointed out. Finally, the application of density matrix theory to pulsed FT NMR experiments is illustrated by following the evolution of the density matrix through a typical pulsed FT NMR experiment.

## I.2 Definition of Density Matrix and Equations for Physical Observables

The time-dependent Schroedinger equation for a system described by a wavefunction  $\Psi$  is given by

$$\hat{H}\Psi = i\hbar \frac{\partial \Psi}{\partial t}, \quad [1-1]$$

where  $\hat{H}$  is the total Hamiltonian of the system (1). The wavefunction  $\Psi$  can be represented in a complete orthonormal basis set  $\{|m\rangle\}$  as

$$\Psi(t) = \sum_m C_m(t) |m\rangle, \quad [1-2]$$

where  $C_m(t)$  are time-dependent coefficients.

The value of any observable property  $O$ , associated with the corresponding quantum mechanical operator  $\hat{O}$ , is given by (1,2)

$$O(t) = \langle \Psi(t) | \hat{O} | \Psi(t) \rangle \quad [1-3]$$

$$= \sum_{m,n} C_m^*(t) C_n(t) \langle m | \hat{O} | n \rangle.$$

Since  $O(t)$  is given in terms of products of coefficients, it is convenient to define a matrix  $P$  whose elements are the products of coefficients arranged so as to give

$$P_{ij} = C_i(t) C_j^*(t) \quad [1-4]$$

Equation [1-3] can then be written as

$$\begin{aligned}
 Q(t) &= \sum_{m,n} P_{nm}(t) \langle m | \hat{Q} | n \rangle \quad [1-5] \\
 &= \sum_{m,n} P_{nm}(t) Q_{mn} = \sum_n (\hat{P}(t) \hat{Q})_{nn} = \text{Trace}(\hat{P}(t) \hat{Q}).
 \end{aligned}$$

Equation [1-5] describes the property  $Q(t)$  for a particular molecule, but experimental measurements give the average  $\langle Q(t) \rangle$  per molecule in the ensemble.

Averaging over the ensemble, we obtain

$$\langle Q(t) \rangle = \text{Trace} (\hat{\rho}(t) \hat{Q}) \quad [1-6]$$

where the density matrix  $\hat{\rho}(t)$  is the ensemble average of  $\hat{P}(t)$  and has elements

$$\rho_{ij}(t) = \overline{C_i(t) C_j^*(t)}$$

where the bar denotes an ensemble average (1,2). Equation [1-6] gives the prescription for deriving average values of properties from the density matrix  $\hat{\rho}(t)$ .

The density matrix  $\rho$  is the quantum mechanical analog of the classical ensemble density.  $\rho$  contains all of the time dependence of the system and defines the system completely. The density matrix  $\rho$  is the representation of the density operator  $\hat{\rho}$  in a particular basis set, with elements

$$\rho_{ij} = \langle i | \hat{\rho} | j \rangle$$

Since the representation of any operator depends on the particular basis set used, the density matrix has different forms when represented in different basis sets. Although the form of the matrices,  $\rho$  and  $Q$  depend on the particular basis set chosen, the trace of their product, i.e. the average value of the observable, is independent of the basis set. Hence the density operator can be represented in any convenient basis set.

### I.3 Equation of Motion of the Density Matrix

The time-dependence of the density matrix can be ascertained from the time-dependent Schroedinger equation. The time derivative of the density matrix element  $\rho_{nm}$  is given by

$$\frac{d\rho_{nm}}{dt} = C_n(t) \frac{dC_m^*(t)}{dt} + \frac{dC_n(t)}{dt} C_m^*(t) \quad [1-7]$$

From Equations [1-1] and [1-2], one obtains

$$\sum_m C_m \hat{H} |m\rangle = i\hbar \sum_m \frac{dC_m}{dt} |m\rangle, \quad [1-8]$$

from which the time derivatives of the coefficients  $C_n(t)$  can be obtained as

$$i\hbar \frac{dC_n}{dt} = \sum_{m'} C_{m'} \langle n | \hat{H} | m' \rangle$$

and

[1-9]

$$-i\hbar \frac{dC_n^*}{dt} = \sum_{m'} C_{m'}^* \langle m' | \hat{H} | n \rangle$$

Substitution of Equation [1-9] into [1-7] gives

$$\frac{d\rho_{nm}}{dt} = \frac{1}{i\hbar} \sum_{m'} C_{m'} C_m^* \langle n | \hat{H} | m' \rangle - \frac{1}{i\hbar} \sum_{m'} C_n C_{m'}^* \langle m' | \hat{H} | m \rangle,$$

which can be rearranged to give

$$\frac{d\rho_{nm}}{dt} = \frac{i}{\hbar} \{[\rho, H]\}_{nm},$$

or, in operator form, as (1)

$$\frac{d\hat{\rho}}{dt} = \frac{i}{\hbar} [\hat{\rho}, \hat{H}] . \quad [1-10]$$

In the absence of any explicit time dependence in  $\hat{H}$ , the solution to Equation [1-10] is given by

$$\hat{\rho}(t) = \exp\{-i\hat{H}t/\hbar\} \hat{\rho}(0) \exp\{i\hat{H}t/\hbar\} , \quad [1-11]$$

where  $\hat{\rho}(0)$  is the density operator at time  $t = 0$ .

Provided the Hamiltonian  $\hat{H}$  is time-independent, the density matrix at any further instant in time can be computed from the matrix representation of Equation [1-11].

#### I.4 Rotating Frame Transformation

When the Hamiltonian contains a periodically time-dependent term, the equation of motion for  $\hat{\rho}$  is solved by transforming the density operator into a suitable rotating frame so that the effective Hamiltonian in the rotating frame is time-independent. When the Hamiltonian  $\hat{H}(t)$  is expressed as

$$\hat{H}(t) = \hat{H}_0 + \hat{H}_1(t) ,$$

the equation of motion for the density operator is given by

$$\frac{d\hat{\rho}}{dt} = \frac{i}{\hbar} [\hat{\rho}, \hat{H}_0 + \hat{H}_1(t)] . \quad [1-12]$$

In a frame rotating at frequency  $\omega$  about the laboratory z-axis, the density operator  $\hat{\rho}^*(t)$  is related to the laboratory frame density operator by

$$\hat{\rho}^*(t) = \exp(-i\omega\hat{I}_z t) \hat{\rho}(t) \exp(i\omega\hat{I}_z t) , \quad [1-13]$$

where  $\hat{I}_z$  is the z-component of the total spin angular momentum of the system. The equation of motion for  $\hat{\rho}^*$  is obtained from Equation [1-12] by recognizing that

$$\frac{d\hat{\rho}^*}{dt} = i[\hat{\rho}^*, \omega\hat{I}_z] + \exp(-i\omega\hat{I}_z t) \frac{d\hat{\rho}}{dt} \exp(i\omega\hat{I}_z t) . \quad [1-14]$$

One obtains

$$\frac{d\hat{\rho}^*}{dt} = \frac{i}{\hbar} [\hat{\rho}^*, \hat{H}_0 + \hbar\omega\hat{I}_z + \hat{H}_1^*(t)] \quad [1-15]$$

where

$$\hat{H}_1^*(t) = \exp(-i\omega\hat{I}_z t) \hat{H}_1(t) \exp(i\omega\hat{I}_z t) \quad [1-16]$$

is the time-dependent interaction in the rotating frame. In all cases of interest in magnetic resonance,  $\hat{H}_1^*(t)$  has a time-independent part which causes important changes in  $\hat{\rho}^*$ , and a time-dependent part which is far off-resonance and has no influence on the magnetizations of the system. One therefore takes the equation of motion for  $\hat{\rho}^*$  to be

$$\frac{d\hat{\rho}^*}{dt} = \frac{i}{\hbar} [\hat{\rho}^*, \hat{H}_{\text{eff}}] \quad [1-17]$$

where  $\hat{H}_{\text{eff}} = \hat{H}_0 + \hbar\omega\hat{I}_z + \text{time-independent part of } \hat{H}_1^*$ .

Since  $\hat{H}_{\text{eff}}$  is time-independent, the solution to Equation [1-17] is given by

$$\hat{\rho}^*(t) = \exp(-i\hat{H}_{\text{eff}}t/\hbar) \hat{\rho}^*(0) \exp(i\hat{H}_{\text{eff}}t/\hbar) \quad [1-18]$$

and the density operator in the laboratory frame will be

$$\hat{\rho}(t) = \exp(i\omega\hat{I}_zt) \hat{\rho}^*(t) \exp(-i\omega\hat{I}_zt) \quad [1-19]$$

It is instructive to illustrate some of the features of the rotating frame transformation by considering some simple nuclear magnetic resonance experiments on a single



spin 1/2 particle. The following examples also serve to illustrate the similarities between this quantum mechanical rotating frame and the rotating frames introduced in the solution of the Bloch equations. First, the case of a time-independent Hamiltonian is considered. The spin 1/2 particle is subjected to a constant magnetic field of strength  $H_0$ , along the z-axis. The Hamiltonian for this system can be written as

$$\begin{aligned}\hat{H}_0 &= -\gamma\hbar H_0 \hat{I}_z \\ &= -\hbar\omega_0 \hat{I}_z\end{aligned}\quad [1-20]$$

where  $\omega_0$  is the Larmor frequency (in radians  $\text{sec}^{-1}$ ),  $\gamma$  is the magnetogyric ratio of the nucleus, and  $\hat{I}_z$  is the z-component of the nuclear spin angular momentum operator. The Hamiltonian operator of the system in the frame rotating at angular frequency  $\omega$ , is given by

$$\begin{aligned}\hat{H}_{\text{eff}} &= \hat{H}_0 + \hbar\omega \hat{I}_z \\ &= -\hbar(\omega_0 - \omega) \hat{I}_z.\end{aligned}\quad [1-21]$$

When the system is exactly "on resonance",  $\omega_0 = \omega$  and  $\hat{H}_{\text{eff}} = 0$ . This leads to the result (Equation [1-17])

$$\frac{d\rho^*}{dt} = 0, \quad [1-22]$$

which implies that  $\rho^*$  is time-independent (in the rotating frame). The Bloch equations give exactly the same result in terms of magnetization vectors in the classical rotating frame (3,4).

The case where the Hamiltonian has a periodic time-dependence will now be considered. The system is subjected to an additional oscillating radio frequency field in a direction perpendicular to the constant field  $H_0$ . The Hamiltonian is given by

$$\hat{H} = -\hbar\omega_0 \hat{I}_z - \gamma\hbar H_1 \cos \omega t \hat{I}_x, \quad [1-23]$$

where  $H_1$  is the amplitude of the time-dependent magnetic field oscillating at a frequency  $\omega$ . Transformation into the rotating frame yields (Equation [1-16])

$$\hat{H}_1^* = -\frac{\gamma\hbar H_1 \hat{I}_x}{2} - \frac{\gamma\hbar H_1}{2} (\hat{I}_x \cos 2\omega t - \hat{I}_y \sin 2\omega t). \quad [1-24]$$

The first term in Equation [1-24] is time-independent and is the "on resonance" component of the rf field. The last term represents a field oscillating at frequency  $2\omega$  in the opposite direction. This counter-rotating component is

far from resonance and has virtually no effect on the magnetizations. The last term can therefore be neglected. The effective Hamiltonian in the rotating frame is then written as

$$\hat{H}_{\text{eff}} = -\hbar(\omega_0 - \omega)\hat{I}_z - \frac{\gamma\hbar H_1}{2}\hat{I}_x, \quad [1-25]$$

where  $\hat{H}_{\text{eff}}$  is time-independent. For the exact "on-resonance" condition, it reduces to

$$\hat{H}_{\text{eff}} = \frac{-\gamma\hbar H_1}{2}\hat{I}_x. \quad [1-26]$$

Equation [1-26] shows that, at resonance, the effective field in the rotating frame is just the  $H_1$  field along the x-axis. Bloch equations also give the same result.

### 1.5 Inclusion of Relaxation Effects and Chemical Exchange

The effect of spin relaxation caused by a stationary random perturbation  $\hat{H}_1(t)$ , has been incorporated into the equation of motion of the density matrix by Redfield (5). Using perturbation theory and making use of the ensemble average properties of  $H_1(t)$ , he has shown that the equation of motion of the density matrix due to relaxation is given by

$$\left(\frac{d\rho_{\alpha\alpha'}}{dt}\right)_{\text{relaxation}} = \sum_{\beta, \beta'} R_{\alpha\alpha'; \beta\beta'} (\rho_{\beta\beta'} - \rho_{\beta\beta'}^0) \quad [1-27]$$

where  $R_{\alpha\alpha'; \beta\beta'}$  is the relaxation matrix element given by

$$R_{\alpha\alpha'; \beta\beta'} = \frac{1}{2\hbar^2} [J_{\alpha\beta\alpha'\beta'}(\alpha' - \beta') + J_{\alpha\beta\alpha'\beta'}(\alpha - \beta) - \delta_{\alpha'\beta'} \sum_{\gamma} J_{\gamma\beta\gamma\alpha}(\gamma - \beta) - \delta_{\alpha\beta} \sum_{\gamma} J_{\gamma\alpha'\gamma\beta'}(\gamma - \beta')] \quad [1-28]$$

where  $\alpha - \beta$  is the frequency corresponding to the transition states  $\alpha$  and  $\beta$ , and  $J_{\alpha\alpha'\beta\beta'}(\omega)$  are the spectral densities (1),

$$J_{\alpha\alpha'\beta\beta'}(\omega) = \overline{\int_{-\infty}^{\infty} \langle \alpha | \hat{H}_1(t) | \alpha' \rangle \langle \beta' | \hat{H}_1(t+\tau) | \beta \rangle e^{-i\omega\tau} d\tau} \quad [1-29]$$

where the bar indicates an ensemble average.

The equation of motion of the density operator has been further modified to account for the chemical exchange processes (6). A chemical exchange process has the effect of permuting the nuclear spin states, and the average rate of change of the density operator can be given by

$$\left(\frac{d\hat{\rho}}{dt}\right)_{\text{exchange}} = \frac{1}{\tau} (\hat{P}\hat{\rho}\hat{P}^+ - \hat{\rho}) \quad [1-30]$$

where an exchange event occurs on the average every  $\tau$  seconds and  $\hat{P}$  is the permutation operator. This approach to chemical exchange is elegant for simple product basis sets, but tends to be complicated when product bases are unsuitable (strongly coupled systems).

#### I.6 Density Matrix Method and Bloch Equations Approach

The Bloch equations provide the classical description of the motion of non-interacting spins. These equations (1,3,4), are the equations of motion for the magnetization components  $M_x$ ,  $M_y$  and  $M_z$ , in the presence of relaxation effects:

$$\frac{dM_z}{dt} = \gamma(\vec{M} \times \vec{H})_z + \frac{M_0 - M_z}{T_1}$$

$$\frac{dM_x}{dt} = \gamma(\vec{M} \times \vec{H})_x - \frac{M_x}{T_2}$$

[1-31]

$$\frac{dM_y}{dt} = \gamma(\vec{M} \times \vec{H})_y - \frac{M_y}{T_2}$$

where  $M_0$  is the thermal equilibrium magnetization and  $T_1$  and  $T_2$  are the longitudinal and transverse relaxation times respectively.

The Bloch equations can be derived from density matrix theory in some situations by evaluating the expressions for the expectation values of the magnetization components. Both methods, the density matrix theory and Bloch equations approach, yield identical results, in the description of many experiments, for the observable components of magnetization in weakly coupled spin systems. However, the applicability of the Bloch equations is limited. Some of the major differences between these methods are amplified in the following:

(i) Exact expressions for the relaxation terms can be derived using the density matrix method, as was done in the Redfield relaxation equations. In contrast, the relaxation terms included in the Bloch equations are purely empirical. The inclusion of these terms is justifiable only because they seem to explain experimental observations. Density matrix theory provides, in addition, the conditions under which the Bloch equations are applicable.

(ii) The classical description of NMR experiments, given by the Bloch equations, are not applicable for strongly coupled spins. Here it is necessary to introduce quantum mechanical energy levels and operators rather than classical magnetization vectors. For weakly coupled spin systems, the simple products of the eigenfunctions of the

separated spins are eigenfunctions of the time-independent Hamiltonian  $H_0$  for the complete spin system, and hence the transitions between various energy levels are identifiable as corresponding to the spin flips of individual nuclei.

In such cases it is possible to write down Bloch equations for the magnetization components of each individual

nucleus. However, in strongly coupled spin systems, the simple product functions are not eigenfunctions of the Hamiltonian  $H_0$  and the transitions cannot be identified as arising from the spin flip of any particular nuclei.

Density matrix theory must be used to describe the time dependence of such strongly coupled spin systems.

(iii) The Bloch equations are concerned only with magnetization components (one-quantum coherences), not with zero quantum and multiple quantum coherences, and hence fail to describe the creation and evolution of these invisible (directly unobservable) coherences in multiple-pulse experiments. These coherences can be produced in a spin system initially at thermal equilibrium by application of two radiofrequency pulses separated by a delay (7). Multiple quantum coherence phenomena have been utilized in multiple pulse and two dimensional FT experiments to provide additional information about the spin system. In such situations, the density matrix theory must be used in order to describe the signals and the quantum mechanical state of the system.

## I.7 Applications to Pulsed FT NMR

The density matrix theory can be used to describe pulsed FT and CW NMR experiments. Since the theory is capable of explaining the origin and behaviour of multiple quantum coherences, it is especially useful in the analysis of many multiple pulse FT experiments. However, the explicit computation of the density matrix can become tedious depending on the size of the spin system and the pulse sequence employed.

A typical pulsed FT NMR experiment consists of the application of a set of pulses to the spin system, separated by periods of free precession followed by an acquisition period where the transverse components of the magnetizations are sampled. The pulses may act on all nuclei (homonuclear systems) or may be selective and act only on one group of nuclei (heteronuclear systems). The flip angles and phases of the pulses, duration of the free precession periods, spin decoupling during precession and/or acquisition periods, etc., can be used to select the information about the spin system which is obtained in the measured response. The transverse components of the magnetization are measured as a time varying signal referred to as the free induction decay (FID). In order



to improve the signal-to-noise ratio, the signals from a number of scans are co-added to obtain the final FID. During the individual scans, the phases of the pulses may be varied to suppress undesirable or spurious signals or to correct for pulse-length imperfections, pulse-phase abnormalities, and for differentiating magnetization arising from various orders of coherence, i.e. zero quantum, single quantum, and multiple quantum coherences. The final FID is Fourier transformed to obtain the conventional frequency domain NMR spectrum.

Recently, two dimensional FT experiments have been developed (8). Here the signal is collected as a function of two time variables. It is then Fourier transformed in both time domains to yield a frequency spectrum which is a function of two independent frequency variables (9-12). The advantage of two dimensional experiments over the conventional FT experiments is the simplification of complex spectra which can be achieved by selectively presenting a particular type of spectral information (e.g. chemical shift) along one frequency dimension while simultaneously displaying another spectral parameter (e.g. spin-spin coupling) along the second dimension (13-15). Thus the total information content of the conventional spectrum is partitioned along two dimensions, which greatly simplifies the interpretation of spectra,

particularly those of large molecules. Another application of two dimensional experiments is in correlating the chemical shifts of coupled nuclei in homonuclear and heteronuclear systems (16). The correlation of chemical shifts is effected through some mechanism for magnetization transfer between the nuclei involved (17). The different coupling mechanisms utilized for magnetization transfer are scalar J coupling interaction (18-22), dipole-dipole interactions (23-25), and chemical exchange processes (26,27). Depending on the shift correlation information desired, a two dimensional experiment can be performed utilizing any of the above mechanisms for magnetization transfer. Pulse sequences can also be designed to utilize the multiple quantum coherences in spectrum editing (7,28-30). It is possible, for example, to edit the spectrum so as to differentiate signal components arising from various spin subsystems. This technique has been used to distinguish between signals arising from CH, CH<sub>2</sub>, and CH<sub>3</sub> spin systems (31).

Pulse sequences for all types of NMR experiments can be represented as a series of radiofrequency pulses and free precession periods applied to a spin system which is initially at thermal equilibrium. In applying the density matrix theory to the description of these experiments, one begins with the thermal equilibrium density matrix. It is

convenient to choose a basis whose members are the eigenfunctions of  $H_0$ , the Hamiltonian operator in the absence of radiofrequency pulses. The Hamiltonian operator corresponding to a multiple pulse experiment would be different at each stage in the pulse sequence. Hence it is preferable to think of the entire pulse sequence as a sequence of steps, such that during any particular step, the Hamiltonian operator has a definite time dependence. The state of the spin system during the experiment can then be followed by monitoring the evolution of the density matrix in each successive step. In a multiple-pulse sequence, there are basically two types of Hamiltonian operators acting on the spin system in a sequential manner: radiofrequency pulses and free precession periods. Solving the equation of motion of the density matrix during the free precession is straightforward since the Hamiltonian is time-independent (Equation [1-11]). The time dependence of the Hamiltonian during the application of an rf pulse can be removed by transforming the system into a rotating frame with an angular frequency equal to the frequency of the rf pulse irradiation and the solution of the equation of motion for the density matrix (Equation [1-17]) is again straightforward (Equation [1-19]):

The time evolution of the density matrix in a multiple pulse sequence can be represented as follows:

Let  $\hat{\rho}(0)$  be the thermal equilibrium density matrix

operator and let  $H_1, H_2, \dots, H_n$  be the sequence of Hamiltonian operators representing the pulse sequence.

The operators are time-ordered with the earliest one

leftmost and successive ones to the right. Here it is

assumed that the time-dependence of the operators has been removed by appropriate rotating frame transformation. The

final density operator at the end of the pulse sequence is given by

$$\hat{\rho} = \hat{T}_n (\dots (\hat{T}_2 (\hat{T}_1 \hat{\rho}(0) \hat{T}_1^+) \hat{T}_2^+ \dots) \hat{T}_n^+ \dots) \quad [1-32]$$

where  $\hat{T}_i$  is the propagator during the  $i$ th time interval.

Using this prescription it is then possible to follow the

evolution of the density operator under any given pulse

sequence. However, at the computation stage, it is

preferable to work with the matrix representations of the

operators rather than the operators themselves since it is

easier to apply the matrix transformations rather than

evaluate operator transformation equations.

### I.8 Analysis of a Simple FT Experiment

The application of density matrix theory in the description of pulsed FT experiments is nicely illustrated by considering the pulse sequence used for routine measurement of spectra. The sequence consists of a  $90^\circ$  pulse followed by signal acquisition. The detailed evolution of  $\rho$  during this sequence will be considered for an ensemble of systems containing a single spin  $1/2$  nucleus.

The system is subjected to a static magnetic field of strength  $H_0$ , along the  $z$  axis. The Hamiltonian for the system is given by Equation [1-20] with eigenfunctions  $|\alpha\rangle$  and  $|\beta\rangle$ , corresponding to eigenvalues  $-\hbar\omega_0/2$  and  $+\hbar\omega_0/2$  respectively. From statistical thermodynamics, the thermal equilibrium density operator  $\hat{\rho}(0)$  can be written as

$$\hat{\rho}(0) = (1/z) \exp(-\hat{H}_0/kT) , \quad [1-33]$$

where  $z$  is the partition function of the system. The density matrix will be diagonal at thermal equilibrium.

In the high temperature limit,

$$\exp(-\hat{H}_0/kT) \cong \hat{1} - \hat{H}_0/kT , \quad [1-34]$$

and the density matrix elements are

$$\rho(0)_{\alpha\alpha} = (1+\Delta)/2, \quad \rho(0)_{\beta\beta} = (1-\Delta)/2 \quad \text{and} \quad \rho(0)_{\alpha\beta} = \rho(0)_{\beta\alpha} = 0,$$

where  $\Delta = \gamma \hbar H_0 / 2kT$ .

The magnetization per molecule for the ensemble at thermal equilibrium can now be determined from Equation [1-6] and has components

$$\langle M_i \rangle = \text{Trace} (\rho \tilde{M}_i) ; \quad i = x, y, z, \quad [1-35]$$

where

$$\tilde{M}_i = \gamma \hbar I_i,$$

and  $I_i$ ,  $i = x, y, z$  are given by the Pauli spin matrices. Evaluation of the magnetization components gives

$$\langle M_x \rangle = 0, \quad \langle M_y \rangle = 0, \quad \text{and} \quad \langle M_z \rangle = (1/2) \gamma \hbar \Delta. \quad [1-36]$$

As expected, the x and y components of the magnetization vanish since the off-diagonal elements of the density matrix are all zero. Note that  $\langle M_x \rangle$  is proportional to

$(\rho_{\alpha\beta} + \rho_{\beta\alpha})$  and  $\langle M_y \rangle$  is proportional to  $(\rho_{\alpha\beta} - \rho_{\beta\alpha})$  so that transverse magnetizations are present only if  $\rho$  has non-zero off-diagonal elements. The value of  $\langle M_z \rangle$  is proportional to  $(\rho_{\alpha\alpha} - \rho_{\beta\beta})$  and, in this case, is simply the thermal equilibrium magnetization.

In the presence of the rf pulse, the Hamiltonian for the system is given by Equation [1-23]. As discussed in Section I.4, the time dependence of the Hamiltonian  $\hat{H}$  can be removed by transforming the system into a frame rotating at frequency  $\omega$  about the field  $H_0$ , such that  $\gamma H_1 \gg (\omega - \omega_0)$ . The equation of motion of the density operator in the rotating frame, then becomes

$$\frac{d\hat{\rho}^*}{dt} = \frac{-i\gamma H_1}{2} [\hat{\rho}^*, \hat{I}_x], \quad [1-37]$$

with solution,

$$\hat{\rho}^*(\tau) = \exp\left(\frac{i\gamma H_1 \tau \hat{I}_x}{2}\right) \hat{\rho}^*(0) \exp\left(-\frac{i\gamma H_1 \tau \hat{I}_x}{2}\right). \quad [1-38]$$

$(1/2)\gamma_1 H_1 \tau$  is the angle through which the magnetization is tipped by the pulse and will be denoted by  $\theta$  (in radians). The representation of the exponential operator can be obtained from its series expansion, from which we have

$$\exp(i\theta \tilde{I}_x) = \begin{bmatrix} \cos \frac{\theta}{2} & -i \sin \frac{\theta}{2} \\ i \sin \frac{\theta}{2} & \cos \frac{\theta}{2} \end{bmatrix}. \quad [1-39]$$

For an rf pulse of flip angle  $90^\circ$ ,  $\theta = \pi/2$ , and the representation matrix in Equation [1-39] reduces to

$$\exp(i\frac{\pi}{2} \tilde{I}_x) = \frac{1}{\sqrt{2}} \begin{bmatrix} 1 & i \\ i & 1 \end{bmatrix}. \quad [1-40]$$

For simplicity the density matrix is viewed in the rotating frame in the following discussion. After the transformation indicated in Equation [1-38], the density matrix in the rotating frame is given by

$$\tilde{\rho}^*(\tau) = \frac{1}{2} \begin{bmatrix} 1 & 0 \\ 0 & 1 \end{bmatrix} + \frac{1}{2} \begin{bmatrix} 0 & -i\Delta \\ i\Delta & 0 \end{bmatrix}. \quad [1-41]$$

Evaluating the components of the magnetization per molecule in the rotating frame, we obtain



$$\langle M_x(\tau) \rangle = 0, \quad \langle M_y(\tau) \rangle = \frac{\Delta}{2}, \quad \text{and} \quad \langle M_z(\tau) \rangle = 0. \quad [1-42]$$

The 90° pulse along the x-axis of the rotating frame has rotated the magnetization from the z-axis to the y-axis of the rotating frame in keeping with simple magnetization vector diagrams.

The spin system is now allowed to precess freely. The effective Hamiltonian is given by Equation [1-21]. The representation of  $\exp(iH_{\text{eff}} t_1)$  is diagonal in the simple product basis, given by

$$\exp(iH_{\text{eff}} t_1) = \begin{bmatrix} \exp\{i(\omega - \omega_0)t_1/2\} & 0 \\ 0 & \exp\{-i(\omega - \omega_0)t_1/2\} \end{bmatrix}, \quad [1-43]$$

where  $t_1$  is the acquisition time variable. The density matrix during the free precession, therefore becomes

$$\rho^*(\tau + t_1) = \frac{1}{2} \begin{bmatrix} 1 & 0 \\ 0 & 1 \end{bmatrix} + \frac{1}{2} \begin{bmatrix} 0 & -i\Delta \exp\{i(\omega - \omega_0)t_1\} \\ i\Delta \exp\{-i(\omega - \omega_0)t_1\} & 0 \end{bmatrix}. \quad [1-44]$$

During the free precession period, the non-zero off-diagonal elements develop time dependence.

The NMR signals in the rotating frame, can now be computed using the expressions for expectation values of magnetization components to give

$$\begin{aligned} \langle M_x(t_1+\tau) \rangle &= -(\Delta/2) \sin\{(\omega-\omega_0)t_1\} \\ \langle M_y(t_1+\tau) \rangle &= -(\Delta/2) \cos\{(\omega-\omega_0)t_1\} \\ \langle M_z(t_1+\tau) \rangle &= 0. \end{aligned} \quad [1-45]$$

These calculations suggest that the magnetization lies in the transverse plane (xy plane) throughout the detection period  $t_1$ . If the relaxation effects were included, we would have obtained

$$\begin{aligned} \langle M_x(t_1+\tau) \rangle &= -(\Delta/2) \sin\{(\omega-\omega_0)t_1\} \exp\{-t_1/T_2\} \\ \langle M_y(t_1+\tau) \rangle &= -(\Delta/2) \cos\{(\omega-\omega_0)t_1\} \exp\{-t_1/T_2\} \end{aligned} \quad [1-46]$$

Spin-spin relaxation damps the oscillatory functions, with the characteristic rate constant  $(1/T_2)$ . Equation [1-46] gives the time domain magnetization functions for this simple experiment. The conventional mode of presentation of the NMR spectrum is in the frequency domain. The frequency domain spectrum can be obtained by Fourier cosine transformation of  $\langle M_x(\tau+t_1) \rangle$  or  $\langle M_y(\tau+t_1) \rangle$  time

domain functions. Fourier transformation of the time domain functions in Equation [1-46] gives a Lorentzian line centered at frequency  $\nu - \nu_0$  (in Hz), with full width at half-height of  $1/(\pi T_2)$  (in Hz). It should be noted that  $\omega = 2\pi \nu$  in Equations [1-45] and [1-46].

The example of the spin 1/2 system illustrates the way in which the density matrix theory is used to describe pulsed FT experiments. An analysis using the classical Bloch equations would have yielded identical results in this case. For larger systems with strong coupling or for sequences which involve the generation of multiple quantum coherences, the Bloch equation approach is inadequate. Even with larger spin systems, the basic guidelines in the application of density matrix theory remain the same, however the computational complexity can increase rapidly.

### I.9 Summary

In this chapter a brief description of density matrix theory and its applications in the description of pulsed FT NMR experiments was presented. The equation of motion of the density matrix was set up and the application of the rotating frame transformation in the simplification of the equation of motion described. Modifications of the density matrix theory to take into account the relaxation

and chemical exchange processes, were briefly discussed.

Finally, the application of the density matrix theory in

the description of pulsed FT experiments was illustrated

by considering a simple example of an ensemble of spin  $1/2$

systems subjected to the most basic FT experiment, the

$90^\circ$  pulse-acquire sequence. The next chapter describes

the implementation of a computer program to carry out

density matrix computations on more general spin systems

under a variety of multiple pulse and two dimensional FT

experiments.

## CHAPTER II

### DESCRIPTION OF THE SIMULATION PROGRAM

#### II.1 Introduction

The implementation of a simulation program to analyze multiple pulse and two dimensional FT NMR experiments, based on density matrix theory, is discussed in this chapter. The objectives of the program are laid out, the structure of the program is illustrated with a block diagram and brief descriptions of the major subprograms are given. The data structure for the representation of the density matrix is described. The computation of the thermal equilibrium density matrix is illustrated with examples of the IS and IS<sub>2</sub> spin systems. The implementation of the density matrix transformation by a rf pulse and during free precession periods is discussed, with the transformations illustrated for the IS and IS<sub>2</sub> systems.

The effects of broadband decoupling are considered briefly. The equation of motion for the density matrix in the presence of a broadband decoupler irradiation, and its

solution are given. The simulation of the signal acquisition process is considered next. The algorithms used to compute and simplify the signal expressions are briefly described. The interpretation of the frequency terms in the computed signal is clarified by carrying out the analysis of a simple pulse sequence.

The implementation of various other features in the program, such as phase cycling of the rf pulses and the receiver, rf pulses of any given tip angle, are described. Finally, some of the limitations of the current version of the program are discussed along with suggestions for future extensions.

## II.2 Objectives of the Simulation Program

The program has been intended to simulate the effects of multiple pulse sequences on a variety of spin systems. The development of the program has been motivated by the conspicuous absence of a device for analyzing the rapidly increasing number of two-dimensional NMR (2D NMR) and other multiple pulse experiments. The simulation method is based on the density matrix description of pulsed NMR discussed in the last chapter. Some work on the computer simulation of multiple pulse experiments has been reported using Bloch equations (32)

and density matrix theory (33-35). Recently another approach to simulation of multiple pulse and 2D NMR experiments has been devised, making use of the super-spin formalism (36-38). Simple rules for following the evolution of the density operator under rf pulses and during free precession periods have also been given (39-41), but the operator expressions tend to be prohibitively complex in a typical multiple pulse sequence. The computational complexity associated with the density matrix method grows rapidly with the size of the spin system. The need for automated density matrix calculation is therefore apparent, and the aim of this thesis has been to develop a rather general system to accommodate a large variety of pulse sequences and to simulate many of the features used in modern high resolution NMR spectroscopy.

The spin systems that can be analyzed by the program are homonuclear and heteronuclear  $I_m S_n$  systems of weakly coupled spin 1/2 nuclei with  $1 < m, n < 3$ . The input format is similar to the pulse microprograms used with high resolution NMR spectrometers. The specification of the pulse sequence constitutes: the definition of the spin system; specification of the pulse angles; pulse phases and nuclei on which the pulses act; delay periods and signal acquisition periods with or without broadband decoupling; options to carry out phase cycling of pulses and detectors; and so on.

Pulses can be applied to either I or S nuclei (as in a heteronuclear system), or to both nuclei (as in a homonuclear system), and along the +x, -x, +y, -y axes of the rotating frame. The program is also capable of simulating the effects of pulses of any given flip angle, besides the most common 90° and 180° pulses. Since our early experience showed that examination of the elements of density matrix at different stages in a pulse sequence enabled us to investigate the behaviour of magnetizations and multiple-quantum coherences, a facility to output the density matrix was incorporated into the simulation routine.

The computed signal can be simplified to some extent so as to make the output more comprehensible. Another important simplification feature has been incorporated to allow explicit substitution for the durations of precession periods in terms of  $1/(nJ)$ , where  $n$  is an integer and  $J$  is the scalar coupling constant between the I and S nuclei.

### II.3 Implementation of the Simulation Program

In order to have a program with reasonable speed, efficiency, and portability, the FORTRAN language was chosen rather than an algebraic language like REDUCE2 (42)



for the implementation of the simulation scheme. The program is organized in a modular fashion, with a short main program and a number of subprograms, each with a distinct function. This feature simplifies the task of expanding the program, since modules to perform new functions can be added on with only relatively minor changes to the short main program. The main program calls on different subprograms to handle various steps specified in the input pulse sequence. Subprograms pass control back as soon as their function is performed and the main program chooses another subprogram depending on the next input specification. Communications between the main program and subprograms are made mostly through common blocks of memory.

The density matrix elements are the most important and complicated items to be represented in the simulation program. The elements of the density matrix are, in general, complex and depend explicitly on the durations of precession and decoupling periods. In order to strike a balance between the complexities of pulse sequences which could be handled and the storage requirements, the number of time variables is limited to four:  $T_1$ ,  $T_2$ ,  $D_1$ , and  $D_2$ . Each of these variables can be used to define the duration of a period of free precession or a decoupling period, and each variable may be used no more than twice

within a given sequence. Each density matrix element, at any particular point in the pulse sequence, will consist of a sum of terms of the form:

$$\text{TERM} = (A + iB) \exp[2\pi i(\nu_1 T_1 + \nu_2 T_2 + \nu_3 D_1 + \nu_4 D_2)] \quad [2-1]$$

where  $A + iB$  is a complex number and  $\nu_1, \nu_2, \nu_3, \nu_4$  denote frequencies which describe the evolution during time periods  $T_1, T_2, D_1, D_2$  respectively. The frequencies  $\nu_1, \nu_2, \nu_3, \nu_4$  are equal to frequencies for transitions between particular spin states so that the specification of each frequency variable requires the specification of a pair of indices (encoded into a single integer) which identify the states involved in the corresponding transitions. Each term can therefore be represented as a complex number and four encoded integers which specify the frequency variables in each of the time domains. A collection of these terms, each with distinct exponential factors, completely defines a particular element of the density matrix. In order to economize on computer memory requirements, the density matrix is represented as a collection of elements, each consisting of a number of terms, in single dimension arrays with appropriate arrays of index variables to specify the density matrix element to which the particular terms belong. The numbers of

terms associated with each of the density matrix elements are also stored in a single dimension array. This data structure for the representation of the density matrix will be referred to as "data array". For convenience in accessing and manipulating the density matrix, the index of the starting row and the total number of the rows of the "data array" occupied by the density matrix, at a particular stage in the simulation are stored in another array referred to as the "status array". Since the density matrix is Hermitian, only the elements in the upper triangle are stored. The data structure representing the density matrix resides in a common block and is thereby accessible to the subprograms which manipulate and update its elements.

A block diagram of the program is given in Figure 1. The functions of the main program are to read and echo the input pulse sequence, and to control the flow of execution by selecting the appropriate subprogram to handle the particular step in the input. The main program also carries out the task of initializing the values of certain variables, constants and arrays. The subprogram SPNSYS computes the initial thermal equilibrium density matrix appropriate for the spin system specified in the input data, PULSES transforms the density matrix by application of the pulse specified in the input, and the

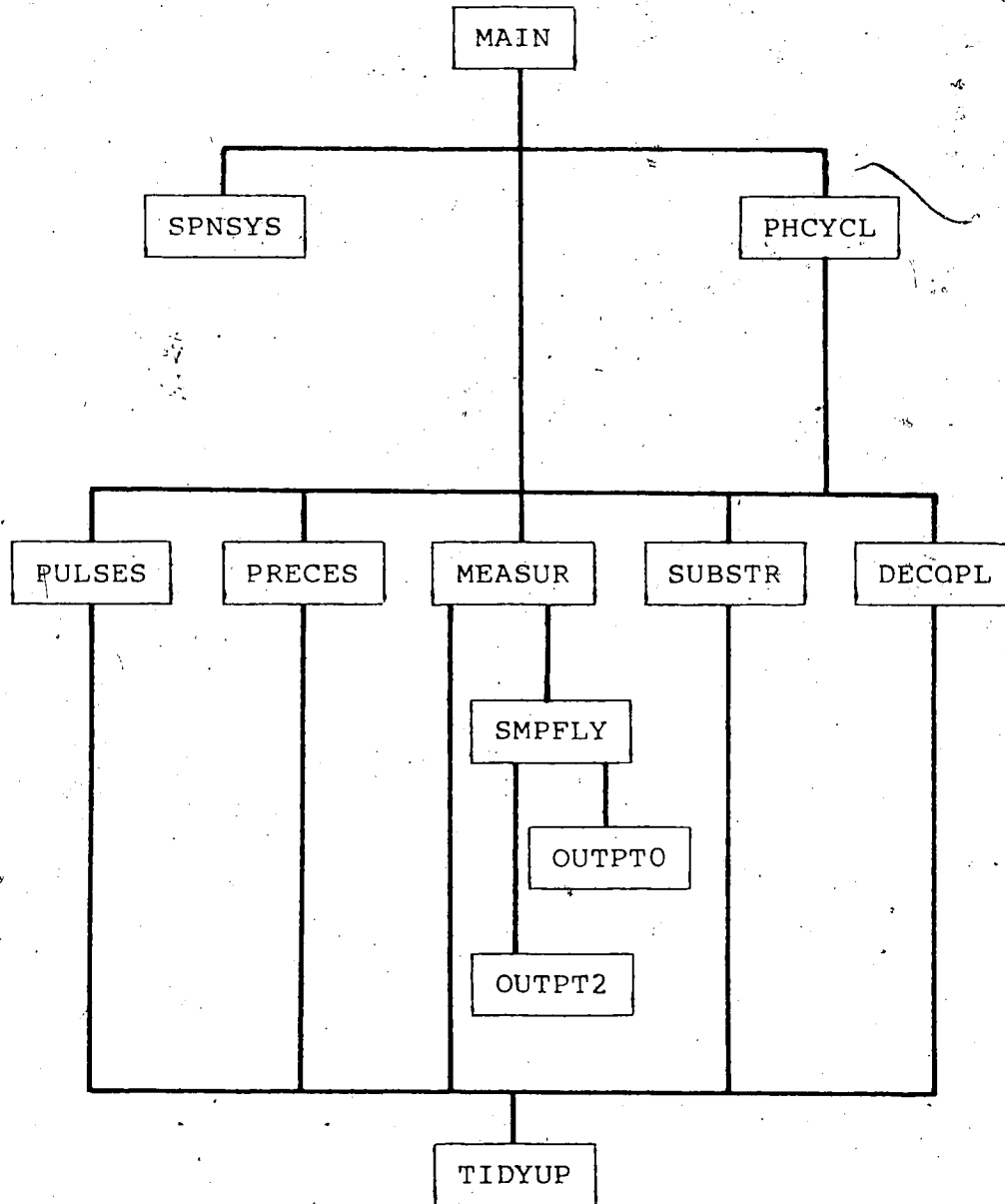


Figure 1. Block diagram of the simulation program.

transformation of the density matrix during the free precession periods is carried out by the subprogram PRECES. The magnetization components are computed by MEASUR and simplified to a certain extent by the subprogram SMPFLY, which recognizes the relationships between  $\exp(i\phi) \pm \exp(-i\phi)$  and  $\cos \phi$  and  $\sin \phi$ . The parities of the sine and cosine functions are also invoked in this simplification procedure. After simplification, the final output may have considerably many fewer terms than are present in the internal data structure. The printing of the signal expressions is carried out by the subprogram OUTPT2. The subprogram SUBSTR allows the simplification of the density matrix at intermediate stages by explicit substitution for the duration of one of the time periods T1, T2, D1, or D2 by  $1/(nJ)$ , where J is the I-S spin-spin coupling constant and n is an integer. Such substitution often causes certain terms of the density matrix elements to vanish and produces significant simplification. The transformation of the density matrix during broadband decoupling is carried out by DECOPL, which computes the density matrix during the decoupling period using an averaging process discussed in detail in Chapter III. The phase cycling of pulses and the receiver is handled by the subprogram PHYCYCL, which to a certain extent duplicates some of the functions of the main

program by controlling the flow of execution inside the phase cycling loop. As indicated by the block diagram, it interacts with most of the other subprograms. It also keeps track of the signals generated during each of the individual phase cycles and passes on the accumulated signal for simplification. Besides the major subprograms mentioned above, there are a number of other subprograms which carry out various other functions. One of the most important among these is TIDYUP, which organizes the rows of the "data array", and carries out some simplification by collapsing mutually cancellable terms, simplifying terms which can be summed together, and deleting blank rows formed during the simplification procedure.

a. Description of Input Commands

A description of the input commands to the simulation program is given below. Most of the commands consist of two strings (each containing four characters), typed consecutively (without blanks or any other characters between them) on the same line. There must be only one such command in a single line of the input file. Command names which fall short of four characters are to be typed in left justified fashion. The input is read from FORTRAN unit 5.

<u>Command</u>	<u>Description</u>
1. SPIN $I_m S_n$	Sets up the thermal equilibrium density matrix for the $I_m S_n$ spin system with $1 < m, n < 3$ .
2. HOMO	Defines the spin system to be homonuclear. HOMO command should be specified <u>before</u> the SPIN command.
3a. PULS $abcc$	Applies a pulse transformation to the density matrix. $a$ specifies the pulsed nucleus and can be I or S. $b$ specifies the pulse length and can be any of the following:
b. PULS $abccabc'c'...$	<p>A : denotes a <math>90^\circ</math> pulse</p> <p>B : denotes a <math>180^\circ</math> pulse</p> <p>C-F: can be used to assign any desired pulse length (see SET command below).</p> <p><math>cc</math> specifies the direction in the rotating frame along which the pulse is applied and can be any of: <math>+x</math>, <math>-x</math>, <math>-y</math>, and <math>-y</math>.</p> <p>The command (3b) shows how the</p>

PULS command is to be used in a phase cycle sequence. `c'c'` specifies the phase of the pulse in the second pass through the phase cycle (see PHASECYCLE command below).

4. PRECtt

Applies the free precession transformation to the density matrix during the time period `tt`, where `tt` can be any of T1, T2, D1 or D2. It is preferable to use T1 or T2 for signal acquisition periods since the program carries out more extensive simplification on terms containing T1 or T2. Each of the time periods can be used no more than twice in a pulse sequence.

5a. MEASaXYb

b. MEASac

c. MEASaXYbaXYb'...

d. MEASacac'...

Simulates the signal acquisition by measuring the magnetization components. Command (5a) measures the complex quadrature magnetization. `a` specifies the



nucleus. (I or S).  $b$  specifies the particular quadrature combination as given below:

$$b = 0 : X + iY$$

$$b = 1 : -Y + iX$$

$$b = 2 : -X - iY$$

$$b = 3 : Y - iX$$

The output is onto FORTRAN unit

6. Command (5b) measures a single magnetization

component.  $a$  denotes the

nucleus (I or S) and  $c$  denotes

the magnetization component (X,

Y or Z). 5c and 5b illustrate

how the commands 5a and 5d are

to be used inside a phase

cycling loop. Here  $b'$  and  $c'$

specifies the component to be

measured in the second pass

through the phase cycle (see

PHASECYCLE command below).

6. DCPLabbtt

Applies the transformation

appropriate for spin decoupling

during a precession period.  $a$

specifies the nucleus to be decoupled (I or S), **bbb** denotes 3 blanks, and **tt** specifies the time period during which decoupling is carried out (T1, T2, D1, or D2).

7. **SUBStt=1/(nnJ)**

Allows the substitution of the specified time variable by a term proportional to the reciprocal of the coupling constant J. **tt** specifies the time variable (T1, T2, D1, or D2) and **nn** is a two digit integer (in I2 format).

8. **PHASECYCLEnn**

Allows phase cycling to be carried out. This command is used to set up a loop, terminated by another such phase cycle command. The loop encloses that part of the pulse sequence in which phase cycling is carried out. **nn** specifies the number of cycles and is such that  $1 < nn < 64$  (in I2

format). The pulse phases and receiver phases to be used for the different cycles are to be specified sequentially in all PULS and MEAS commands. If the number of cycles in the loop is larger than 16, then specifications for 16 cycles should appear on each line, the next 16 on the next line leaving the first four characters blank, and so on. The last command inside the phase cycle loop must be a MEAS and there can only be one MEAS command in the loop. There can only be one phase cycle loop in the pulse sequence.

9a. SETP**bb**angle

Defines any desired pulse angle for the pulses C-F. P specifies one of the pulses (C, D, E, or F) and angle represents the flip angle (in degrees) to be assigned to P. The angle is to

## b. SETspecaa

be specified in F5.1 format.  
 bbb denotes 3 blank characters.

Allows the user to set states  
 (ON/OFF) of certain  
 specification switches. aa is  
 the switch setting and is either  
 ON or OFF. spec is one of the  
 following:

(a) MOVE: If it is desired to  
 store the density matrices  
 after each step, for print  
 out or debugging purposes,  
 the OFF setting can be used  
 to prevent overwriting of  
 previous density matrices  
 within the data table. The  
 default setting is ON.

(b) DEBUG: Intermediate output  
 for debugging purposes can  
 be produced with the ON  
 setting. The default  
 setting is OFF.

## 10. WRDM

Can be used to print out the  
 density matrix after the

- previous command in the pulse sequence. The output is onto FORTRAN unit 6.
11. DUMP Can be used to print out the internal representation (data structure) of the density matrix after the previous command in the pulse sequence. The output is onto the FORTRAN unit 6.
12. COMMstring Echo prints **string** as a comment onto FORTRAN unit 6.
13. STOP Stop calculation and terminate execution.
14. NEXT Terminates the calculation on the current pulse sequence and starts calculation on the pulse sequence specified, starting from the next line of input.
15. STDM Stores the internal representation of the density matrix onto FORTRAN unit 7. It can be read in later in another run to continue the calculation.

16. RDFL

Reads in an initial density matrix from FORTRAN unit 4. This feature can be used to carry out calculations starting with non equilibrium density matrices. The FORTRAN unit 4 should contain the SPIN command (HOMO and SET commands if applicable), the NEDM and CLFL commands as well as the density matrix elements.

NEDM (subcommand)

This subcommand follows the SPIN command mentioned above, and initiates reading in the density matrix. The density matrix element is represented as described in Section II.3. Only the non zero and upper triangular and diagonal elements should be specified. There should be one line for each "TERM" (Equation [2-1]) of every density matrix element. Density matrix elements are to be defined one after the other.

Each line should contain the data described in Table 1.

After all matrix elements have been specified, the input mode is terminated by inserting a zero in the field corresponding to NCOMP (Table 1).

CLFL (subcommand) Instructs the program to terminate input from FORTRAN unit 4 and to continue to read input from the normal input device (FORTRAN unit 5).

#### II.4 Choice of Basis Sets

The basis set for representation of  $\hat{\rho}$  is the eigenbasis of  $\hat{H}_0$  which, in the weak coupling limit, is taken to be the direct product of the irreducible basis of the  $I_m$  subgroup and the irreducible basis of the  $S_n$  subgroup. The construction of the irreducible basis in the simulation program uses a building up process which starts with the eigenfunctions of the single spin 1/2 system, forms uncoupled simple product basis, then transforms the simple product functions into the irreducible basis functions using appropriate

Table 1

## Program Input Format for Density Matrix Elements

<u>Variable</u>	<u>Format</u>	<u>Description</u>
NCOMP	I6	Specifies the number of "TERMS" in the particular density matrix element
LDM	I6	The row and column numbers of the matrix element in the form: (i × 100) + j, where i is the row number and j is the column number
COEFF	2E14.7	A complex number specifying the magnitude of the density matrix element
TAG1	I6	The T1 time dependence encoded as (i × 100) + j, representing the $\exp\{2\pi i v_{ij} T1\}$ factor in Eq. II.1
TAG2	I6	Corresponding variable for T2
TAG3	I6	Corresponding variable for D1
TAG4	I6	Corresponding variable for D2
JCOEFF	I6	Encodes information regarding the spin coupling constant J during various precession periods. Should be specified as "111111"



transformation matrices. The eigenbasis of  $\hat{H}_0$  is the set of eigenfunctions  $|I, M_I\rangle |S, M_S\rangle$  of the operators  $\hat{I}^2$ ,  $\hat{I}_z$ ,  $\hat{S}^2$ , and  $\hat{S}_z$  with eigenvalues  $I(I+1)$ ,  $M_I$ ,  $S(S+1)$  and  $M_S$  respectively. Here  $\hat{I}$  is the total spin angular momentum operator for the  $I_m$  spins and  $\hat{S}$  is the total spin angular momentum operator for the  $S_n$  spins. Since the basis functions are never explicitly generated by the program, but the representations of spin angular momentum operators are, the building up process will be illustrated in connection with the representation of the spin operators.

## II.5 Construction of Spin Operator Representation Matrices

The generation of representation matrices for spin angular momentum operators is accomplished by starting with the matrix representation of the required operator for a single spin  $1/2$  nucleus, forming the representation of this operator in an uncoupled product basis and transforming this product representation into the representation in the irreducible basis by appropriate transformation matrices. This process is illustrated by considering the representation of  $\hat{I}_z$  and  $\hat{S}_z$  in  $I_1 S_1$  and  $I_1 S_2$  spin systems.

The matrix representation  $\hat{I}_z$  of the z-component of the spin angular momentum operator for a single spin  $1/2$  system, in the  $\{|1/2, 1/2\rangle, |1/2, -1/2\rangle\}$  basis, is (1)

$$\tilde{z} = (1/2) \begin{bmatrix} 1 & 0 \\ 0 & -1 \end{bmatrix} \quad [2-2]$$

The representation of  $\hat{I}_z$  for the  $I_1 S_1$  spin system is constructed by computing the direct product of  $\tilde{z}$  with a  $2 \times 2$  unit matrix  $\tilde{U}_2$  corresponding to the  $S$  spin, giving

$$\tilde{I}_z = \tilde{z} \otimes \tilde{U}_2 = (1/2) \begin{bmatrix} 1 & 0 & 0 & 0 \\ 0 & -1 & 0 & 0 \\ 0 & 0 & 1 & 0 \\ 0 & 0 & 0 & -1 \end{bmatrix} \quad [2-3]$$

The basis functions  $|I, M_I\rangle |S, M_S\rangle$  are in the order  $(M_I, M_S) = (1/2, 1/2), (-1/2, 1/2), (1/2, -1/2), (-1/2, -1/2)$ . The representation of  $S_z$  is constructed by reversing the order of direct products in Equation [2-3] and is given by

$$\tilde{S}_z = \tilde{U}_2 \otimes \tilde{z} \quad [2-4]$$

A more interesting case, involves the representation of  $S_z$  for the  $I_1 S_2$  system. The representation  $z_2$ , of the  $z$ -component of the spin angular momentum for the  $S_2$  spin subgroup in the uncoupled basis is generated by

$$z_2 = \tilde{z} \otimes \tilde{U}_2 + \tilde{U}_2 \otimes \tilde{z} \quad [2-5]$$



Here the basis functions  $|I, M_I\rangle |S, M_S\rangle$  are arranged in the order  $(M_I, M_S) = (1/2, 1), (-1/2, 1), (1/2, 0), (-1/2, 0), (1/2, -1), (-1/2, -1), (1/2, 0), (-1/2, 0)$  with the first 6 functions associated with the triplet states of the  $S_2$  subsystem, and the last 2 with the singlet state.

Similarly the representation of  $\hat{I}_z$  for the  $I_1 S_2$  spin system can be constructed by taking the direct product of  $z$  with  $U_4$ , a  $4 \times 4$  unit matrix corresponding to  $S_2$  subgroup:

$$\hat{I}_z = z \otimes U_4 \quad [2-8]$$

The matrix representations of other operators  $\hat{I}_x, \hat{I}_y, \hat{S}_x$  and  $\hat{S}_y$  are likewise constructed, building up from their corresponding representations for the single spin  $1/2$  system. The matrices  $D$  for the transformation of spin operators from uncoupled to coupled basis for 2 and 3 spin  $1/2$  subsystems are stored in the program.

## II.6 Computation of the Thermal Equilibrium Density Matrix

The first step in the simulation of any pulse sequence is the specification of the spin system  $I_m S_n$  and the construction of the thermal equilibrium density matrix.

In the high temperature limit, the thermal equilibrium density operator given in Equation [1-33] reduces to

$$\hat{\rho}(0) = (\hat{1} - \hat{H}_0/kT)/N, \quad [2-9]$$

where  $\hat{1}$  is the identity operator and  $N$  is the number of spin states ( $2^{n+m}$  for the  $I_m S_n$  spin system). In the case of weak coupling between the  $I_m$  and  $S_n$  spin groups, the eigenbasis of  $\hat{H}_0$ , constructed in Section II.3, is the set of eigenfunctions  $\{|I, M_I\rangle |S, M_S\rangle\}$  of the operators  $\hat{I}^2$ ,  $\hat{I}_z$ ,  $\hat{S}^2$  and  $\hat{S}_z$  with eigenvalues  $I(I+1)$ ,  $M_I$ ,  $S(S+1)$ , and  $M_S$  respectively. Hence  $\hat{\rho}(0)$  is diagonal in this basis and has elements

$$\rho_{jj}(0) = [1 - (\gamma_I h \nu_I M_{Ij} + \gamma_S h \nu_S M_{Sj})/kT]/N, \quad [2-10]$$

where the contributions from the much smaller spin-spin interaction terms have been neglected, and  $M_{Ij}$  and  $M_{Sj}$  are the eigenvalues of  $\hat{I}_z$  and  $\hat{S}_z$  for the  $j$ -th basis function. Since the term  $\hat{1}/N$  is common to all of the elements of  $\hat{\rho}(0)$ , it is unaffected by rf pulses and decoupling fields, and it gives no contributions to measurable properties of the system, it can therefore be ignored. We take

$$\rho_{jj}(0) \equiv -\Delta_I M_{Ij} - \Delta_S M_{Sj} , \quad [2-11]$$

where  $\Delta_I = (\gamma_I h \nu_I / NkT)$  and  $\Delta_S = (\gamma_S h \nu_S / NkT)$  are constants. Using the above considerations, it can be shown that the thermal equilibrium density matrix for the  $I_1 S_1$  system can be written as

$$\rho_e(0) = (1/2) \begin{bmatrix} \Delta_I + \Delta_S & 0 & 0 & 0 \\ 0 & -\Delta_I + \Delta_S & 0 & 0 \\ 0 & 0 & \Delta_I - \Delta_S & 0 \\ 0 & 0 & 0 & -\Delta_I - \Delta_S \end{bmatrix} . \quad [2-12]$$

In the simulation program,  $\Delta_I = \Delta_S = 100$  for homonuclear spin systems and, for heteronuclear spin systems,  $\Delta_I = 5$  and  $\Delta_S = 100$ .

## II.7 Transformation of the Density Matrix by rf Pulse Operators

During the presence of an rf pulse, the Hamiltonian operator is time dependent. This explicit time dependence of the Hamiltonian operator in the laboratory frame, is removed by a transformation into a coordinate system rotating at an appropriate frequency as shown in Section I.3, and the solution to the equation of motion is given

by Equation [1-18]. An analysis of the effects on an  $I_1S_1$  spin system, on the application of a rf pulse of definite duration to the S nucleus, is illustrated below.

The Hamiltonian for the  $I_mS_n$  spin system, in a frame rotating at frequency  $\nu$  about the z-axis, is

$$\begin{aligned} \hat{H}/h = & -(\nu_I - \nu)\hat{I}_z - (\nu_S - \nu)\hat{S}_z + J\hat{I}_z\hat{S}_z - \\ & (\gamma_I H_1/2\pi)\hat{I}_x - (\gamma_S H_1/2\pi)\hat{S}_x . \end{aligned} \quad [2-13]$$

The last two terms arise from the rf field which has frequency  $\nu$  and strength  $2H_1$ . The spin-spin coupling term can be ignored since its magnitude is very small compared to the Zeeman interaction terms. When  $|\nu_S - \nu|$  is small compared to  $\gamma_S H_1/2\pi$ , the rf field is on-resonance with the S spins, and is far from resonance for the I spins so that the frequency offset term for the S spins and the  $(\gamma_I H_1/2\pi)\hat{I}_x$  term can be ignored. The effective Hamiltonian then reduces to

$$\frac{\hat{H}_{\text{eff}}}{h} = -(\nu_I - \nu)\hat{I}_z - (\gamma_S H_1/2\pi)\hat{S}_x . \quad [2-14]$$

Since the first term in Equation [2-14] describes the free precession of any I spin transverse magnetization, which is not really of interest here and it can be treated

separately, we will ignore this term during the application of the rf pulse. The density matrix after the application of the pulse is therefore related to the initial density matrix by Equation [1-18]. Hence the transformation operator,  $\hat{R}_k(\theta)$ , which describes the rf pulse is

$$\hat{R}_k(\theta) = \exp(i\gamma_S H_1 t \hat{S}_k) = \exp(i\theta \hat{S}_k), \quad [2-15]$$

where  $\theta$  is the angle through which S magnetization is flipped by the pulse. In order to carry out the transformation in Equation [1-18] the matrix representation of the transformation operator  $\exp(i\theta \hat{S}_k)$  in the  $I_1 S_1$  basis set must be computed.

The transformation matrix is constructed by a building up process which is exactly analogous to the process described in Section II.5 for the construction of the spin operator representations. The transformation operator  $\hat{R}_k(\theta)$  for a pulse along the k-axis of the rotating frame, for single spin 1/2 nucleus, is (1,43)

$$\hat{R}_k(\theta) = \exp(i\theta \hat{S}_k) = \hat{1} \cos(\theta/2) + 2i \hat{S}_k \sin(\theta/2). \quad [2-16]$$

The direction index k can take on values  $\pm x$  and  $\pm y$  corresponding to the four phases commonly available on



spectrometers. In general, the transformation matrix for the particular  $I_m$  or  $S_n$  subgroup is obtained by taking direct products of the single spin representations (Equation [2-16]) to produce a representation in the uncoupled simple product basis, then transforming this simple product representation to the irreducible basis using an appropriate transformation matrix. The matrix representation of the pulse for the full  $I_m S_n$  system is obtained by taking the direct product of the transformation matrix for the  $I_m$  subgroup with a  $2^n \times 2^n$  unit matrix (pulse on I nuclei only), the direct product of a  $2^m \times 2^m$  unit matrix with the transformation matrix for the  $S_n$  subgroup (pulse on S nuclei only), or the direct product of the transformation matrix for the  $I_m$  subgroup with the transformation matrix for the  $S_n$  subgroup (pulses to both I and S nuclei in a homonuclear system).

The case of an  $I_1 S_1$  system shall be considered. The pulse matrix  $R_x(\theta)$  for a rf pulse applied along the x-axis of the rotating frame for a single spin 1/2 nucleus, in the  $\{|1/2, 1/2\rangle, |1/2, -1/2\rangle\}$  basis, is

$$R_x(\theta) = \begin{bmatrix} C & iS \\ iS & C \end{bmatrix}, \quad [2-17]$$

where  $C = \cos(\theta/2)$  and  $S = \sin(\theta/2)$ . By analogy with Equation [2-4], the direct product of  $\underline{U}_2$  with  $\underline{R}_X(\theta)$  yields the pulse transformation matrix  $\underline{R}_{Sx}(\theta)$  for the full  $I_1S_1$  system:

$$\underline{R}_{Sx}(\theta) = \underline{U}_2 \otimes \underline{R}_X(\theta) = \begin{bmatrix} C & 0 & iS & 0 \\ 0 & C & 0 & iS \\ iS & 0 & C & 0 \\ 0 & iS & 0 & C \end{bmatrix} \quad [2-18]$$

For the rf pulse applied to the I spins, the corresponding transformation matrix  $\underline{R}_{Ix}(\theta)$  is constructed by reversing the order of direct products:

$$\underline{R}_{Ix}(\theta) = \underline{R}_X(\theta) \otimes \underline{U}_2 \quad [2-19]$$

If the rf pulse affects both nuclei (a homonuclear spin system), the corresponding transformation matrix is

$$\underline{R}_{ISx}(\theta) = \underline{R}_X(\theta) \otimes \underline{R}_X(\theta) = \begin{bmatrix} C^2 & iCS & iCS & -S^2 \\ iCS & C^2 & -S^2 & iCS \\ iCS & -S^2 & C^2 & iCS \\ -S^2 & iCS & iCS & C^2 \end{bmatrix} \quad [2-20]$$

since both spins experience the effects of the pulse.

Pulse representation matrices for larger spin systems are also built up in a similar stepwise manner in exact analogy to the construction of spin operators described in Section II.6.

The subprogram PULSES, which handles the rf pulse transformations, analyzes the input command to identify the nuclei to which the rf pulse is to be applied, the duration of the rf pulse, and the direction in the rotating frame along which the rf pulse is to be applied (referred to as the phase of the rf pulse). The appropriate pulse transformation matrix is computed and the transformation indicated in Equation [1-18] is carried out, by retrieving the elements of the previous density matrix, one by one and carrying out the matrix multiplications of Equation [1-18]. After each element of the final density matrix has been computed, a preliminary simplification and organization of the terms of the density matrix element are carried out. At the end of the transformation procedure, bookkeeping information concerning the final density matrix, such as the start index and size in the "data array", is updated in the "status array".

## II.8 Transformation of the Density Matrix During Free Precession Periods

During a free precession period, the spin Hamiltonian is time independent, and the density matrix in the rotating frame evolves according to Equation [1-11]. The spin Hamiltonian during a free precession period is given as

$$\frac{\hat{H}}{\hbar} = -\nu_I \hat{I}_z - \nu_S \hat{S}_z + J \hat{I}_z \hat{S}_z \quad [2-21]$$

Computation of the matrix representation of the exponential operator  $\exp\{-i\hat{H}(t_2-t_1)/\hbar\}$  is relatively straightforward, since the  $\{|I, M_I\rangle |S, M_S\rangle\}$  basis set is an eigenbasis of  $\hat{H}$ . The representation matrix is diagonal, and has elements

$$\langle j | \exp[-i\hat{H}(t_2-t_1)/\hbar] | j \rangle = \exp[-2\pi i E_j(t_2-t_1)] \quad [2-22]$$

where  $E_j$  is the energy (in Hz) of the  $j$ th state. It can be shown that the effect of the transformation in Equation [1-11], is to change the density matrix elements as

$$\rho_{pq}(t_2) = \rho_{pq}(t_1) \exp[2\pi i \nu_{pq}(t_2-t_1)] \quad [2-23]$$

where  $\nu_{pq} = E_q - E_p$ , is the frequency of the transition between the states  $p$  and  $q$ .

As pointed out in Section II.3, the time-dependence of the elements of the density matrix is represented by an encoded pair of indices which specify the states whose energy separation corresponds to the frequency of oscillation during a particular time interval. During a free precession period of duration  $T_1$  (where  $T_1 = t_2 - t_1$ ), for example, the terms in  $\rho_{pq}$  will all be multiplied by  $\exp(2\pi i \nu_{pq} T_1)$  so that the encoded integer array associated with the  $T_1$  time domain must be updated by incorporating the encoded integer pair  $p, q$  into each term in  $\rho_{pq}$ .

## II.9 Transformation of Density Matrix During Broad-Band Decoupling

It will be shown in Chapter III that the behaviour of the density matrix, when a noise decoupling field is applied at the resonance frequency for the  $S$  nuclei, is described by

$$\rho_{pq}(t_2) = \exp[2\pi i \nu_{pq}(t_2 - t_1)] \sum_{p'} \sum_{q'} \rho_{p'q'}(t_1) P_{p'q';pq}$$

[2-24]

where the  $P_{p'q';pq}$  are numerical coefficients given in Section III.3 and  $\nu_{pq}$  is the "decoupled frequency" corresponding to  $\nu_{pq}$  (i.e. the frequency of the transition from state  $p$  to state  $q$  in the absence of scalar spin-spin coupling between the nuclei I and S).

In the implementation of the decoupling subprogram, DECOPL, the coefficients  $P_{p'q';pq}$  are grouped into a number of small matrices and stored in the subprogram. The manipulations of the density matrix data structure for a decoupling period are straightforward - one computes the appropriate linear combinations, then updates the encoded integer array associated with the decoupling time variable in the same way as for a free precession period. In addition, a flag is set to indicate to the output stages of the program that the spin-spin coupling constant  $J$  is to be set to zero in this time period, so that decoupled frequencies will be computed at that stage.

## II.10 Computation and Simplification of Signal Expressions

The signal measured by the receiver in NMR experiments is proportional to the transverse components of the magnetization for a particular type of nuclei. The expression for the physical observable  $O$ , is given by the Equation [1-6]. In NMR experiments, the physical

observables  $Q$  are either the individual transverse components, for example in the case of I spins  $\langle I_x \rangle$  or  $\langle I_y \rangle$ , or, in quadrature detection mode, the complex components formed from these transverse components. The various complex magnetizations that can be formed from these transverse components are  $\langle I_x + iI_y \rangle$ ,  $\langle I_y + iI_x \rangle$ ,  $\langle I_{-x} + iI_{-y} \rangle$  and  $\langle I_{-y} + iI_{-x} \rangle$ .

The simulation of the receiver in NMR experiments is accomplished by constructing a matrix representation of the appropriate spin angular momentum operator  $\hat{I}_x$ ,  $\hat{I}_y$ ,  $\hat{I}_x + i\hat{I}_y$ ,  $\hat{I}_y + i\hat{I}_x$ ,  $\hat{I}_{-x} + i\hat{I}_{-y}$ ,  $\hat{I}_{-y} + i\hat{I}_{-x}$  (spin I magnetizations only),  $\hat{S}_x$ ,  $\hat{S}_y$ ,  $\hat{S}_x + i\hat{S}_y$ ,  $\hat{S}_y + i\hat{S}_x$ ,  $\hat{S}_{-x} + i\hat{S}_{-y}$ ,  $\hat{S}_{-y} + i\hat{S}_{-x}$  (spin S magnetizations only), or  $\hat{I}_x + \hat{S}_x$ ,  $\hat{I}_y + \hat{S}_y$ ,  $(\hat{I}_x + \hat{S}_x) + i(\hat{I}_y + \hat{S}_y)$ ,  $(\hat{I}_y + \hat{S}_y) + i(\hat{I}_x + \hat{S}_x)$ ,  $(\hat{I}_{-x} + \hat{S}_{-x}) + i(\hat{I}_{-y} + \hat{S}_{-y})$ ,  $(\hat{I}_{-y} + \hat{S}_{-y}) + i(\hat{I}_{-x} + \hat{S}_{-x})$  (both I and S magnetizations for homonuclear systems). The construction of the matrix representation of a spin angular momentum operator is discussed in Section II.5. In homonuclear systems, the sum of the representations for the spin operators for the I and S spins is constructed. The calculation of the magnetization is effected using Equation [1-6], with  $\hat{Q}$  replaced by the appropriate spin angular momentum as listed above. For completeness, the simulation program allows one to "measure" the z-component of the magnetizations although these cannot be measured directly with a spectrometer.

The subprogram MEASUR, which carries out the signal computation, first analyses the input command to determine the magnetization component which is to be extracted for the specified spins. It then constructs the matrix representations of the appropriate spin angular momentum operators. In the computation of the magnetization components, since only the trace of the product of  $\rho$  and the appropriate spin operator matrix is needed, the diagonal elements of the product matrix are computed and summed together. Simplification of these terms is carried out by recognizing the relationships between  $\exp(i\phi) \pm \exp(-i\phi)$  and  $\cos \phi$  and  $\sin \phi$ , where  $\phi$  refers to the encoded integer arrays associated with the time variables T1, T2, D1 and D2. The subprogram SMPFLY scans through the rows of terms in the "data array" associated with each element of the density matrix and picks out pairs of rows which can be simplified and can be expressed in terms of sine or cosine functions. The information regarding the type of the function (i.e. "sine", "cosine" or "exp") is encoded in appropriate integer arrays for communication to the printing subprograms. Furthermore, the four integer arrays associated with the four time variables are decoded in the output stage and the frequencies  $\nu_{pq}$  associated with each time domain are given as explicit linear combinations of  $\nu_I$ ,  $\nu_S$  and  $J$  so that the time dependence



can be ascribed clearly to the chemical shift offsets and/or spin-spin coupling. This explicit dependence on  $\nu_I$ ,  $\nu_S$  and  $J$  is also given when the density matrix is itself output. It should be pointed out that  $\nu_I$  and  $\nu_S$  in the output represent offsets from the corresponding transmitter frequencies. The justification for this interpretation of frequency terms is discussed in the next section.

#### II.11 Identification of $\nu_I$ and $\nu_S$ as Frequency Offsets from Transmitter

It was indicated above that the frequencies  $\nu_I$  and  $\nu_S$  in the output represent offsets from the corresponding transmitter frequencies. In this section, a detailed analysis of a simple example will be presented to illustrate that despite the numerous transformations between various frames of reference required in the density matrix treatment, the signal output by the simulation program is justified if the frequency terms in the output are considered as offsets from corresponding transmitter frequencies.

It is important to recognize that the density matrix and the Hamiltonian matrix which appear in Equation [1-17] must be in the same frame of reference. The

straightforward procedure for relating the density matrix in the laboratory frame before and after a pulse requires the transformations

$$\hat{\rho}_{(t_1)}^{(\text{lab})} \rightarrow \hat{\rho}_{(t_1)}^{*(\text{rot})} \xrightarrow{\text{Pulse Transformation}} \hat{\rho}_{(t_1+\tau)}^{*(\text{rot})} \rightarrow \hat{\rho}_{(t_1+\tau)}^{(\text{lab})} \quad [2-25]$$

As an illustration, the evolution of density matrix will be followed in detail, by carrying out the sequence of transformations in Equation [2-25] for each pulse in the sequence shown in Figure 2 applied to the  $I_1S_1$  spin system. This pulse sequence is employed for the determination of pulse lengths on nuclei, when they are not under direct observation (44,45).

The elements of the density matrix in laboratory and rotating frames at time  $t$  are related by

$$\rho_{pq}^{(\text{rot})}(t) = \rho_{pq}^{(\text{lab})}(t) \exp[-2\pi i(M_p - M_q)vt], \quad [2-26]$$

where  $M_p$  and  $M_q$  are the eigenvalues of the  $z$ -component of the total angular momentum operator  $\hat{I}_z + \hat{S}_z$  in the  $p$  and  $q$  states. At  $t = 0$ , the laboratory and rotating frames coincide and the initial density matrix is

8

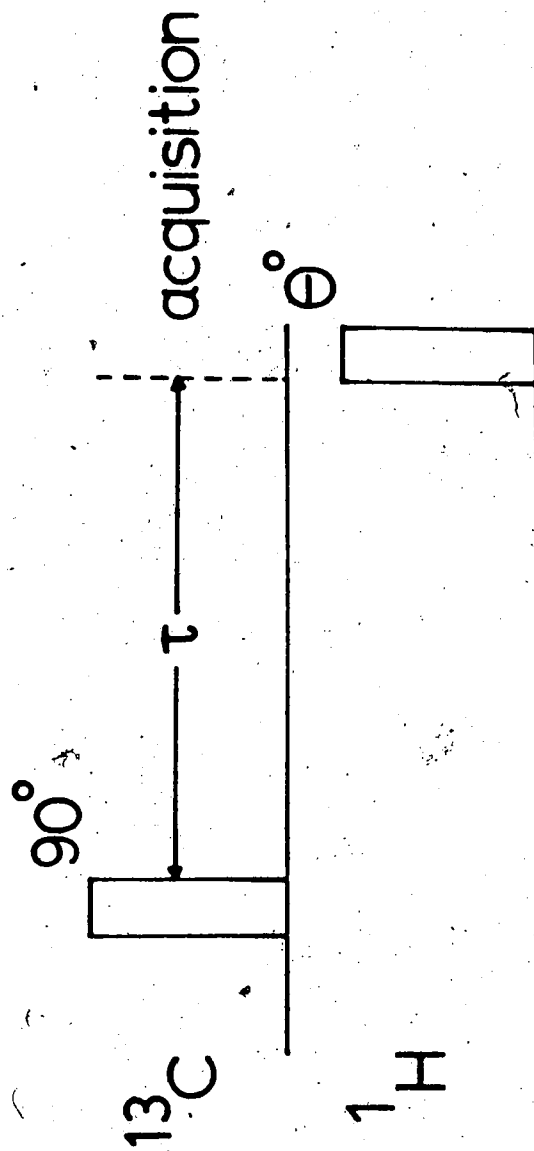


Figure 2. Pulse sequence for calibration of pulse width. The delay  $\tau$  is to be set for  $1/(2J_{\text{CH}})$ . When  $\theta = 90^\circ$  for the proton pulse, the carbon signals will have minimum intensity.

$$\rho^{(lab)}(0) = \rho^{(rot)}(0) = \begin{bmatrix} \Delta + \delta & 0 & 0 & 0 \\ 0 & \Delta - \delta & 0 & 0 \\ 0 & 0 & -\Delta + \delta & 0 \\ 0 & 0 & 0 & -\Delta - \delta \end{bmatrix} \quad [2-27]$$

where  $\Delta$  and  $\delta$  are the parameters defined above. A  $90^\circ$  pulse is applied, at time zero at the I resonance frequency  $\nu_i^0$  and the density matrix in the frame rotating at  $\nu = \nu_i^0$ , after the pulse is

$$\rho^{(rot)}(\tau_p) = \begin{bmatrix} \Delta & i\delta & 0 & 0 \\ -i\delta & \Delta & 0 & 0 \\ 0 & 0 & -\Delta & i\delta \\ 0 & 0 & -i\delta & -\Delta \end{bmatrix} \quad [2-28]$$

where  $\tau_p$  is the time required to effect the  $90^\circ$  pulse. Transforming to the laboratory frame, we obtain

$$\rho^{(lab)}(\tau_p) = \begin{bmatrix} \Delta & a & 0 & 0 \\ a^* & \Delta & 0 & 0 \\ 0 & 0 & -\Delta & a \\ 0 & 0 & a^* & -\Delta \end{bmatrix} \quad [2-29]$$

where  $a = i\delta \exp[2\pi i \nu_i^0 \tau_p]$  and the asterisk denotes complex conjugation. According to Figure 2, the system is

allowed to precess freely for a period  $t_1$  during which the density matrix evolves under the time independent Hamiltonian and becomes

$$\rho_{(lab)}(\tau_p + t_1) = \begin{bmatrix} \Delta & b & 0 & 0 \\ b^* & \Delta & 0 & 0 \\ 0 & 0 & -\Delta & c \\ 0 & 0 & c^* & -\Delta \end{bmatrix} \quad [2-30]$$

where  $b = i\delta \exp[2\pi i(\nu_i^o \tau_p + \nu_{12} t_1)]$ ,  
 $c = i\delta \exp[2\pi i(\nu_i^o \tau_p + \nu_{34} t_1)]$ , and  $\nu_{ij}$  is the frequency of the transition between states  $i$  and  $j$ . At the end of the precession period, a  $90^\circ$  pulse is applied at the S resonance frequency. To handle this, the density matrix must be transformed into the frame rotating at the frequency  $\nu_S^o$  of the S transmitter to facilitate the transformation by the S pulse. The density matrix in the S rotating frame before the pulse is given by

$$\rho_{(rot)}(\tau_p + t_1) = \begin{bmatrix} \Delta & d & 0 & 0 \\ d^* & \Delta & 0 & 0 \\ 0 & 0 & -\Delta & e \\ 0 & 0 & e^* & -\Delta \end{bmatrix} \quad [2-31]$$

where  $d = i\delta \exp\{2\pi i[v_I^0 \tau_p + v_{12} t_1 - v_S^0(\tau_p + t_1)]\}$ ,

$e = i\delta \exp\{2\pi i[v_I^0 \tau_p + v_{34} t_1 - v_S^0(\tau_p + t_1)]\}$ .

For the sake of simplicity, only the density matrix elements of interest  $\rho_{12}$  and  $\rho_{34}$  which are associated with transverse I magnetization will be considered further.

After the application of the  $90^\circ_x$  S pulse, the elements  $\rho_{12}$  and  $\rho_{34}$  in the S rotating frame are given by

$$\rho_{12}^{(\text{rot})}(\tau_p + t_1 + \tau_{p'}) = \rho_{34}^{(\text{rot})}(\tau_p + t_1 + \tau_{p'}) =$$

$$i\delta \exp\{2\pi i(v_I^0 \tau_p + v_S^0(\tau_p + t_1))\} \{ \exp(2\pi i v_{12} t_1) + \exp(2\pi i v_{34} t_1) \}.$$

[2-32]

Transformation of these density matrix elements into the laboratory frame yields

$$\rho_{12}^{(\text{lab})}(\tau_p + t_1 + \tau_{p'}) = \rho_{34}^{(\text{lab})}(\tau_p + t_1 + \tau_{p'}) =$$

$$i\delta \exp\{2\pi i(v_I^0 \tau_p + v_S^0 \tau_{p'})\} \{ \exp(2\pi i v_{12} t_1) + \exp(2\pi i v_{34} t_1) \},$$

[2-33]

where  $\tau_{p'}$  denotes the duration of the  $90^\circ_x$  S pulse. During the signal acquisition period  $t_2$ , the density matrix elements develop further time dependence as

$$\rho_{12}^{(\text{lab})}(\tau_p + t_1 + \tau_{p'} + t_2) = i\delta \exp\{2\pi i(\nu_I^0 \tau_p + \nu_S^0 \tau_{p'})\} \times$$

$$\{\exp(2\pi i\nu_{12}t_1) + \exp(2\pi i\nu_{34}t_1)\} \exp(2\pi i\nu_{12}t_2),$$

[2-34]

$$\rho_{34}^{(\text{lab})}(\tau_p + t_1 + \tau_{p'} + t_2) = i\delta \exp\{2\pi i(\nu_I^0 \tau_p + \nu_S^0 \tau_{p'})\} \times$$

$$\{\exp(2\pi i\nu_{12}t_1) + \exp(2\pi i\nu_{34}t_1)\} \exp(2\pi i\nu_{34}t_2).$$

Since the heterodyne receiver in an NMR spectrometer measures the I magnetization in the rotating frame,  $\rho_{12}$  and  $\rho_{34}$  in the I rotating frame are required:

$$\rho_{12}^{(\text{rot})}(\tau_p + t_1 + \tau_{p'} + t_2) = i\delta \exp\{2\pi i(\nu_S \tau_{p'} - \nu_I \tau_p)\} \times$$

$$\{\exp(2\pi i\Delta\nu_{12}t_1) + \exp(2\pi i\Delta\nu_{34}t_1)\} \times \exp(2\pi i\Delta\nu_{12}t_2),$$

[2-35]

$$\rho_{34}^{(\text{rot})}(\tau_p + t_1 + \tau_{p'} + t_2) = i\delta \exp\{2\pi i(\nu_S \tau_{p'} - \nu_I \tau_p)\} \times$$

$$\{\exp(2\pi i \Delta v_{12} t_1) + \exp(2\pi i \Delta v_{34} t_1)\} \times \exp(2\pi i \Delta v_{34} t_2)$$

where  $\Delta v_{ij}$  is the frequency offset of the transition frequency  $v_{ij}$  from the transmitter frequency  $v_I^{\circ}$ ,

$$\Delta v_{ij} = v_{ij} - v_I^{\circ}$$

The I spin signal  $I_x + iI_y$  measured is given by

$$\text{Signal} \propto i\delta\{\exp(2\pi i \Delta v_{12} t_1) + \exp(2\pi i \Delta v_{34} t_1)\} \times$$

$$\exp\{2\pi i (v_S^{\circ} \tau_p - v_I^{\circ} \tau_p)\} \times \quad [2-36]$$

$$\{\exp(2\pi i \Delta v_{12} t_2) + \exp(2\pi i \Delta v_{34} t_2)\}$$

The factor involving  $\tau_p$  and  $\tau_p'$  is just a phase shift and this is compensated in real experiments by "phasing" the spectrum to get pure absorption mode presentation. Since this phase factor is the same for all signals, we can ignore it and write



$$\text{Signal} \propto i\delta\{\exp(2\pi i\Delta\nu_{12}t_1) + \exp(2\pi i\Delta\nu_{34}t_1)\} \times$$

$$[\text{exp}(2\pi i\Delta\nu_{12}t_2) + \text{exp}(2\pi i\Delta\nu_{34}t_2)] \quad [2-37]$$

The signal expression in Equation [2-37] obtained from the above analysis, shows that the transition frequencies in the measured magnetizations appear as offsets from the respective transmitter frequencies. The signal output by the simulation program is exactly similar to Equation [2-37], but the program represents the difference  $\nu_I - \nu_I^0$  as  $\nu_I$  (similarly  $\nu_S - \nu_S^0$  as  $\nu_S$ ). Hence  $\nu_S$  and  $\nu_I$  are to be interpreted as offsets from the corresponding transmitter frequencies. The transformations of the density matrix between various frames of reference, described above, are not really necessary since any phase shifts built up in the duration of the pulses are unimportant. These phase shifts do not arise if all pulses are taken to be infinitely short so that laboratory and rotating frames coincide for the duration of a pulse. In this view, all calculations are performed in the laboratory frame, but the frequencies which appear in the signals must be interpreted as offsets from the respective transmitter frequencies.

$m = -i\delta \exp\{2\pi i(VI-J/2)T_2\} [1 + \exp\{2\pi i J D_1\}]$ . The carbon signals are then given by

$$\begin{aligned} \text{Signal} \propto & -i(\delta/4) [\exp\{2\pi i(VI+J/2)T_2\} \{1 + \exp(2\pi i J D_1)\} \\ & + \exp\{2\pi i(VI-J/2)T_2\} \{1 + \exp(-2\pi i J D_1)\}] , \quad [4-28] \end{aligned}$$

which gives rise to a  $2 \times 2$  parallelogram of peaks with intensity 1:1:1:1, in the 2D contour map. The density matrix simulations for the coupled spectra for  $\text{CH}_2$  and  $\text{CH}_3$  systems are given in Figures 36 and 37 respectively. For  $\text{CH}_2$  and  $\text{CH}_3$  systems, one obtains from the calculation, a  $3 \times 3$  and  $4 \times 4$  parallelogram of peaks, the positions and relative intensities of which, are in accordance with experimental results for 2-butanol, (Figure 34).

#### IV.3 Summary

Simulations of several pulse sequences applied to a variety of spin systems were included in this chapter, in order to demonstrate some of the applications of the simulation program. The utility of various features of the program, such as rf pulses of any given flip angle, broadband decoupler irradiation facility and the phase cycling feature, were emphasized in the examples. The

OUTPUT FOR SEQUENCE C (COUPLED) ON CH2 SYSTEM

Carbon Signals During Acquisition ( Decoupler Gated Off )

SIGNAL =	+( 0.0	-0.833)=EXPI(2*PI*(	1.00 VI	1.00 J	)=T2 )
	+( 0.0	-0.833)=EXPI(2*PI*(	1.00 VI	1.00 J	)=T2 )
		EXPI(2*PI*(		1.00 J	)=D1 )
	+( 0.0	-0.833)=EXPI(2*PI*(	1.00 VI	1.00 J	)=T2 )
		EXPI(2*PI*(		2.00 J	)=D1 )
	+( 0.0	-0.833)=EXPI(2*PI*(	1.00 VI	-1.00 J	)=T2 )
		EXPI(2*PI*(		-1.00 J	)=D1 )
	+( 0.0	-3.333)=EXPI(2*PI*(	1.00 VI		)=T2 )
	+( 0.0	-0.833)=EXPI(2*PI*(	1.00 VI		)=T2 )
		EXPI(2*PI*(		1.00 J	)=D1 )
	+( 0.0	-0.833)=EXPI(2*PI*(	1.00 VI	-1.00 J	)=T2 )
		EXPI(2*PI*(		-2.00 J	)=D1 )
	+( 0.0	-0.833)=EXPI(2*PI*(	1.00 VI	-1.00 J	)=T2 )
		EXPI(2*PI*(		-1.00 J	)=D1 )
	+( 0.0	-0.833)=EXPI(2*PI*(	1.00 VI	-1.00 J	)=T2 )

Figure 36. Output data from simulation of gated decoupler pulse sequence C (with coupled acquisition) on CH<sub>2</sub> system.

OUTPUT FOR SEQUENCE C (COUPLED) ON CH<sub>3</sub> SYSTEM

Carbon Signals During Acquisition (Decoupler Gated Off)

SIGNAL =	+( 0.0 , -0.625)*EXPI(2*PI*(	1.00 VI	1.50 J )*T2 )
	+( 0.0 , -0.625)*EXPI(2*PI*(	1.00 VI	1.50 J )*T2 )
	*EXPI(2*PI*(		1.00 J )*D1 )
	+( 0.0 , -0.625)*EXPI(2*PI*(	1.00 VI	1.50 J )*T2 )
	*EXPI(2*PI*(		2.00 J )*D1 )
	+( 0.0 , -0.625)*EXPI(2*PI*(	1.00 VI	1.50 J )*T2 )
	*EXPI(2*PI*(		3.00 J )*D1 )
	+( 0.0 , -0.625)*EXPI(2*PI*(	1.00 VI	0.50 J )*T2 )
	*EXPI(2*PI*(		-1.00 J )*D1 )
	+( 0.0 , -3.125)*EXPI(2*PI*(	1.00 VI	0.50 J )*T2 )
	+( 0.0 , -3.125)*EXPI(2*PI*(	1.00 VI	0.50 J )*T2 )
	*EXPI(2*PI*(		1.00 J )*D1 )
	+( 0.0 , -0.625)*EXPI(2*PI*(	1.00 VI	0.50 J )*T2 )
	*EXPI(2*PI*(		-2.00 J )*D1 )
	+( 0.0 , -0.625)*EXPI(2*PI*(	1.00 VI	-0.50 J )*T2 )
	*EXPI(2*PI*(		-2.00 J )*D1 )
	+( 0.0 , -3.125)*EXPI(2*PI*(	1.00 VI	-0.50 J )*T2 )
	*EXPI(2*PI*(		-1.00 J )*D1 )
	+( 0.0 , -3.125)*EXPI(2*PI*(	1.00 VI	-0.50 J )*T2 )
	+( 0.0 , -0.625)*EXPI(2*PI*(	1.00 VI	-0.50 J )*T2 )
	*EXPI(2*PI*(		1.00 J )*D1 )
	+( 0.0 , -0.625)*EXPI(2*PI*(	1.00 VI	-1.50 J )*T2 )
	*EXPI(2*PI*(		-3.00 J )*D1 )
	+( 0.0 , -0.625)*EXPI(2*PI*(	1.00 VI	-1.50 J )*T2 )
	*EXPI(2*PI*(		-2.00 J )*D1 )
	+( 0.0 , -0.625)*EXPI(2*PI*(	1.00 VI	-1.50 J )*T2 )
	*EXPI(2*PI*(		-1.00 J )*D1 )
	+( 0.0 , -0.625)*EXPI(2*PI*(	1.00 VI	-1.50 J )*T2 )

Figure 37. Output data from simulation of gated decoupler pulse sequence C (with coupled acquisition) on CH<sub>3</sub> system.

experiments simulated in this chapter included DEPT, selective 2D heteronuclear shift correlation, INADEQUATE and 2D gated J- $\delta$  correlation experiments which demonstrate certain unexpected effects of spin decoupling.

INPUT FOR 2D SELECTIVE DEPT EXPT ON C-H2 SYSTEM

```

COMM 2D SELECTIVE DEPT EXPERIMENT ON C-H2 SYSTEM
SPIN11S2
SET PULSC 45.0
PULSSA+X
PRECT1
PULSIB+X
PRECT1
WRDM
PRECD1
SUBSD1=1/( 2J)
PULSSB+X
PULSIA+X
PRECD1
SUBSD1=1/( 2J)
PULSSC+Y
PULSIB+X
PRECD2
SUBSD2=1/( 2J)
DCPLS T2
MEASIXY0
STOP

```

OUTPUT FOR 2D SELECTIVE DEPT EXPT ON C-H2 SYSTEM

Density Matrix After T1 Evolution Period

```

DM ( 1, 1) = + ( -2.500, 0.0 )
DM ( 1, 3) = + ( 0.0, -70.711)*EXPI(2*PI*( 2.00 VS )=T1 )
DM ( 2, 2) = + ( -2.500, 0.0 )
DM ( 2, 4) = + ( 0.0, 70.711)*EXPI(2*PI*( 2.00 VS )=T1 )
DM ( 3, 3) = + ( -2.500, 0.0 )
DM ( 3, 5) = + ( 0.0, 70.711)*EXPI(2*PI*( 2.00 VS )=T1 )
DM ( 4, 4) = + ( 2.500, 0.0 )
DM ( 4, 6) = + ( 0.0, 70.711)*EXPI(2*PI*( 2.00 VS )=T1 )
DM ( 5, 5) = + ( -2.500, 0.0 )
DM ( 6, 6) = + ( 2.500, 0.0 )
DM ( 7, 7) = + ( -2.500, 0.0 )
DM ( 8, 8) = + ( 2.500, 0.0 )

```

Carbon-13 Signals During Decoupled Acquisition

```

SIGNAL = + ( 0.000, 5.000)*EXPI(2*PI*( 1.00 VI )=T2 )
           *EXPI(2*PI*( -1.00 VI )=D1 )
           *EXPI(2*PI*( 1.00 VI )=D2 )
           + (-100.000, -0.000)*EXPI(2*PI*( 2.00 VS )=T1 )
           *EXPI(2*PI*( 1.00 VI )=T2 )
           *EXPI(2*PI*( -1.00 VI )=D1 )
           *EXPI(2*PI*( 1.00 VI )=D2 )
           + (-100.000, -0.000)*EXPI(2*PI*( -2.00 VS )=T1 )
           *EXPI(2*PI*( 1.00 VI )=T2 )
           *EXPI(2*PI*( -1.00 VI )=D1 )
           *EXPI(2*PI*( 1.00 VI )=D2 )

```

Figure 18. Input data and output from the simulation of  $\text{CH}_2$  selective shift correlation experiment. The  $\theta$  pulse (pulse C) has been set to  $45^\circ$ .

PART 2

NUCLEAR RELAXATION STUDY OF  
HEXAMETHYLPHOSPHORAMIDE

---

## CHAPTER V

### DESCRIPTION OF SPIN RELAXATION MECHANISMS

#### V.1 Introduction

In this chapter, some of the important spin relaxation mechanisms and the application of relaxation rate measurements in studying molecular motion in liquids are discussed. Various relaxation mechanisms and their characteristic correlation times are described. Theoretical relaxation rate expressions for various mechanisms are presented. A brief review of the diffusion models for describing molecular motion in liquids is also given. Finally, the objectives of the project are described.

---

#### V.2 Spin Relaxation and Applications of Relaxation Studies

Magnetic relaxation processes are responsible for restoring any non-equilibrium state of the spin system to thermal equilibrium. The interactions which cause magnetic relaxation give rise to a coupling between the



nuclear spin system and the lattice. The lattice acts as a heat sink and comprises the collection of translational, rotational and other degrees of freedom of the molecule (65). The coupling between nuclear spins and lattice acts as a pathway for energy transfer from the spins to the lattice. The coupling between the spin system and the lattice is inherently weak (66), but it is via this coupling that nuclear spin relaxation occurs.

A spin system in a static magnetic field at equilibrium, has the various spin states populated according to the Boltzmann probability distribution. Any perturbation from this equilibrium state causes the system to respond in such a way that the spin populations return to thermal equilibrium values, with the rate of recovery characterized by the time constants  $T_1$  and  $T_2$  (66). The spin-lattice relaxation time  $T_1$  is of more importance in the study of molecular mechanics in liquids than is the spin-spin relaxation time  $T_2$ , due to the ease of measurement of  $T_1$ . The spin-lattice relaxation time describes the recovery of the longitudinal component of the macroscopic magnetization ( $M_z$ ) back to its thermal equilibrium value, while the spin-spin relaxation time  $T_2$  determines the recovery of the transverse components ( $M_x$  and  $M_y$ ) from a nonequilibrium state (66). The longitudinal components and transverse components may have

different rates associated with them since the dynamics of the interaction processes associated with their recovery are different. For the interaction process to be effective in bringing about relaxation, it must be time dependent, must involve the spin of interest and should fluctuate on a time scale such that its frequency is comparable to or greater than the resonance frequency of the spin.  $T_1$  relaxation is affected by high frequency processes, while the  $T_2$  relaxation is influenced by high frequency processes as well as those with low frequencies such as chemical exchange (3). Hence in most cases,  $T_2$  can never be longer than  $T_1$ , however, for molecules tumbling rapidly in liquids, they are often equal. Relaxation effects have been introduced phenomenologically (67) in the classical Bloch equations:

$$\frac{dM_z}{dt} = - \frac{(M_z - M_0)}{T_1},$$

$$\frac{dM_x}{dt} = \omega_0 M_y - \frac{M_x}{T_2},$$

[5-1]

$$\frac{dM_y}{dt} = -\omega_0 M_x - \frac{M_y}{T_2},$$

where  $M_0$  is the thermal equilibrium value of  $M_z$  and  $\omega_0$  is the resonance frequency of the spin.

Magnetic relaxation rate measurements provide a powerful and highly versatile tool for the study of molecular dynamics and structure (3,65,68-71). In the field of molecular dynamics, overall molecular reorientation (66,70), internal motion of molecular fragments in nonrigid systems (72,73) and relative translational motion between molecules (66,70) can be investigated using spin relaxation rate measurements. Relaxation data can be used to test models (77-80) of the microdynamic behavior of liquids. In the determination of organic molecular structure, nuclear spin relaxation measurements play a very useful role, particularly the  $^{13}\text{C}$  spin relaxation rates. Many of these applications have been reviewed by Lyerla et al. (68). The  $^{13}\text{C}$ - $^1\text{H}$  dipolar relaxation rates have been used in spectral assignment since they can provide information regarding the number of protons and their distances to the carbon nucleus. This method is commonly used for distinguishing between protonated and non-protonated carbons. Another common technique which is used in assignment of complex spectra is specific deuteration.

As mentioned above, nuclear spin relaxation can be induced by any mechanism which provides a time dependent magnetic field at the site of the nucleus (3,66). Hence spin relaxation measurements are an excellent tool for

probing molecular dynamics, since molecular motion renders time dependence to many of the spin interactions. More specifically, the relaxation rates are functions of certain quantities known as the correlation times. A correlation time is the time constant characterizing the decay of a particular molecular property, i.e. it is the time in which the system loses memory of its previous state. Hence, for short correlation times, the system loses phase memory quickly and for long correlation times, the phase memory persists for longer periods, i.e. a correlation time can be viewed qualitatively as the time constant characterizing the exponential decay of the correlation function for the particular property.

The physical interactions which give rise to various relaxation processes have different correlation functions. The relaxation rates arising from these interactions are proportional to the spectral density of the interaction, which is just the Fourier transform of the correlation function (66). The spectral density, which is a function of frequency, describes how the power available for relaxation is distributed along the frequency dimension. The spin relaxation rate is related to the spectral density by certain constants characterizing the intensity of the coupling between the spins and the lattice. The importance of the relaxation

rate measurements stems from the fact that if these coupling constants are known, the experimental determination of relaxation rates enables the measurement of the correlation times. To make further connection of the correlation times to the way in which molecules reorient in liquids, one has to refer to appropriate models for the molecular reorientation. The predictions of the particular model, about the relation between different correlation times, are then compared with the experimentally observed variation. Thus relaxation studies are of great importance in testing various theoretical models describing molecular rotation (70).

### V.3 Spin Relaxation Mechanisms

The spin-lattice relaxation rate of a nucleus is the sum of contributions from various relaxation mechanisms. For the general case, the time dependent interaction  $\hat{H}_{int}(t)$  which gives rise to spin relaxation is of the form (66)

$$\hat{H}_{int}(t) = \sum_q \hat{I}_q F_q(t) \quad [5-2]$$

where  $\hat{I}_q$  are spin operators (spin angular momentum operators and bilinear combinations of these operators)

and  $F_q(t)$  are time dependent lattice functions characteristic of the spin-lattice interaction. The time dependence of  $\hat{H}_{int}$  is assumed to be random, and the relaxation rate,  $R_1$ , in the limit of strong motional narrowing, is a linear combination of the form

$$R_1 = 1/T_1 \propto \sum_q a_q |F_q(0)|^2 \tau_q, \quad [5-3]$$

where  $\tau_q$  is the correlation time over which the correlation function  $F_q(t) F_q^*(0)$  has significant amplitude, and  $a_q$  are simple numerical coefficients.  $\tau_q$  is the zero frequency component of the spectral density  $J^{(q)}(\omega)$ , and will be related to the details of molecular motion which modulate  $F_q(t)$ ; and  $|F_q(0)|^2$  will be a measure of the strength of the interaction producing spin relaxation.

Some of the important relaxation mechanisms are intramolecular and intermolecular dipole-dipole interactions, spin-rotation interactions, nuclear quadrupolar interactions and chemical shift anisotropy. In the case of spin 1/2 nuclei, the dipolar interactions and spin-rotation interactions are the major contributors to relaxation, while in nuclei which have a quadrupole moment, the quadrupolar relaxation almost entirely determines the relaxation rate. In certain cases, the

presence of internal motion of groups can influence the relaxation rates due to some of the above mentioned interactions.

a. Dipolar Interactions

Dipolar interactions between two spins on the same molecule acquire time dependence when the angle between the internuclear vector (which is fixed in the molecular frame) and the applied field varies with time as a result of molecular reorientation. Hence the intramolecular dipolar interaction is characterized by a molecular reorientational correlation time  $\tau_0$ . The functions which describe the orientation of the internuclear vector with respect to the applied field are the spherical harmonics of order two, and  $\tau_0$  then describes the decay time for the correlation function of the spherical harmonics. The case of intermolecular dipolar interaction is more complicated since in this case, the time dependence of the interaction originates from two sources: (i) as a result of the relative translational motion of neighboring molecules, the internuclear vector changes its magnitude and direction with time, (ii) molecular reorientation imparts further time dependence to the dipolar interactions. As a result, the translational diffusion coefficient of the molecule enters into the relaxation rate expressions.

Since  $\tau_\theta$  decreases with increasing temperature, the contribution of the dipolar mechanism to  $R_1$  decreases with temperature.

The expression for the relaxation rate,  $R_1^I$ , due to dipolar interactions between two like spins I and S, has been given by Abragam (66) as

$$R_1^I = (3/2) \gamma_I^4 \hbar^2 I(I+1) \{ J^{(1)}(\omega_I) + J^{(2)}(2\omega_I) \}, \quad [5-4]$$

where  $\gamma_I$ , I and  $\omega_I$  represent the magnetogyric ratio, spin and Larmor frequency of the nucleus I. The functions  $J^{(q)}(\omega)$  represent the spectral densities of the dipolar interactions. When I and S are unlike spins, the relaxation rate of nucleus I is given by (66)

$$R_1^I = \gamma_I^2 \gamma_S^2 \hbar^2 S(S+1) \{ (1/12) J^{(0)}(\omega_I - \omega_S) + (3/2) J^{(1)}(\omega_I) + (3/4) J^{(2)}(\omega_I + \omega_S) \}, \quad [5-5]$$

where S is the spin of the S nucleus. The above expressions for the relaxation rates are general in that the spectral densities have not been specified as arising from any specific mechanism such as random rotation or translation.



### 1. Random Rotation

Using the Debye model for random rotation of molecules, the relaxation rate expression for like spins is given by (66)

$$R_1 = (2/5)r^{-6} \gamma_I^2 \hbar^2 I(I+1) \left\{ \tau_\theta / (1 + \omega_I^2 \tau_\theta^2) + 4\tau_\theta / (1 + 4\omega_I^2 \tau_\theta^2) \right\}, \quad [5-6]$$

where  $r$  is the internuclear distance. In the limit of extreme narrowing, i.e.  $\omega_I^2 \tau_\theta^2 \ll 1$ , and for spin  $1/2$  nuclei, Equation [5-6] reduces to

$$R_1 = (3/2) r^{-6} \gamma_I^4 \hbar^2 \tau_\theta. \quad [5-7]$$

For the case of unlike spins  $I$  and  $S$ , the relaxation rate of the  $I$  nucleus at extreme narrowing is given by

$$R_1^I = 4\gamma_I^2 \gamma_S^2 \hbar^2 S(S+1) \tau_\theta / (3 r^6).$$

The correlation time  $\tau_\theta$  is related to the overall rotational diffusion coefficient  $D_r$  by  $\tau_\theta = 1/(6D_r)$ .

In the case where internal motion of groups is present, the internal motion is superimposed on the overall rotation of the molecule and the effective

correlation time  $\tau_{\text{eff}}$  is a function of  $\tau_{\theta}$  and the internal motion correlation time  $\tau_i$ . The dynamics of internal rotation can be studied if  $\tau_i$  can be isolated. The most common method of isolation of  $\tau_i$  is by studying the relaxation rates of two different nuclei such that  $\tau_{\text{eff}}$  and  $\tau_{\theta}$  can be determined independently. The mathematical ground work for isolating the internal motion from the overall rotation was provided by Woessner (72). The applications of this method have been compiled in a review by Lambert et al. (81). If the internal motion is independent of the overall motion and if the internal rotation occurs about the principal axis in the molecular system, its effect can be introduced into the dipolar rate equation by simply adding an internal diffusion constant  $D_i$  ( $D_i = 1/\tau_i$ ) to the diffusion constant  $D_r$  about the principal axis (72). For an isotropic (spherical) system, the intramolecular dipolar relaxation rate in the presence of internal motion is (72)

$$R_1^I = (\gamma_I^2 \gamma_S^2 \hbar^2 / r^6) [A / (6D_r) + B / (6D_r + D_i) + C / (6D_r + 4D_i)], \quad [5-8]$$

where the geometrical constants A, B and C are given by

$A = (3 \cos^2 \Delta - 1)^2 / 4$ ;  $B = 3 \sin^2 \Delta \cos^2 \Delta$ ,  $C = (3/4) \sin^4 \Delta$ ,  
 where  $\Delta$  is angle between the internuclear vector and the  
 internal rotation axis. Equation [5-8] is derived  
 assuming that the internal diffusion is a stochastic  
 process and that all internal rotational orientations have  
 equal probability.

2. Translational Motion

Based on a simple diffusion model of translation,  
 Abragam (66) has given the internuclear dipolar relaxation  
 rate as

$$R_1 = \pi N \gamma_I^4 \hbar^2 / (5 a D_t) \quad [5-9]$$

where  $N$  is the number of spins per  $\text{cm}^3$ ,  $a$  is the  
 hydrodynamic radius of the molecule, and  $D_t$  is the  
 translational diffusion coefficient. This simple model of  
 translation presented by Abragam (66) is in fact quite  
 crude. It fails to consider that, in general,  
 intermolecular dipolar interactions depend on both  
 translational and reorientational motion and that the  
 correlation function for the interaction depends on both  
 angles and distances (82). Features should also be  
 introduced to account for the fact that nuclei are not  
 necessarily at the center of the molecule (82). Another  
 drawback of the simple diffusion model is that the

microscopic detail of the translational motion is obscured since only the gross features of translation are described by the diffusion coefficient  $D_t$  (82). Torrey (83) has introduced random walk theory to calculate the internuclear dipolar relaxation rate and other models are due to Hubbard (84) and Oppenheim and Bloom (85). Hubbard's model takes into account the effects of molecular reorientation on the intermolecular dipolar relaxation rate.

#### b. Spin-Rotation Interaction

The spin-rotation relaxation mechanism is of importance in spin 1/2 systems. In this case, the rotational angular momentum of the molecule produces fluctuating magnetic fields at the site of the nucleus since the electron density in the molecule behaves as a charge system with an angular velocity. Hence the fluctuations of the magnetic fields so produced are determined by the time dependence of the angular momentum of the molecule, with the correlation time  $\tau_J$ . In the case of spherical molecules the relaxation rate is given by (86,87)

$$R_1 = 2kTIC^2\tau_J/\hbar^2 ,$$

where  $I$  is the moment of inertia and  $C$  is the isotropic part of the spin-rotation constant. For symmetric top molecules the relaxation rate expression is given by (88)

$$R_1 = 2kT(C_{\parallel}^2 I_{\parallel} + 2C_{\perp}^2 I_{\perp})\tau_J / (3h^2) \quad [5-11]$$

where the symbols  $\parallel$  and  $\perp$  denote the parallel and perpendicular components of the respective quantities. It has been shown by Hubbard (84) that when  $\tau_J \ll \tau_{\theta}$  and in extreme narrowing, the spin-rotation relaxation rate is proportional to  $\tau_J$ . Hubbard also showed that  $\tau_J$  is proportional to  $D_r/T$ .  $\tau_J$  increases with increasing temperature and hence the spin-rotation mechanism gains importance at higher temperatures.

$\tau_J$  contains information on the molecular collision frequency. The spin-rotation interaction is more important in small symmetrical molecules with weak intermolecular interactions since they tend to possess rather large angular velocities. Determination of the spin-rotation contribution to the total relaxation rate is often difficult since the components of the spin-rotation interaction tensor are not usually known. Flygare (89) has proposed a method which circumvents the task of determining the elements of the spin-rotation tensor experimentally. This method takes advantage of the

relation between spin-rotation constants and chemical shift anisotropy. Spin-rotation constants can be related to chemical shifts since both depend on the electron density distribution in the molecule.

c. Nuclear Quadrupole Interaction

For nuclei with spin  $I > 1/2$  the nuclear quadrupolar contribution dominates the total relaxation rate (3,66,70). Nuclei with spin  $I > 1/2$  possess an electric quadrupole moment (produced by the non-spherical symmetry of the nuclear charge distribution) which interacts with the electric field gradient produced by the surrounding electric charges at the site of the nucleus. The electric field gradient becomes time dependent due to molecular motion. The quadrupole interaction vanishes when the nucleus has an electrical environment which has cubic or higher symmetry (70).

Quadrupolar relaxation is an intramolecular process and provides a very convenient method for determining the reorientational correlation time  $\tau_\theta$  in many cases. For the case of extreme narrowing, the expression for quadrupolar relaxation rate has been given by Abragam (66) as

$$R_1 = \frac{3}{40} \frac{2I+3}{I^2(2I-1)} \left(1 - \frac{\eta^2}{3}\right) \left(\frac{e^2 q Q}{h}\right)^2 \tau_\theta, \quad [5-12]$$

where  $I$  is the spin quantum number,  $(e^2qQ/h)$  is the quadrupole coupling constant, and  $\eta$  is the asymmetry parameter

$$\eta = \frac{\partial^2 V / \partial x^2 - \partial^2 V / \partial y^2}{\partial^2 V / \partial z^2} \quad [5-13]$$

where  $V(x,y,z)$  is the electric potential due to the electrons and  $\{x,y,z\}$  form a molecular coordinate system centred at the nucleus with  $z$  axis chosen to be the principal axis of highest symmetry for the field gradient tensor.

For cases where the asymmetry parameter  $\eta$  and the nuclear quadrupole coupling constant can be determined, Equation [5-12] provides a more convenient and accurate method for determining  $\tau_0$  than the dipolar relaxation rate expression in Equation [5-7]. This is due to the fact that for nuclei with a quadrupole moment, quadrupolar interaction dominates strongly all other mechanisms and there are no intermolecular contributions to the relaxation rate.

If the quadrupolar nucleus is situated in a group which executes internal rotation, the effect of the internal motion is superimposed on the overall reorientational motion. Following Woessner's approach (72)

for internal motion modulation of dipolar interactions, the reorientation correlation time in Equation [5-12] can be replaced (73,126) by an effective correlation time as is done in Equation [5-8].

#### V.4 Brief Review of Rotational Diffusion Models

The earliest of the models for rotational diffusion in liquids was proposed by Debye (90) to describe dielectric relaxation. The Debye model of diffusion was applied to spin relaxation by Bloembergen, Purcell and Pound (91). In the Debye model, the motion of molecules in liquid is pictured as the rotation which macroscopic spheres undergo in a continuous viscous medium. The molecules are acted upon by torques produced by the Brownian motion in the fluid. The model further assumes that the duration of each rotational step or the time between the action of two consecutive torques, is small compared to the time required for the molecule to change its orientation appreciably. This implies that the molecule experiences many changes in angular momentum before it changes its orientation. Since the duration of a rotational step is characterized by the angular momentum correlation time  $\tau_j$  and the overall rotation by the reorientational correlation time  $\tau_\theta$ , the Debye model



assumes that  $\tau_\theta \gg \tau_J$ . Hubbard (84) has used the classical Langevin approach and shown that, for spherical molecules, the reorientational correlation time  $\tau_\theta$  can be related to the angular momentum correlation time  $\tau_J$  by

$$\tau_\theta \tau_J = I_{av}/6kT, \quad [5-14]$$

where  $I_{av}$  is the average moment of inertia of the molecule,  $k$  is the Boltzmann constant and  $T$  is the absolute temperature. The assumption that  $\tau_\theta \gg \tau_J$  is especially objectionable when dealing with the reorientation of spherical or nearly spherical molecules for which it has been found that  $\tau_\theta$  and  $\tau_J$  are of the same order of magnitude (79). Thus the Debye model fails to describe molecular reorientation in the whole range of  $\tau_\theta$  variation with  $\tau_J$ .

When  $\tau_\theta$  and  $\tau_J$  are of comparable magnitude, the molecule reorients through a large angle in a single diffusion step, just as in the dilute gas where molecules rotate freely between collisions. The concept of free rotation and its effect on  $\tau_\theta$  was recognized by many workers (77,92-94), but many of the theories developed were only approximate and were not valid over the entire range of  $\tau_\theta$  and  $\tau_J$ .

The first successful theory which did not incorporate the assumption of small angle diffusion was due to Gordon-

(77). This model has been called the extended diffusion model and he applied it to the case of linear molecules. In the extended diffusion model, no restrictions on the size of reorientational steps were imposed and the model follows the succession of diffusive steps in microscopic detail. The extended diffusion model has been extended to apply for spherical top molecules by McClung (79,95,96), Mountain (97), McClung and Versmold (80); for symmetric top molecules by McClung (98), Fixman and Rider (78), and other workers (99-102); and to asymmetric top molecules by Leicknam et al. (103).

In the extended diffusion model, the molecular motion is examined in detail during each successive diffusion step. It is assumed that the molecule rotates freely between collisions. The collision events are thought to be instantaneous and act as terminators of the diffusive steps. As the result of a collision event, the molecular angular momentum is randomized. This leads to two extreme situations: 1) a case where both the direction and the angular momentum are randomized, referred to as the J-diffusion model and, 2) a case where only the direction of the angular momentum is randomized - the M-diffusion model. The durations of the diffusive steps are assumed to be random and to follow a Poisson distribution with the characteristic time  $\tau_J$ , since each collision event randomizes the components of the angular momentum.

It has been shown (79) that the extended J-diffusion model gives the same results as the Debye model when  $\tau_\theta \gg \tau_J$  and reduces to the perturbed-free-rotor model (104) when  $\tau_\theta \ll \tau_J$ . In the Debye limit ( $\tau_\theta \gg \tau_J$ ), the variation of  $\tau_\theta$  with respect to  $\tau_J$  for the J-diffusion model agrees with Equation [5-14] derived by Hubbard (86). In this limit,  $\tau_\theta$  has an inverse  $\tau_J$  dependence. When  $\tau_\theta \ll \tau_J$ , i.e. at the perturbed-free-rotor limit or dilute gas limit,  $\tau_\theta$  has a direct dependence on  $\tau_J$  (104) and

$$\tau_\theta = \tau_J/5 .$$

[5-15]

The calculations done (79) using the extended diffusion model show the transition from the Debye limit to the perturbed-free-rotor limit. Calculations using the M-diffusion model show that, in the Debye limit,  $\tau_\theta$  is inversely proportional to  $\tau_J$ , but the proportionality constant is different from that in the Debye model. This has been explained (79,105) as due to the fact that Debye model assumes randomization of the magnitude of the angular momentum at each step termination which is not assumed in the extended M-diffusion model. When the anisotropic intermolecular interactions are very weak, the M-diffusion model may be a better approximation because

randomization of the magnitude of the angular momentum at each collisional event is expected to be less probable. The J-diffusion and M-diffusion models are equivalent in the dilute gas limit, and  $\tau_\theta$  exhibits a linear relationship with  $\tau_J$ .

The application of the extended diffusion models has been carried out by comparing the predicted variation of  $\tau_\theta$  with  $\tau_J$ , with the observed variation determined using spin relaxation measurements. Independent determinations of  $\tau_\theta$  and  $\tau_J$  can be made experimentally from relaxation time measurements of different nuclei in suitable molecules. An exhaustive survey of these applications has been given by McClung (105). The extended diffusion model has been applied to linear, spherical top and symmetric top molecules. In most of the applications,  $\tau_J$  was determined from the measurements of spin-rotational contributions to the relaxation rates of spin 1/2 nuclei such as  $^1\text{H}$ ,  $^{19}\text{F}$  and  $^{31}\text{P}$ , and  $\tau_\theta$  was determined from relaxation rates of quadrupolar nuclei. In most cases, the J-diffusion limit of the extended diffusion model was found to give results in quantitative agreement with the experimentally observed  $\tau_\theta$  variation with  $\tau_J$ . The M-diffusion model did not seem to agree very well with most of the experimental observations. The J-diffusion model results however, as expected, did not agree well with

experimental observations on certain linear molecules which have strong intermolecular interactions such as hydrogen bonding. The reasonably widespread success of the J-diffusion model is not surprising since it is capable of yielding results equivalent to the classical Debye diffusion model when  $\tau_{\theta} \gg \tau_J$  and those similar to the results given by dilute gas model at the limit  $\tau_{\theta} \ll \tau_J$ .

#### V.5 Objectives of the Project

The primary objective of this work is to investigate the relative importance of various relaxation mechanisms in the molecule hexamethylphosphoramide,  $O=P[N(CH_3)_2]_3$ , (HMPA) and its deuterated analog (HMPD). Relaxation rates for the  $^{31}P$ ,  $^{14}N$ ,  $^2H$  and  $^1H$  nuclei have been studied over a wide range of temperature. The variation of the translational diffusion coefficient with temperature for hexamethylphosphoramide has been measured to facilitate separation of the contribution to relaxation rates from intermolecular dipolar interactions. It was intended that the reorientational correlation time  $\tau_{\theta}$  and the angular momentum correlation time  $\tau_J$  be determined from the relaxation data. With the knowledge of the coupling constants in the relaxation rate

expressions, from other independent sources, the correlation times characterizing various relaxation processes for different nuclei, can be determined. The knowledge of the variation of the reorientational correlation time  $\tau_\theta$  with the angular momentum correlation time  $\tau_J$  can then be used to test the applicability of the extended diffusion model in describing molecular reorientation in hexamethylphosphoramide.

#### V.6 Summary

A discussion of various spin relaxation mechanisms, their characteristic correlation times and the application of relaxation data in the study of molecular motion has been presented. Quantitative expressions for various relaxation rates were given. Two models describing molecular rotational motion - the Debye model and the extended diffusion model were described. The objectives of the project were also laid out. The next chapter deals with the experimental aspects of spin-lattice relaxation rate determination and the measurement of translational diffusion coefficients. In the following chapter the results and data analysis for HMPA and HMPD are presented.

## CHAPTER VI

### EXPERIMENTAL

#### VI.1 Introduction

This chapter discusses the experimental aspects of the determination of spin-lattice relaxation times and translational diffusion coefficients. The instrumentation used for the measurements is described in brief. Two methods have been adopted for measuring  $T_1$  relaxation times: (i) the inversion recovery experiment and (ii) the triplet sequence which was used for measuring relatively long relaxation times. The last part of the chapter describes the measurement of translational diffusion coefficients by the stationary (time independent) field gradient method.

#### VI.2 Sample Preparation

Hexamethylphosphoramide (Aldrich Chemical Co.) was dried by storing over molecular sieves (Fisher Scientific Co. Type 3A). It was then vacuum distilled into a clean NMR tube attached to the vacuum assembly. The sample was

then degassed using the pump-freeze-thaw technique three times. After degassing, the NMR tube was sealed under vacuum. An identical procedure was used for preparing the sample of the deuterated compound. For the measurement of  $^{31}\text{P}$   $T_1$  in HMPD, a chemical means of deoxygenation of the sample using  $[\text{Co}^{\text{II}}(\text{bipy})_3](\text{ClO}_4)_2$  with sodium borohydride (106) was employed. In an oxygenated solution these compounds give a pale yellow-brown color which changes on removal of oxygen to an extremely oxygen sensitive intense blue color (106). This mixture was added to the HMPD sample and the HMPD was vacuum distilled into an NMR tube. The  $^{31}\text{P}$  relaxation times in this sample did not differ significantly from those in the sample prepared with the pump-freeze-thaw degassing technique.

### VI.3 Instrumentation

The measurement of  $T_1$  values was carried out with a Bruker SXP4-100 high power pulsed NMR spectrometer and a 14 k Gauss Varian Associates electromagnet and V3506 magnetic field flux stabilizer. The Bruker SXP4-100 pulsed spectrometer was operated under the control of a Nicolet 1180 minicomputer along with a Nicolet 293A programmable pulser. The data were stored on a hard disk using a Diablo Disk Drive Unit under the control of the



Nicolet 1180 minicomputer. Analysis of the data was carried out on the minicomputer in the BASIC language and, to a lesser extent, in the Nicolet 1180 Assembler language.

The spectrometer has four independent radio frequency (rf) channels which can be gated on or off by the Nicolet 293A programmable pulser. The phase of the rf pulse can be continuously adjusted in each of the four independent channels. Tuning the spectrometer to the required radio frequency is carried out by adjusting two variable capacitors on the high power amplifier and on the probe arm.

The detector part of the circuitry consists of a preamplifier followed by an amplifier which can be operated in both phase sensitive and diode detection mode. The amplifier, when operating in the diode detection mode, gives a signal which is the square root of the sum of the absorption and dispersion signals. The signal after diode detection is unaffected by moderate changes in magnetic field or radio frequency. Phase sensitive detection has the advantage of linearity of response over the full dynamic range of the amplifier and better signal-to-noise ratio, particularly at low signal intensities. The detector also contains a rf filter with band width adjustable from 100 kHz to 100 Hz.

integrating over about 50 data points in the initial part of the FID. The total acquisition time for the complete FID was typically in the range of 5-25 ms. The signal intensity  $M(\tau)$  for each  $\tau$  value was then fit into an equation of form

$$M(\tau) = A + B \exp(-\tau/T_1) \quad [6-1]$$

using a non-linear least squares analysis algorithm. The computer program was designed to make repetitive  $T_1$  measurements and to calculate the variance and the standard deviation. The diode detection mode was employed for signal acquisition since it was independent of moderate variations in the magnetic field over the period of time required to carry out the repetitive  $T_1$  measurements.

#### b. Triplet Sequence

The triplet sequence (108-111) was used for determination of  $T_1$  values which were relatively long. This sequence is more difficult to carry out and has more stringent requirements concerning the accuracy of the pulse lengths. The advantage of using the triplet sequence is the saving in time, since the wait time is avoided. The triplet sequence can be represented by

$180_x^\circ - \tau - [90_x^\circ - \delta - 180_x^\circ - \delta - 90_x^\circ - \Delta]_n$ , where  $\delta$  must be much smaller than  $T_2$  and was typically about 1 ms, and  $\Delta = \text{acq.time}/n$ , typically about 100 ms. The part of the pulse sequence enclosed by the brackets is repeated  $n$  times (typically  $n = 256$ ). Data were acquired after the first  $90_x^\circ$  pulse of the pulse train enclosed in brackets, using the phase sensitive detection mode. Thus 256 data points were collected during the acquisition time, one data point for each pass through the sequence in brackets.

The triplet sequence is basically similar to the inversion recovery sequence, except that after the signal acquisition period, instead of allowing the magnetization to evolve back to the thermal equilibrium value, the dephased magnetization vectors are refocussed by the  $180_x^\circ$  pulse and rotated back to the  $-Z$  axis by the second  $90_x^\circ$  pulse. This process is then repeated a number of times, thus collecting a data point  $(M(\tau), \tau)$  during each spin echo formation. The data points were fit to Equation [6-1] using the non-linear least squares analysis program. Typical precision of  $T_1$  measurements was about  $\pm 5\%$ ; however, when the  $T_1$  values were very long as in  $^{31}\text{P}$  in HMPD the reproducibility was between  $\pm 5\%$  and  $\pm 10\%$ .

## VI.5 Measurement of Translational Diffusion Coefficients

The translational diffusion coefficient of hexamethylphosphoramide was measured by the stationary field gradient technique (3,112-114). The amplitude of the spin echo from equivalent spins is modulated by diffusion of spins along a magnetic field gradient in the sample. The effective  $T_2$  relaxation time  $T_{2\text{eff}}$  in the presence of a field gradient, contains an extra term involving the diffusion coefficient  $D_t$ . Hence for the experimental determination of  $D_t$ , the transverse relaxation time is measured using the spin echo technique, in the presence and absence of a magnetic field gradient. Both stationary and time dependent field gradients can be employed (3,115,116); however the experiments carried out here were done using the stationary field gradient.

In the first part of the experiment, the relaxation time  $T_2$  of the sample was determined in the absence of any field gradient using the Carr-Purcell-Meiboom-Gill (CPMG) pulse sequence (112,117). The CPMG pulse sequence can be represented as,  $90^\circ_x - \tau/2 - [180^\circ_y - \tau]_n$ , where a train of echoes is generated by the  $180^\circ_y$  pulses and the  $\tau$  time intervals. The  $90^\circ_x$  pulse creates transverse  $y$  magnetization which is allowed to dephase for a time period  $\tau/2$ . A  $180^\circ_y$  pulse is then applied which refocusses

the chemical shift precession and an echo is formed at time  $\tau/2$  after the  $180^\circ$  pulse. This echo is sampled by the A/D convertor of the 1180 computer. A further train of echoes is formed by successive  $180^\circ$  pulses and  $\tau$  delays. The amplitude  $M(t)$  of the spin echo at time  $t$  in the absence of magnetic field gradients is given by (3)

$$M(t) = A + B \exp(-t/T_2) , \quad [6-2]$$

where  $A$  and  $B$  are fitting parameters. In the presence of a field gradient of magnitude  $G$ , the echo amplitude is modified as (3,113)

$$M(t) = A + B \exp\left[-t\left(\frac{1}{T_2} + \frac{\gamma^2 G^2 D_t \tau^2}{2B}\right)\right] , \quad [6-3]$$

where  $D_t$  is the diffusion coefficient and  $\tau$  is the time between the  $180^\circ$  pulses.

The signal was sampled in the phase sensitive detection mode at the maximum of the echo amplitude. For the case where no field gradient was applied, the  $T_2$  value was determined by fitting the data to Equation [6-2] using a non-linear least squares program. The CPMG sequence compensates for pulse length errors by using a  $90^\circ$  phase shifted channel for the  $180^\circ$  pulses. Trial runs of the experiment were carried out during which the relative

phases of pulses were adjusted using the spectrometer rf phase control knobs and the pulse durations were optimized by adjusting the potentiometer knob settings on the Nicolet-1180 computer which control the pulse lengths used by the computer program. The criterion for adjusting the phases and pulse lengths was the symmetry of the spin echoes displayed on an oscilloscope screen.

The second part of the experiment was carried out by measuring the effective relaxation time in the presence of a stationary field gradient. The field gradient was generated by passing current through a pair of copper coils mounted on the aluminum side plates on either side of the probe. The coils consisted of several turns of wire and were arranged so that the current flowed through the two coils in opposite directions. The current to the coils was supplied by a Union Carbide 6 volts No. MS31 cell, and was gated on or off under computer control in synchronization with the CPMG pulse sequence, using programmable level line 7 of the Nicolet 293A pulser.

The field gradient was calibrated using samples of distilled water and benzene whose diffusion constants were given in literature (118,119). The field gradient  $G$  (Gauss/cm) as a function of the current  $I$  (mA) passing through the coils, was obtained using

$$G = mI \quad [6-4]$$

where  $m = 0.155 \pm 0.005$  Gauss  $\text{cm}^{-1}\text{mA}^{-1}$ . The CPMG experiment was first carried out in the absence of the field gradient to determine  $T_2$ .  $T_{2\text{eff}}$  was then obtained from the experiment done in the presence of field gradients, and fitting the data to Equation [6-2]. The field gradient was then calculated from the relation (Equations [6-2] and [6-3]).

$$1/T_{2\text{eff}} = 1/T_2 + \gamma^2 G^2 D_t \tau^2 / 3 \quad [6-5]$$

The field gradient  $G$  was determined for various values of current through the cells, and a calibration chart of field gradient against current was constructed. The current passing through the coils was measured with a Simpson digital multimeter model 461.

The effective relaxation time of hexamethylphosphoramide was then determined in the presence of the field gradient. From the value of  $T_{2\text{eff}}$  the diffusion coefficient  $D_t$  was calculated by substituting the known values of  $T_2$  into Equation [6-5]. The diffusion coefficient of hexamethylphosphoramide was measured over a temperature range 300-440 K. The precision of this method of measurement was approximately  $\pm 10\%$ .

## VI.6 Summary

A description of the experimental aspects of spin relaxation time determination was given in this chapter. The NMR spectrometer system used was described briefly. The spin lattice relaxation time was measured using two techniques: (i) inversion recovery experiment and (ii) triplet sequence. Both of the above methods were described briefly. It was followed by a discussion of the measurement of diffusion coefficient employing the stationary field gradient technique. Brief accounts of the field gradient coil calibration procedure, CPMG experiment and relevant equations were given. The results of the experiments and discussions concerning the separation of relaxation rates into contributions from the individual relaxation mechanisms are presented in the next chapter.



## CHAPTER VII

### RESULTS AND DISCUSSION

#### VII.1 Introduction

The results of the nuclear relaxation and diffusion experiments on HMPA and HMPD and the analysis of the data are presented in this chapter. Section VII.2 deals with the  $T_1$  results for the  $^{31}\text{P}$  nucleus in HMPD and the determination of the angular momentum correlation time. This is followed by the analysis of  $^{14}\text{N}$   $T_1$  data in HMPA, in Section VII.3. Section VII.4 deals with the  $^2\text{H}$  relaxation data analysis. The  $T_1$  data for  $^{31}\text{P}$  nuclei in HMPA, the translational diffusion coefficient results for HMPA, and the delineation of the contributions to the  $^{31}\text{P}$  relaxation rate in HMPA are presented in Section VII.5. The conclusions derived from the study are presented in Section VII.6.

#### VII.2 $^{31}\text{P}$ $T_1$ (HMPD) Results and Analysis

The variation of the spin lattice relaxation time of

$^{31}\text{P}$  in the deuterated analog (HMPD) with temperature was studied from 295 K. to 460 K. The results are shown in Figure 38 and are tabulated in Table 2. The relaxation times were relatively long and the measurements were carried out using the triplet pulse sequence described in Chapter VI. The relaxation time at room temperature was approximately 48 sec and it decreased to about 12 sec at 460 K. To a good approximation, the  $^{31}\text{P}$  relaxation in the deuterated compound can be considered to arise solely from the spin-rotation interaction, since the dipolar interaction between  $^{31}\text{P}$  and  $^2\text{H}$  would be relatively weak. The observed variation of the relaxation rate with temperature in Figure 38 shows the typical characteristic of spin-rotation relaxation: an increase in relaxation rate with increasing temperature. In order to obtain an approximate measure of the  $^{31}\text{P}$ - $^2\text{H}$  dipolar contributions, a calculation using the reorientation correlation time from the  $^2\text{D}$  relaxation rate (see Section VII.4) was carried out, which yielded a value of 370 sec for the dipolar  $T_1$  at room temperature. The experimentally measured  $T_1$  was approximately 48 sec at the same temperature. The contribution of  $^{31}\text{P}$ - $^2\text{H}$  dipolar mechanism to the overall relaxation rate at room temperature, where the dipolar contribution is expected to be larger than at high temperatures, is only slightly larger than the uncertainty

Table 2

Relaxation Data and Results for  $^{31}\text{P}$  in HMPD

Temp. (K)	$T_1$ obs. (sec)	$\tau_J$ obs. ( $\times 10^{14}$ sec)	$\tau_J$ calc. ( $\times 10^{14}$ sec)
294.8	48	4.3	4.1
300.6	42	4.9	4.3
312.6	40	5.0	4.8
313.0	38	5.0	4.8
327.2	39	4.8	5.3
327.8	37	5.0	5.4
333.2	33	5.7	5.6
340.2	32	5.7	5.8
350.1	29	6.0	6.2
359.2	26	6.5	6.6
369.2	25	6.6	7.0
370.5	25	6.7	7.0
384.5	20	7.8	7.6
385.4	21	7.6	7.6
400.2	18	8.4	8.2
406.8	18	8.2	8.5
409.9	17	8.9	8.6
420.4	16	9.1	9.0
425.1	15	9.5	9.2
430.4	15	9.4	9.5
445.7	13	10.6	10.1
450.5	13	10.3	10.3
460.9	12	11.1	10.7

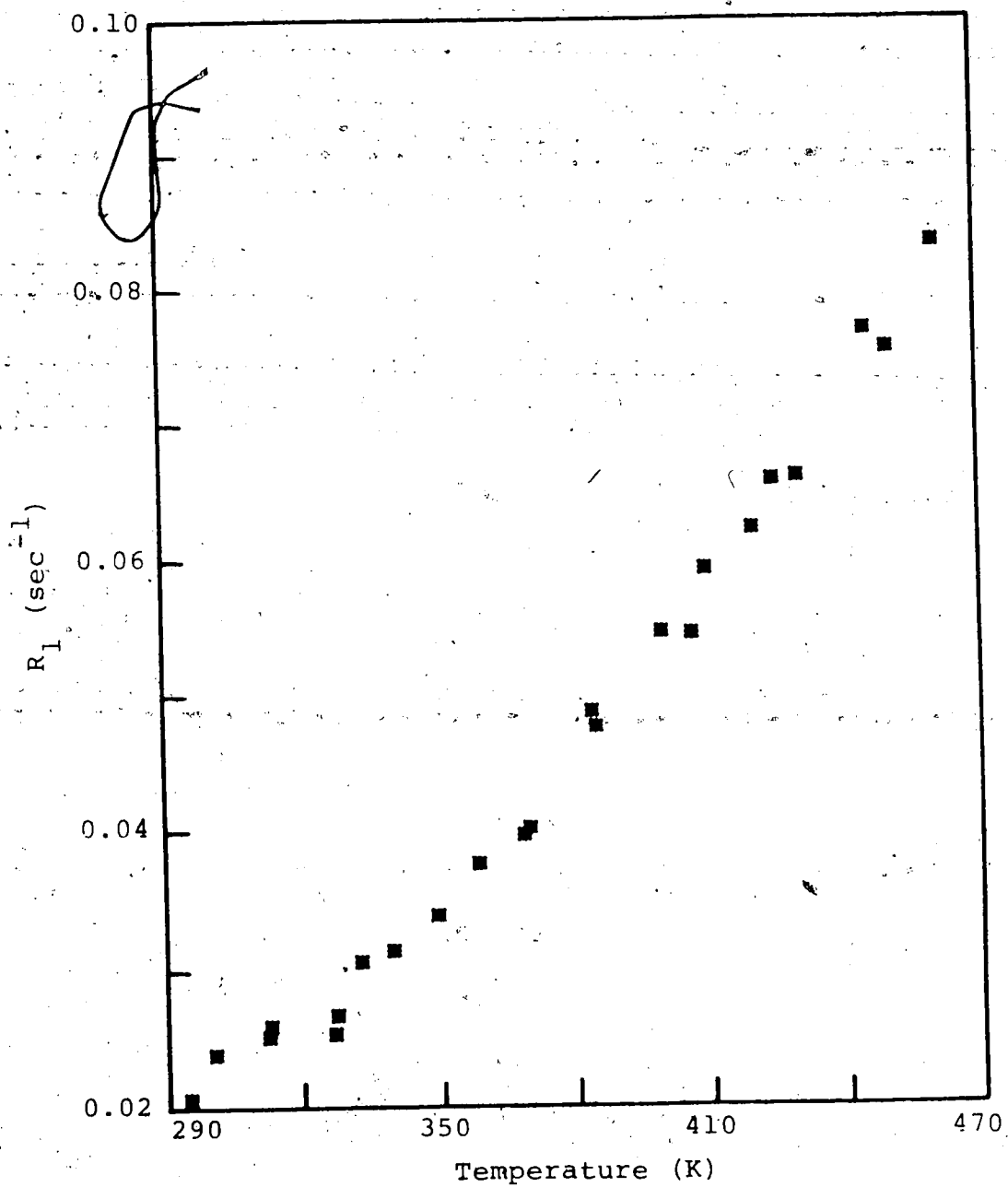


Figure 38. Observed relaxation rates of  $^{31}\text{P}$  in HMPD. The  $T_1$  relaxation times were measured with the triplet pulse sequence.

in the  $T_1$  measurements. Similar calculations of the dipolar interactions with  $^{14}\text{N}$  nuclei, yields a relaxation time of approximately 830 sec for  $^{31}\text{P}$  nucleus at room temperature. Hence dipolar contributions to the  $^{31}\text{P}$  relaxation in HMPD can be neglected.

It is possible to extract the angular momentum correlation time  $\tau_J$  from the observed variation of  $^{31}\text{P}$   $T_1$  values with temperature in the deuterated compound using Equation [5-11], provided that  $C_{\parallel}$  and  $C_{\perp}$ , the parallel and perpendicular components of the spin-rotation interaction tensor, and  $I_{\parallel}$  and  $I_{\perp}$ , the corresponding moments of inertia of HMPD are known. The moments of inertia  $I_{\parallel}$  and  $I_{\perp}$  of HMPD were determined from the x-ray crystal structure data reported by Le Carpentier, Schlupp and Weiss (120) for the compounds  $\text{MoO}(\text{O}_2)_2\text{PO}[\text{N}(\text{CH}_3)_2]_3\text{H}_2\text{O}$  and  $\text{MoO}(\text{O}_2)_2\text{PO}[\text{N}(\text{CH}_3)_2]_3\text{C}_5\text{H}_5\text{N}$ . Average values of the bond lengths and bond angles in the two compounds, the C-H distance ( $1.101 \times 10^{-8}$  cm) and the H-C-H tetrahedral angle ( $109^\circ 28'$ ) were used in the calculation of moments of inertia. The average moments of inertia were calculated to be:  $I_{\parallel} = 1.31 \pm 0.02 \times 10^{-37}$  g cm<sup>2</sup> and  $I_{\perp} = 0.98 \pm 0.01 \times 10^{-37}$  g cm<sup>2</sup>.

The components of the spin-rotation constant tensor were determined from  $^{31}\text{P}$  chemical shifts utilizing the relationship between spin-rotation constants and the

paramagnetic part of the chemical shift (89). Flygare and Goodisman (121) have shown that the paramagnetic part of the chemical shift and the components of the spin-rotation tensor are related by

$$\sigma_{av} = \sigma_{av}^d(\text{free atom}) + \frac{|e|\hbar}{6\pi mc\mu_0 g} (M_{xx}I_x + M_{yy}I_y + M_{zz}I_z) , \quad [7-1]$$

where  $\sigma_{av}$  is the average chemical shift,  $\sigma_{av}^d(\text{free atom})$  is the free-atom diamagnetic susceptibility,  $e$  is the electron charge,  $m$  is the electron mass,  $c$  is the speed of light,  $\mu_0$  is the nuclear magneton,  $g$  is the nuclear  $g$ -factor and  $M_{xx}$ ,  $M_{yy}$  and  $M_{zz}$  are the components of the spin-rotation tensor (in ergs). The spin-rotation tensor  $C$  (in radians/sec) is related to  $M$  by  $M = \hbar C$ . Equation [7-1] can be rearranged to the form

$$C_{\alpha\alpha} = \gamma \hbar^2 [\sigma_{\alpha} - \sigma_{av}^d(\text{free atom})] / [\mu_e I_{\alpha}], \quad \alpha = x, y, z, \quad [7-2]$$

where  $\gamma$  is the nuclear magnetogyric factor and  $\mu_e$  is the Bohr magneton ( $\mu_e = |e|\hbar/[2mc]$ ).

The parallel and perpendicular components of the spin-rotation constant for HMPD,  $C_{\parallel}$  and  $C_{\perp}$ , where  $C_{\parallel} = C_{zz}$  and  $C_{\perp} = C_{xx} = C_{yy}$  can be determined from Equation [7-1]

if the anisotropic components of the chemical shift tensor,  $\sigma_{\parallel}$  and  $\sigma_{\perp}$  are known. The  $^{31}\text{P}$  spectrum of solid HMPA at 77 K shown in Figure 39 was measured by Dr. J. Ripmeester at the National Research Council, Ottawa. The resonance frequency of  $^{31}\text{P}$  was 72.87 MHz and the spectrum was measured with a sweep width of 125 KHz collected in a memory size of 512 points and zero filled to 4096 points before Fourier transformation. The delay between successive scans was 160 sec and four scans were co-added. The spectrum shows the anisotropic line shape resulting from a system with axial or near axial symmetry. The components of the chemical shift tensor  $\sigma_{\parallel}$  and  $\sigma_{\perp}$  were obtained by fitting the spectrum to an anisotropic line shape function with axial symmetry and Gaussian line broadening. The simulation was analogous to that for paramagnetic line shapes of polycrystalline substances reported by Ibers and Swalen (122), who used Lorentzian rather than Gaussian broadening. The chemical shift anisotropy was determined to be  $\sigma_{\parallel} - \sigma_{\perp} = 163.8 \pm 0.1$  ppm. The average chemical shift of  $^{31}\text{P}$  in HMPA with reference to  $\text{PH}_3$  given by Pople et al. (123) and the chemical shift of  $\text{PH}_3$  relative to the free phosphorous atom given by Davis et al. (124):

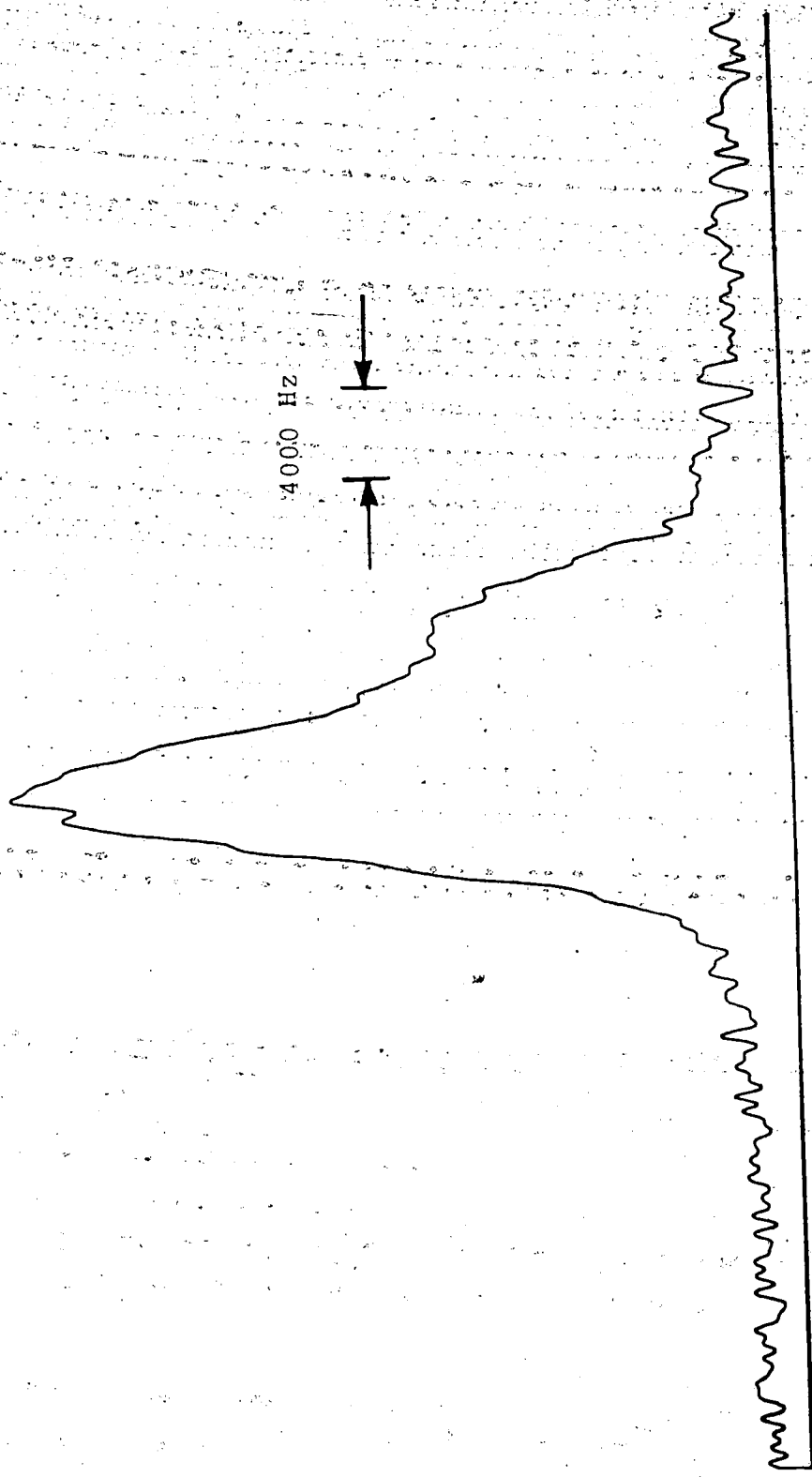


Figure 39. Observed 3p spectrum of solid HMPD. The spectrum was obtained at 77 K. The resonance frequency was 72.87 MHz with a sweep width of 125 kHz collected over 512 data points and zero filled to 4096 points. The delay between experiments was 160 sec. and 4 scans were co-added.



$$\sigma_{av}(\text{HMPA}) - \sigma_{av}(\text{PH}_3) = -261 \pm 1 \text{ ppm}$$

[7-3]

$$\sigma_{av}(\text{PH}_3) - \sigma_{av}^d(\text{free atom}) = -366.4 \pm 0.1 \text{ ppm}$$

give

$$\sigma_{av}(\text{HMPA}) - \sigma_{av}^d(\text{free atom}) = -628 \pm 1 \text{ ppm}$$

[7-4]

Equation [7-4] and the measured chemical shift anisotropy in HMPA given by

$$\sigma_{\parallel}(\text{HMPA}) - \sigma_{\perp}(\text{HMPA}) = 163.8 \pm 0.1 \text{ ppm}$$

were used to obtain the components of the chemical shift tensor relative to free atom value as

$$\sigma_{\parallel}(\text{HMPA}) - \sigma_{av}^d(\text{free atom}) = -518 \pm 1 \text{ ppm}$$

[7-5]

$$\sigma_{\perp}(\text{HMPA}) - \sigma_{av}^d(\text{free atom}) = -682 \pm 1 \text{ ppm}$$

Equation [7-5] and the calculated moments of inertia were substituted in Equation [7-2] to obtain

$$C_{xx,yy} = C_{\perp} = -1.44 \pm 0.01 \text{ KHz}$$

$$C_{zz} = C_{\parallel} = -0.82 \pm 0.01 \text{ KHz}$$

The angular momentum correlation time  $\tau_J$  was determined from the  $^{31}\text{P}$  relaxation rate using Equation [5-11] and the above values  $C_{\perp}$ ,  $C_{\parallel}$ ,  $I_{\perp}$  and  $I_{\parallel}$ . The values of  $\tau_J$ , together with the values calculated from the least squares fit to the form

$$\tau_J = A_1 \exp(-B_1/T), \quad [7-6]$$

are given in Table 2. The non-linear least squares program determined the fitting parameters to be:

$A_1 = 5.8 \pm 0.5 \times 10^{-13}$  sec and  $B_1 = 780 \pm 30$  K. The value of  $\tau_J$  at 300 K is  $4.1 \times 10^{-14}$  sec and it increased to  $1.1 \times 10^{-13}$  sec at 460 K.

### VII.3 $^{14}\text{N}$ $T_1$ Results and Analysis

The variation of  $T_1$  of the  $^{14}\text{N}$  nuclei in HMPA was measured over the temperature range 300 K - 445 K. The  $T_1$  experiments were carried out using the inversion recovery method described in Chapter VI. The experimental results are given in Table 3. The measured  $T_1$  values showed a smooth increase with increasing temperature. The value at 300 K is 0.5 mS and it increases to about 2 mS at the highest temperature. Figure 40 shows the variation of

Table 3

Relaxation Data and Results for  $^{14}\text{N}$  in HMPA

Temp. (K)	$T_1$ obs. (msec)	$\tau_{\text{eff}}^{\text{N}}$ obs. ( $\times 10^{12}$ sec)	$\tau_{\text{eff}}^{\text{N}}$ calc. ( $\times 10^{12}$ sec)
304.8	0.50	5.8	6.0
304.9	0.48	6.1	6.0
317.7	0.59	5.0	5.0
318.2	0.58	5.0	5.0
330.7	0.69	4.3	4.2
331.8	0.73	4.0	4.1
343.4	0.88	3.7	3.6
348.7	0.91	3.3	3.4
355.4	0.97	3.2	3.2
357.7	1.0	3.0	3.1
365.4	1.1	2.8	2.8
378.8	1.2	2.5	2.5
387.0	1.2	2.4	2.3
399.4	1.4	2.0	2.1
412.4	1.5	1.9	1.9
423.4	1.7	1.7	1.7
430.1	1.8	1.6	1.6
439.1	1.9	1.5	1.5
445.2	2.0	1.4	1.5

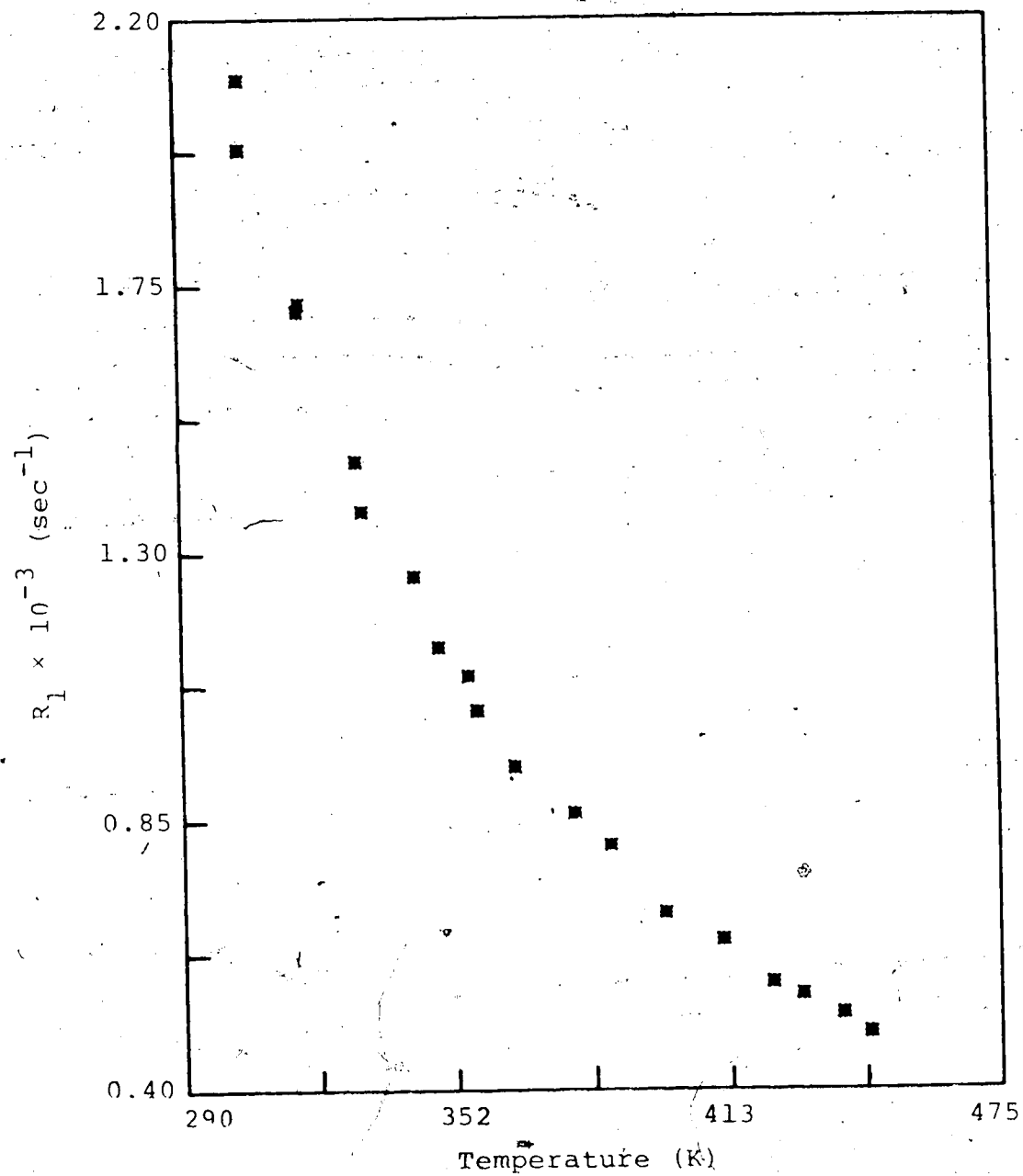


Figure 40. Observed relaxation rates of  $^{14}\text{N}$  in HMPA. The  $T_1$  relaxation times were measured using the inversion-recovery pulse sequence.

the  $^{14}\text{N}$  relaxation rate  $R_1$  with temperature. The smooth decrease of  $R_1$  with temperature indicates that the quadrupolar relaxation mechanism dominates all other processes, as is typical for nuclei with quadrupole moments.

Since the quadrupolar relaxation process entirely dominates other relaxation mechanisms, the  $^{14}\text{N}$   $T_1$  data provide a very convenient means for determination of the reorientational correlation time  $\tau_\theta$ . The temperature dependence of  $R_1$  is due to that of  $\tau_\theta$  (Equation [5-12]).  $\tau_\theta$  can be easily determined from  $R_1$  data if the nuclear quadrupolar coupling constant ( $e^2qQ/\hbar$ ) and the asymmetry parameter ( $\eta$ ) are known. The quadrupole coupling constant and the asymmetry parameter were determined from the  $^{14}\text{N}$  nuclear quadrupole resonance data reported by Krause, and Whitehead (125). They have reported the temperature dependence of  $^{14}\text{N}$  quadrupole resonance frequencies of HMPA over the temperature range from 77 K to 200 K. The quadrupole coupling constant and the asymmetry parameter were calculated at the melting point of HMPA using their relationships with observed nuclear quadrupole resonance frequencies (125). Two sets of  $^{14}\text{N}$  quadrupole resonance frequencies are reported (125). The separation between these frequencies decreases with increasing temperature, but the lines do not coalesce below the melting point. It

was therefore concluded (125) that the frequency separation was due to crystallographically inequivalent nitrogen atoms, there being two inequivalent nitrogen lattice sites per unit cell in HMPA. The separation of resonance lines introduces some uncertainty into the calculations reported here. The average values of quadrupole coupling constant and asymmetry parameter evaluated from two sets of frequency data, were calculated. The average value of the quadrupole coupling constant  $e^2Qq/h$  was calculated to be  $4.8 \pm 0.2$  MHz and the asymmetry parameter  $\eta$  to be  $0.13 \pm 0.01$ .

The calculated values for the quadrupole coupling constant and the asymmetry parameter, along with the experimental  $R_1$  values, were used in Equation [5-12] to obtain the reorientational correlation time  $\tau_\theta^N$ . These values are included in Table 3. The  $\tau_\theta^N$  values for various temperatures were fit into the equation

$$\tau_\theta^N = A_2 \exp(B_2/T) , \quad [7-7]$$

where  $A_2$  and  $B_2$  are fitting parameters. The non-linear least squares analysis yielded:  $A_2 = 6.9 \pm 0.3 \times 10^{-14}$  sec and  $B_2 = 1360 \pm 20$  K.

It is now appropriate to attempt a comparison of the observed variation of  $\tau_\theta^N$  with  $\tau_J$ , with that predicted

using theoretical models for molecular reorientation. The relative magnitudes of the observed  $\tau_{\theta}^N$  (from  $^{14}\text{N}$  data) and  $\tau_J$  (from  $^{31}\text{P}$  data in HMPD) are such that  $\tau_{\theta}^N \gg \tau_J$  and hence these values correspond to rotational motion in the Debye limit (79;90). In this limit, the extended J-diffusion model (77,95-103) and the rotational Fokker-Planck-Langevin (FPL) model (78) give results which are identical to those given by Debye diffusion model (90). The investigated range of  $\tau_{\theta}^N$  and  $\tau_J$ , does not extend into the transition region between the Debye limit and the dilute gas limit. It is in this transition region where a rigorous test of the validity of the extended J-diffusion and FPL models could be made. Hence the  $\tau_{\theta}^N$  and  $\tau_J$  results obtained in this work do not afford an opportunity to test models for rotational motion in liquids.

The experimentally determined variation of  $\tau_{\theta}^N$  and  $\tau_J$  has been compared with the variation predicted by the Hubbard relation (Equation [5-14]). The plots of the correlation times are shown in Figure 41. It is evident from Figure 41 that the observed variation of  $\tau_{\theta}^N$  with  $\tau_J$  does not agree with the theoretical variation. The Hubbard relation predicts substantially larger values for  $\tau_{\theta}$  than those experimentally observed and the deviation of the experimental  $\tau_{\theta}$  values from the theoretical values becomes larger at higher temperatures. These deviations

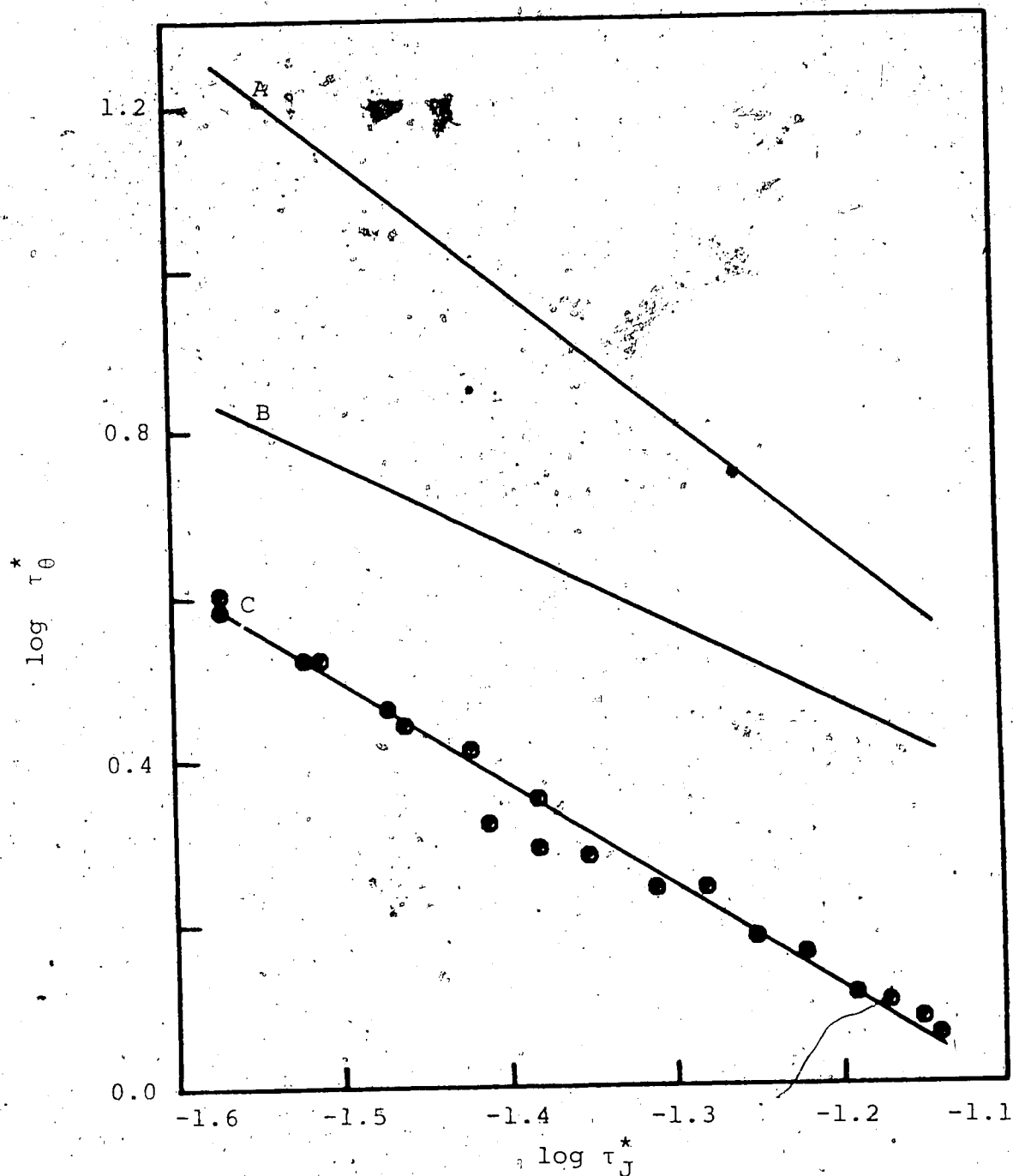


Figure 41. Variation of  $\tau_\theta$  with  $\tau_J$  for HMPD. A, B and C represent  $\log \tau_i^{*PN}$ ,  $\log \tau_\theta^*$  and  $\log \tau_{eff}^{*N}$  respectively. The asterisks denote reduced correlation times, for example,  $\tau_J^* = (kT/I)^{1/2} \tau_J$ . The experimentally observed variation is represented by dots.



are much larger than the uncertainties in  $\tau_{\theta}^N$  and  $\tau_J$  due to experimental errors in the  $T_1$  measurements and the uncertainties in the  $^{14}\text{N}$  quadrupole constant and the  $^{31}\text{P}$  spin rotation tensor. The increasing deviation with increasing temperature (larger  $\tau_J$  values) suggests that the internal rotation process about the P-N bond must be taken into account in the theoretical model. Although the internal rotation about the P-N bond may be expected to possess a relatively large activation energy, it could affect the efficiency of  $^{14}\text{N}$  relaxation in the high temperature range.

The reorientational correlation time  $\tau_{\theta}^N$  deduced from the  $^{14}\text{N}$  data (Equation [7-7], Table 3) is therefore an effective correlation time ( $\tau_{\text{eff}}^N$ ) which is a function of the correlation time for molecular tumbling ( $\tau_{\theta}$ ) and that for internal rotation about the P-N bond ( $\tau_{\text{I}}^{\text{PN}}$ ). The internal motion about the P-N bond is superimposed on the overall molecular tumbling. It is possible to isolate the internal motion about the P-N bond if it is assumed that the molecular reorientation of HMPA is described by the Hubbard relation (Equation [5-14]). The effective correlation time  $\tau_{\text{eff}}^N$  for the case of isotropic reorientation is given by (73,126)

$$\tau_{\text{eff}}^{\text{N}} = A\tau_{\theta} + B\tau_{\theta}\tau_1^{\text{PN}}/(\tau_{\theta} + \tau_1^{\text{PN}}) + C\tau_{\theta}\tau_1^{\text{PN}}/(4\tau_{\theta} + \tau_1^{\text{PN}}) , \quad [7-8]$$

where A, B and C are defined in Equation [5-8]. The angle  $\Delta$  in Equation [5-8] in the case of quadrupolar relaxation corresponds to the angle between the internal rotation axis and the principal field gradient axis. The principal field gradient axis is assumed to lie along the nitrogen atom-lone pair direction and hence  $\Delta$  is expected to be close to the tetrahedral angle. Equation [7-8] assumes that the internal motion and overall molecular tumbling are independent. The temperature dependence of the internal motion correlation time can be described by an equation of form

$$\tau_1^{\text{PN}} = A_3 \exp(B_3/T) , \quad [7-9]$$

where  $A_3$  and  $B_3$  are fitting parameters. The parameters  $A_3$  and  $B_3$  were determined by fitting the observed  $^{14}\text{N}$  correlation times (Table 3) to Equation [7-8], and  $\tau_{\theta}$  was calculated from Hubbard relation (Equation [5-14]) with  $\tau_J$  given by Equation [7-6]. The least squares analysis gave the following results:  $A_3 = 1.2 \pm 0.2 \times 10^{-13}$  sec and

$B_3 = 1710 \pm 80$  K. Equation [7-9] shows the characteristic Arrhenius type variation and hence the energy barrier to internal rotation about the P-N bond can be extracted from it. The parameter  $B_2$  corresponds to  $\Delta E/R$  where  $\Delta E$  is the internal rotation barrier and  $R$  is the gas constant.

Hence the barrier to internal rotation has been calculated to be  $3.4 \pm 0.2$  kcal/mole. No data on activation energies for the hindered rotation about P-N bonds are available in the literature for HMPA in liquid state, but P-N rotation barrier in solid HMPA has been estimated to be 6 kcal/mole by Andreeva et al. (127) from studies of  $^{14}\text{N}$  nuclear quadrupole resonance. The energy barrier in liquid HMPA can be expected to be lower than the value estimated in the solid (127).

#### VII.4 $^2\text{H}$ $T_1$ Results and Analysis

The  $T_1$  relaxation times of  $^2\text{H}$  nuclei in the deuterated analog (HMPD) were studied as a function of temperature. The  $^2\text{H}$   $T_1$  values were measured using the inversion recovery sequence over the temperature range 250-410 K. The relaxation time at 250 K was 0.40 sec and it increased to 3.3 sec at 410 K. The Experimental results are shown in Table 4. Figure 42 shows the variation of the relaxation rate  $R_1$  with temperature.

Table 4

Relaxation Data and Results for  $^2\text{H}$  Nucleus

Temp. (K)	$T_1$ obs. (sec)	$\tau_{\text{eff}}^{\text{D}}$ obs. ( $\times 10^{12}$ sec)	$\tau_{\text{eff}}^{\text{D}}$ calc. ( $\times 10^{12}$ sec)	$\tau_{\text{i}}^{\text{CN}}$ calc. ( $\times 10^{12}$ sec)
253.7	0.40	6.1	5.8	19
264.4	0.53	4.6	4.7	15
274.5	0.64	3.8	3.9	12
283.2	0.74	3.3	3.3	10
290.8	0.87	2.8	2.9	9.0
295.2	0.92	2.7	2.7	8.3
309.4	1.1	2.2	2.2	6.6
316.0	1.2	2.0	2.0	5.9
328.7	1.4	1.7	1.7	4.9
340.2	1.7	1.5	1.5	4.2
349.7	1.9	1.3	1.3	3.7
358.6	2.0	1.2	1.2	3.4
366.8	2.2	1.1	1.1	3.1
376.5	2.4	1.0	0.99	2.8
387.8	2.8	0.88	0.89	2.5
397.8	3.3	0.75	0.81	2.2
408.2	3.3	0.75	0.74	2.0

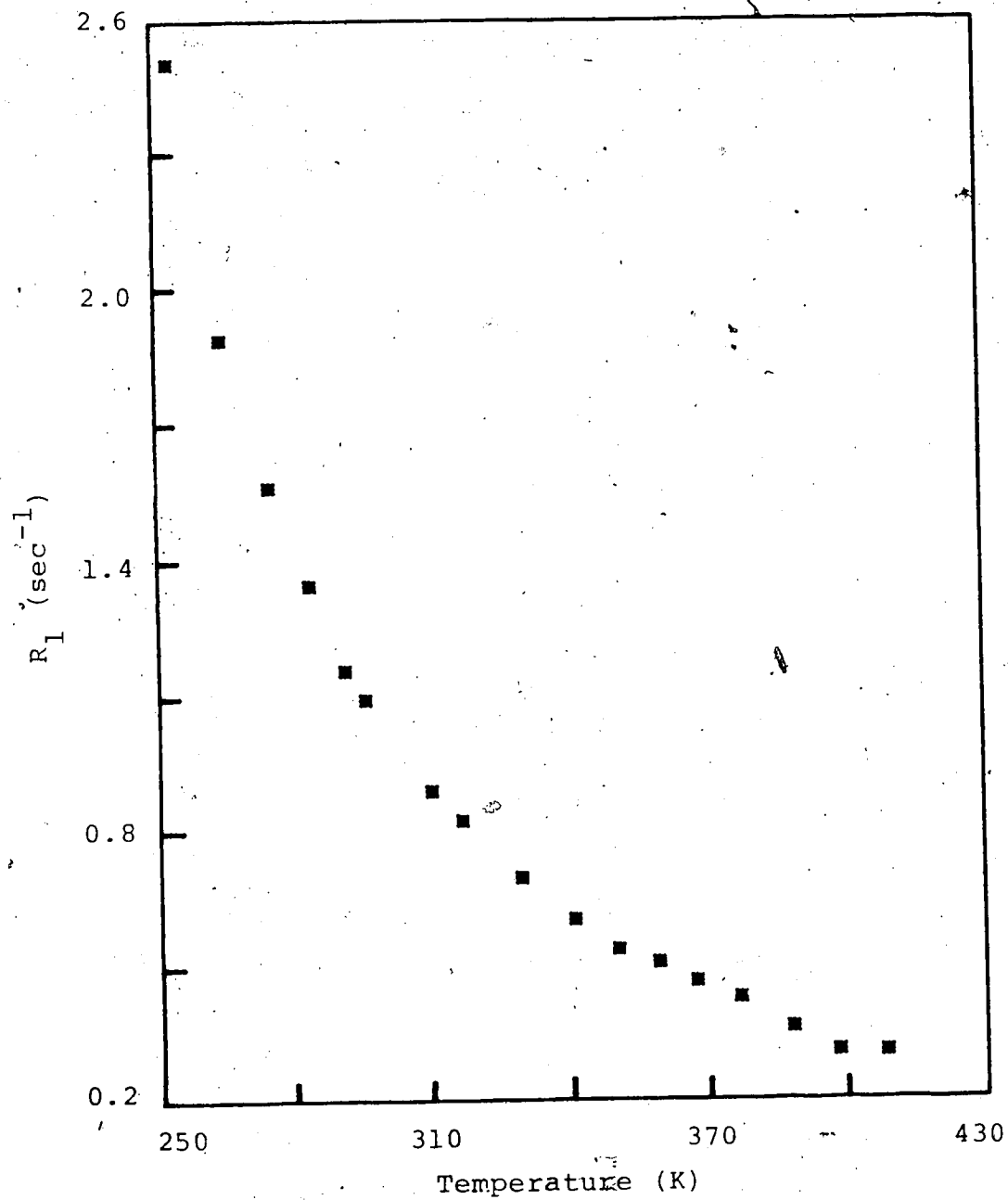


Figure 42. Observed relaxation rates of  $^2\text{H}$  in HMPD. The  $T_1$  relaxation times were measured with the inversion-recovery pulse sequence.

The  $^2\text{H}$  relaxation in HMPD can be assumed to be entirely due to motional modulation of quadrupolar interactions. The quadrupolar relaxation rate of deuterium in the  $\text{CD}_3$  group in HMPD is governed by three correlation times: (1) that due to molecular tumbling ( $\tau_0$ ), (2) that due to internal rotation about P-N bond ( $\tau_1^{\text{PN}}$ ), and (3) that due to internal rotation about the C-N bond ( $\tau_1^{\text{CN}}$ ). The internal rotation about the P-N bond is superimposed on the molecular tumbling motion to yield the effective correlation time  $\tau_{\text{eff}}^{\text{N}}$  discussed in Section VII.3. The internal motion of the  $\text{CD}_3$  group is superimposed on  $\tau_{\text{eff}}^{\text{N}}$  to give a third correlation time  $\tau_{\text{eff}}^{\text{D}}$  which governs the time dependence of the  $^2\text{H}$  quadrupolar interaction. Since all three motions are independent of each other,  $\tau_{\text{eff}}^{\text{D}}$  can be written as

$$\tau_{\text{eff}}^{\text{D}} = A' \tau_{\text{eff}}^{\text{N}} + B' \tau_{\text{eff}}^{\text{N}} \tau_1^{\text{CN}} / (\tau_{\text{eff}}^{\text{N}} + \tau_1^{\text{CN}}) + C' \tau_{\text{eff}}^{\text{N}} \tau_1^{\text{CN}} / (4 \tau_{\text{eff}}^{\text{N}} + \tau_1^{\text{CN}}), \quad [7-10]$$

where  $\tau_{\text{eff}}^{\text{N}}$  is given by Equation [7-8] and  $A'$ ,  $B'$  and  $C'$  are analogous to  $A$ ,  $B$  and  $C$  respectively, in Equation [5-8]. In the definitions of  $A'$ ,  $B'$  and  $C'$ , the angle variable is denoted by  $\Delta'$  and is the angle between the internal rotation axis (the C-N bond) and principal axis

of the deuterium field gradient tensor (the C-D bond). Hence  $\Delta'$  is the tetrahedral angle  $109^\circ 28'$ . The relaxation of the  $^2\text{H}$  nuclei in HMPD thus provides an interesting case where the relaxation interaction is modulated by a time dependence characterized by three correlation times.

The quadrupolar relaxation rate in the presence of internal motion is obtained from Equation [5-12] by replacing  $\tau_\theta$  by  $\tau_{\text{eff}}^{\text{D}}$ . The deuterium quadrupole coupling in HMPD has not been reported, so we have assumed that the observed value,  $166 \pm 10$  KHz (128), for the  $\text{CD}_3$  deuterium quadrupole coupling constant in methylamine would provide an accurate estimate for the HMPD molecule. The value of  $e^2Qq/h$  for D in  $\text{CD}_3$  group varies from  $180 \pm 5$  KHz in  $\text{CD}_3\text{I}$  (129) to  $133 \pm 7$  KHz in  $\text{CD}_3\text{F}$  (130) and the variation is related to the electronegativity of the group attached to the  $\text{CD}_3$  group (131). Hence  $\text{CD}_3\text{NH}_2$  seemed the logical molecule to use in estimating  $e^2Qq/h$  for D in HMPD. The asymmetry parameter  $\eta$  for deuterium in  $\text{CD}_3$  group is very close to zero due to the cylindrical symmetry of the electric field gradient and can be dropped to a good approximation (132). Hence the relaxation rate expression (Equation [5-12]) reduces to

$$R_1 = \frac{3}{8} \left( \frac{e^2qQ^2}{h} \right)^2 \tau_{\text{eff}}^{\text{D}} \quad [7-11]$$

The deuterium  $T_1$  data (Table 4) were analyzed to yield the effective correlation time  $\tau_{\text{eff}}^{\text{D}}$  which is also given in Table 4.

The effective correlation time  $\tau_{\text{eff}}^{\text{N}}$  appearing in Equation [7-10] was determined from the  $^{14}\text{N}$  data in Section VII.3. The temperature dependence of the internal rotation correlation time was assumed to have the form

$$\tau_i^{\text{CN}} = A_4 \exp(B_4/T) , \quad [7-12]$$

where  $A_4$  and  $B_4$  are fitting parameters. The observed deuterium correlation times ( $\tau_{\text{eff}}^{\text{D}}$ ) (Equation [7-11]) were fit to Equation [7-10] using Equations [7-8], [7-9], [7-12] and the Hubbard model. Fixing  $A_3$  and  $B_3$  at the values obtained from least squares analysis (Section VII.3), the best fit values for  $A_4$  and  $B_4$  were determined. The non-linear least squares analysis gave the following results:  $A_4 = 5.1 \pm 0.7 \times 10^{-14}$  sec and  $B_4 = 1500 \pm 40$  K. The barrier to the rotation of the  $\text{CD}_3$  group in HMPD was determined from the parameter  $B_4$  to be  $3.0 \pm 0.1$  kcal/mole. This compares favourably with the set of methyl rotation barrier values for various organic molecules compiled by Lambert et al. (81), for example, 2.9 kcal/mole in 1,1,1-trichloroethane [ $\text{CH}_3\text{CCl}_3$ ] and 3.5



kcal/mole in tertiarybutylchloride  $[(CH_3)_3CCl]$  (133,134). Andreeva et al. (127) have reported the  $CH_3$  rotational barrier in solid HMPA to be 2 kcal/mole, but have stressed that their work gives a lower bound.

#### VII.5 $^{31}P$ $T_1$ (HMPA) Results and Analysis

The longitudinal relaxation times of  $^{31}P$  in HMPA were measured over the temperature range 299 K to 460 K.  $T_1$  measurements were carried out using the inversion recovery sequence described in Chapter VI. The experimental results are shown in Figure 43 and Table 5. The  $T_1$  value at 296 K was 18 sec which increased to a maximum of 20 sec at 311 K and then decreased steadily to 10 sec at 461 K. The occurrence of a maximum in the temperature variation of  $T_1$  indicates the presence of two competing relaxation mechanisms: the spin rotation and dipolar contributions, which have complimentary temperature dependence. The total relaxation rate can be written as

$$R_1 = R_{1SR} + R_{1intraDD} + R_{1interDD} \quad [7-13]$$

where  $R_{1SR}$ ,  $R_{1intraDD}$  and  $R_{1interDD}$  are given by Equations [5-11], [5-8] and [5-9] respectively. The spin rotation relaxation rate increases with increasing temperature

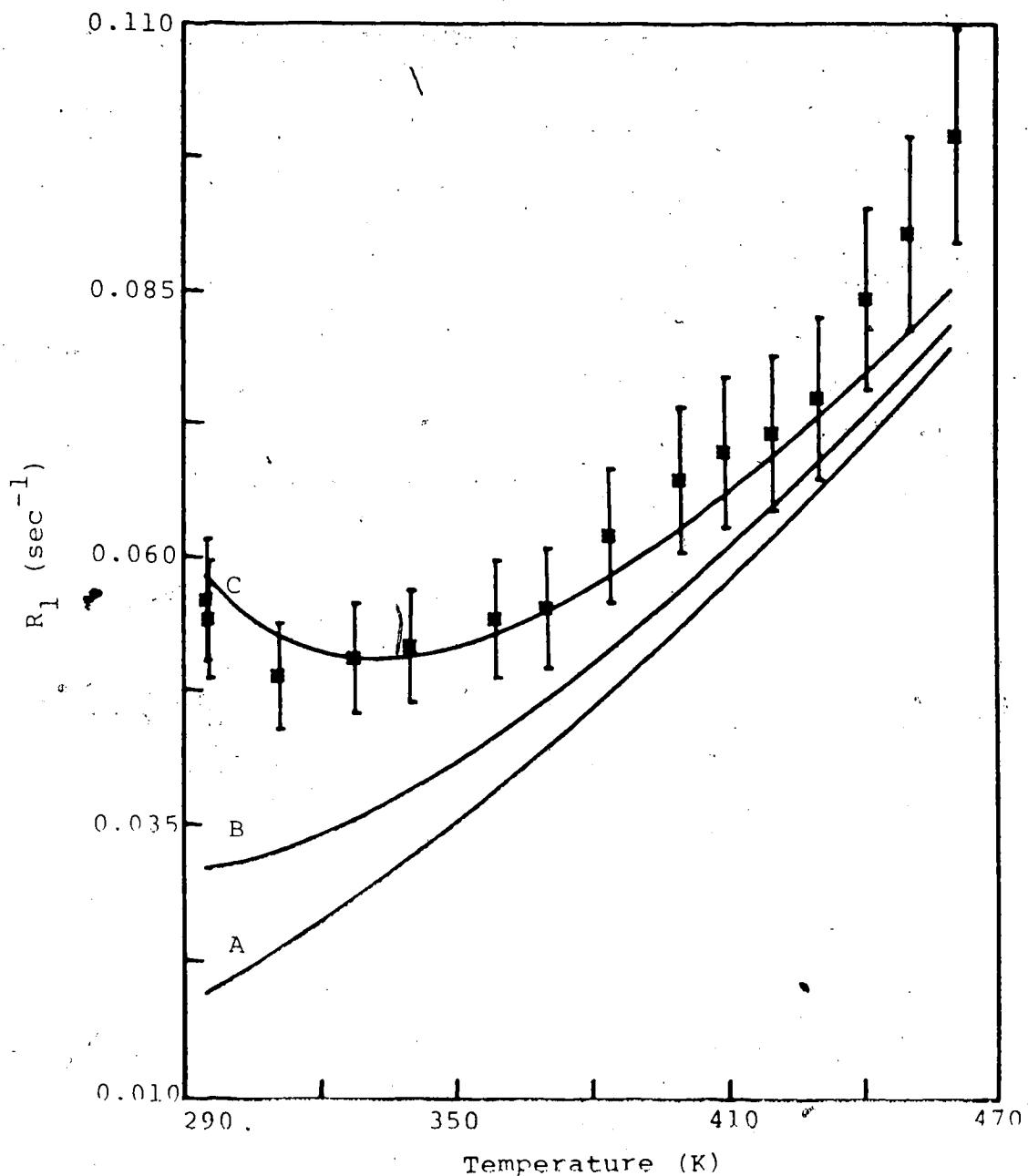


Figure 43. Comparison of calculated and observed  $^{31}\text{P}$  relaxation rates in HMPA. The asterisk points show the observed  $T_1$  relaxation rates with  $\pm 10\%$  error bounds. The solid lines denote the calculated relaxation rates: curve A represents the spin-rotation relaxation rate; curve B represents the sum of spin-rotation and intramolecular dipolar relaxation rates; and curve C represents the sum of spin rotation, intramolecular and intermolecular dipolar relaxation rates.

Table 5  
Relaxation Data for  $^{31}\text{P}$  in HMPA

Temp. (K)	$T_1$ (sec)
295.0	18
295.6	18
311.0	20
327.8	20
340.2	19
359.2	18
370.5	18
384.5	16
400.2	15
409.9	14
420.4	14
430.4	13
441.2	12
450.5	11
460.9	10 <sup>s</sup>

while the intramolecular and intermolecular dipolar relaxation rates decrease with increasing temperature, but at different rates. An attempt was made to delineate the contributions due to spin-rotation, inter- and intramolecular dipolar interactions over the temperature range studied. To attain this objective, the individual relaxation rates were computed using parameters determined from the analysis of  $^{14}\text{N}$ ,  $^2\text{H}$  and  $^{31}\text{P}$  in HMPD data in previous sections. The correlation times  $\tau_{\text{eff}}^{\text{N}}$  and  $\tau_{\text{i}}^{\text{CN}}$  obtained from the  $^{14}\text{N}$  and  $^2\text{H}$  data were used to compute the  $R_{\text{lintra}}$  term. The angular momentum correlation time  $\tau_{\text{J}}$  determined from  $^{31}\text{P}$  in HMPD was used to calculate  $R_{\text{ISR}}$ . The translational diffusion coefficients which were measured over the entire temperature range were used in the calculation of  $R_{\text{linter}}$ .

#### a. Calculation of Spin-Rotation Relaxation Rates

Equation [5-11] was employed to calculate the spin-rotational contribution to the total relaxation rate. The moments of inertia were calculated as described in Section VII.4 using crystallographic data (120). The following moments of inertia were obtained:  $I_{\parallel} = 1.08 \pm 0.02 \times 10^{-37}$  g cm<sup>2</sup> and  $I_{\perp} = 0.81 \pm 0.01 \times 10^{-37}$  g cm<sup>2</sup>. The components of the spin-rotation tensor were evaluated using Equation [7-2], with the results:  $C_{\parallel} = -0.99 \pm 0.02$  KHz and

$C_1 = -1.74 \pm 0.02$  KHz. The angular momentum correlation time  $\tau_J$  in HMPA was assumed to be equal to that in HMPD. This should prove to be a reasonable assumption since their moments of inertia are quite similar. The contribution  $R_{1SR}$  to the total relaxation rate was then calculated using Equation [5-11]. The results are given in Table 6.

b. Calculation of Intermolecular Dipolar Relaxation Rates

The translational diffusion coefficient  $D_t$  of HMPA was measured using the stationary field gradient technique described in Chapter VI. The experimental results are given in Table 7. The diffusion coefficient at 304 K is  $3.8 \times 10^{-6} \text{ cm}^2\text{sec}^{-1}$  and it increases to  $2.3 \times 10^{-5} \text{ cm}^2\text{sec}^{-1}$  at 450 K. The experimental data were fit to the equation

$$D_t = A_5 \exp(B_5/T) \quad [7-14]$$

where the fitting parameters  $A_5$  and  $B_5$  were determined to be:  $A_5 = 1.2 \pm 0.2 \times 10^{-3} \text{ cm}^2\text{sec}^{-1}$  and  $B_5 = -1740 \pm 50$  K. Equation [5-9] was used to compute  $R_{1interDD}$ . The factor  $a$  in Equation [5-9] represents the hydrodynamic radius of HMPA, i.e. the effective radius of the HMPA molecule if the molecule is assumed to be spherical in shape and to be

Table 6

Comparison of Calculated and Observed  $^1\text{H}$  Relaxation Rates in HMPA

Temp. (K)	$R_{1\text{SR}}^{\text{calc.}}$ ( $\text{sec}^{-1}$ )	$R_{1\text{DDIntra}}^{\text{calc.}}$ ( $\text{sec}^{-1}$ )	$R_{1\text{DDInter}}^{\text{calc.}}$ ( $\text{sec}^{-1}$ )	$R_{1\text{Total}}^{\text{calc.}}$ ( $\text{sec}^{-1}$ )	$R_1^{\text{obs.}}$ ( $\text{sec}^{-1}$ )
295.0	0.020	0.012	0.027	0.058	0.056
295.5	0.020	0.012	0.027	0.058	0.054
310.9	0.024	0.0091	0.020	0.053	0.049
327.8	0.029	0.0073	0.015	0.051	0.051
340.1	0.032	0.0062	0.012	0.051	0.052
359.1	0.039	0.0050	0.0095	0.053	0.054
370.4	0.042	0.0045	0.0082	0.055	0.056
384.4	0.048	0.0039	0.0069	0.058	0.062
400.1	0.054	0.0034	0.0058	0.063	0.068
409.9	0.058	0.0031	0.0052	0.066	0.070
420.4	0.062	0.0029	0.0047	0.070	0.072
430.4	0.066	0.0027	0.0042	0.073	0.075
441.1	0.071	0.0025	0.0038	0.077	0.084
450.4	0.075	0.0023	0.0035	0.081	0.090
460.9	0.080	0.0022	0.0032	0.086	0.100

Table 7

## Translational Diffusion Coefficients of HMPA

Temp (K)	D obs. ( $\times 10^6$ cm <sup>2</sup> sec <sup>-1</sup> )	D l.s.fit ( $\times 10^6$ cm <sup>2</sup> sec <sup>-1</sup> )
304.2	3.9	4.0
309.4	4.4	4.4
318.6	5.1	5.2
329.0	6.2	6.2
341.4	7.6	7.5
351.0	7.6	8.6
355.0	8.9	9.1
357.2	10	9.3
361.2	11	9.9
369.9	13	11
381.4	12	13
391.2	14	14
402.0	16	16
410.2	18	18
421.0	22	20
430.4	21	21
440.0	23	23
449.6	23	26

immersed in a continuous viscous medium. The hydrodynamic radius was taken to be  $4 \times 10^{-8}$  cm. The calculated  $R_{1interDD}$  values are given in Table 6.

c. Calculation of the Intramolecular Dipole Relaxation Rates

The intramolecular dipolar relaxation rates were calculated taking into account the effects of internal motion of methyl groups superimposed on the overall molecular reorientation. It has been shown (135) that when internal rotation modulates the internuclear separation, the intramolecular dipolar relaxation rates can be affected in certain molecular geometries. Hence in such cases, Equation [5-8] which does not take into account the modulation of internuclear distance, does not adequately determine the relaxation rate. In the work (135) mentioned above, the internuclear distance term appearing in the correlation functions, was expressed as a function of the internal rotation angle and the correlation functions were evaluated (135) assuming that a rotational diffusion model describes both internal and overall molecular rotation. The spectral density functions resulting from these correlation functions were substituted in Equation [5-5] to give the relaxation rate expression [Equation [11] of Reference (135)] for dipolar



relaxation with modulation of the internuclear distance by internal rotation.

In HMPA, the  $^{31}\text{P}$ - $^1\text{H}$  internuclear separation is modulated by rotation of the methyl groups. Hence the approach described above was employed for the calculation of  $R_{\text{intraDD}}$ . The effective reorientational correlation time  $\tau_{\text{eff}}^{\text{N}}$  determined from the  $^{14}\text{N}$  data in Section VII.3 and the internal rotation correlation time  $\tau_{\text{I}}^{\text{CN}}$  obtained from the analysis of the  $^2\text{H}$  data in Section VII.4, were substituted in Equation [11] of Reference (135) to evaluate the  $R_{\text{intraDD}}$  term. The results are given in Table 6.

d. Comparison of Calculated and Experimental Relaxation Rates

The calculated values for spin-rotation, inter- and intramolecular dipolar relaxation rates along with the experimental relaxation rates of  $^{31}\text{P}$  in HMPA are given in Table 6. Graphical illustration of the data in Table 6 is shown in Figure 43. At 311 K, the spin-rotation mechanism contributes approximately 48% of the total relaxation rate while the inter- and intramolecular dipolar rates are approximately 41% and 19% respectively. Although the calculated relaxation rate is only grossly consistent with the experimental value at 311 K, it exhibits a reassuring

feature: the contribution of dipolar relaxation mechanisms and spin-rotation mechanisms are approximately equal at the minimum in the plot of relaxation rate with temperature (136). The calculations (Table 6) show that the spin-rotation contribution is 48% at 311 K which is approximately the temperature at which the experimental plot shows a minimum (Figure 43). The spin-rotation contribution increases to about 80% at 400 K while the inter- and intramolecular dipolar contributions decrease to about 9% and 5% respectively. At 461 K the spin-rotation interaction contributes approximately 81% of the total relaxation rate and the dipolar mechanisms account for about 6% of the total rate. Although the calculated relaxation rates do not agree with experimental rates in a rigorous quantitative manner, the delineation of the contributions of various relaxation mechanisms remains valid considering the limits of experimental errors and the various approximations used.

Another interesting feature which emerges from Table 6 is that the intermolecular dipolar relaxation rates are larger than the intramolecular dipolar rates. Although this result seems surprising, it can be rationalized when the implications of the internal rotation of methyl groups are recognized. It has been shown (137) that the effect of internal motion is most pronounced when the internal

rotation correlation time  $\tau_i^{\text{CN}}$  and the overall reorientational correlation time  $\tau_\theta$  are comparable. In HMPA,  $\tau_i^{\text{CN}}$  and  $\tau_\theta$  correlation times are comparable (Equations [7-7] and [7-12]) and hence the internal motion can be expected to alter the intramolecular dipolar contribution when compared with situations where internal motion is absent or when  $\tau_i^{\text{CN}}$  is different from  $\tau_\theta$  by several orders of magnitude.

#### VII.6 Conclusions

The work described in Chapters V, VI and VII of this thesis demonstrates the use of relaxation data for the various nuclei to obtain an overall picture of the molecular motion in HMPA.

The study of  $^{31}\text{P}$  relaxation in the deuterated compound (HMPD) has yielded the angular momentum correlation times  $\tau_J$ . The study of the deuterated form of the molecule has been useful in isolating the spin-rotation interaction of the  $^{31}\text{P}$  nucleus.

From the  $^{14}\text{N}$  data analysis, it has been found that the effective correlation time for reorientation is a function of the molecular tumbling correlation time and that for internal motion about the P-N bond. It was found that the inclusion of the internal motion about the P-N

bond was essential for agreement between the experimental variation of  $\tau_{\theta}^N$  with  $\tau_J$ , and the corresponding variation predicted by the Hubbard relation. The internal rotation about the P-N bond was found to be quite hindered, with an activation energy of  $3.4 \pm 0.2$  kcal/mole. The internal rotation correlation time  $\tau_i^{PN}$  was about 5 times larger than the correlation time for molecular tumbling  $\tau_{\theta}$  (given by the Hubbard relation) at room temperature. At 450 K this ratio decreased to about 1.4. Thus at high temperatures the internal motion time scale was comparable to that for molecular tumbling and hence altered the effective reorientation correlation time  $\tau_{eff}^N$  significantly.

The relative magnitude of  $\tau_{\theta}$  and  $\tau_J$  was such that  $\tau_{\theta} \gg \tau_J$ , which is the Debye limiting situation. In the Debye limit, the results from various models for molecular reorientation, such as the J-diffusion model (77,95-103) and the Fokker-Planck-Langevin model (78), essentially reduce to those given by the Hubbard relation. The applicability of models for molecular reorientation can only be tested using the results at the transition stage between the Debye limit and the dilute gas limit. Hence it was not possible to test the validity of the J-diffusion or FPL models from the results on HMPA obtained in this work.

The relaxation study of  $^2\text{H}$  in HMPD provided an interesting situation where the effective correlation time was affected by three types of motion: (1) overall molecular tumbling, (2) internal motion about the N-P bond and (3) internal motion of the  $\text{CD}_3$  groups. It was found that the rotation of  $\text{CD}_3$  groups was also relatively hindered with an activation energy of  $3.0 \pm 0.1$  kcal/mol. This result seems to be in the correct range when compared with the results in the literature for activation energies for rotation of methyl groups. A comparison of the relative magnitudes of the correlation times, give the ratio of  $\tau_1^{\text{PN}}:\tau_0:\tau_1^{\text{CN}}$  to be 40:15:1 at room temperature. At 450 K this ratio becomes approximately 30:20:1. The relative ratio of each internal correlation time to  $\tau_0$  is such that the effect of each internal motion process on the overall motion is appreciable.

It has been possible to delineate the individual contributions to  $^{31}\text{P}$  relaxation in HMPA at various temperatures. The separation of the contributions was carried out by calculating the relaxation rates due to various mechanisms, using results derived from the analysis of  $^{31}\text{P}$  in HMPD,  $^{14}\text{N}$  and  $^2\text{H}$  data. It was found that at about 311 K the spin-rotation and the total dipolar contributions were approximately equal at higher temperatures, the spin-rotation contribution became much

more dominant and accounted for most of the relaxation rate at 460 K. Another interesting observation was that the contribution of intermolecular dipolar interactions was larger than the intramolecular dipolar component. This can be rationalized on the basis that the internal motion of methyl groups, with correlation time comparable to that for molecular tumbling, reduces the effective spectral density and hence makes the intramolecular dipolar relaxation rate smaller than one would find in the absence of internal rotation.

#### VII.7 Summary

The results of the relaxation rate studies in HMPA and the data analysis were presented in this chapter. The use of  $^{31}\text{P}$   $T_1$  values in HMPD to obtain angular momentum correlation time was described. The analysis of  $^{14}\text{N}$  data to yield the correlation times for reorientation and internal motion about the N-P bond was presented. It was followed by  $^2\text{H}$  data analysis yielding the correlation time for internal rotation of methyl groups. The delineation of contributions to the relaxation rate of  $^{31}\text{P}$  in HMPA was discussed. Finally, the conclusions derived from this study were presented.

## REFERENCES

1. C.P. Slichter, "Principles of Magnetic Resonance", 2nd Ed., Springer-Verlag, Berlin, 1978.
2. R.M. Lynden-Bell, Prog. NMR Spectrosc., 2, Chapter 4, 163 (1967).
3. T.C. Farrar and E.D. Becker, "Pulse and Fourier Transform NMR", Academic Press, New York, 1971.
4. A. Carrington and A.D. McLachlan, "Introduction to Magnetic Resonance", John Wiley and Sons, Inc., New York, 1967.
5. A.G. Redfield, IBM J. Res. Develop., 1, 19 (1957).
6. C.S. Johnson, Adv. Magn. Reson., 1, 33 (1965).
7. G. Bodenhausen, Prog. NMR Spectrosc., 14, 137 (1981).
8. J. Jeener, Ampere International Summer School, Basko Polje, Yugoslavia (1971), unpublished.
9. R. Freeman and G.A. Morris, Bull. Magn. Reson., 1, 5 (1979).
10. A. Bax, "Two Dimensional Nuclear Magnetic Resonance In Liquids", D. Reidel Publishing Company, Holland, 1982.
11. G. Bodenhausen, R. Freeman, R. Niedermeyer and D.L. Turner, J. Magn. Reson., 26, 133 (1977).

12. W.P. Aue, E. Bartholdi and R.R. Ernst, J. Chem. Phys., 64, 2229 (1976).
13. L. Muller, A. Kumar and R.R. Ernst, J. Chem. Phys., 63, 5490 (1975).
14. W.P. Aue, J. Karhan and R.R. Ernst, J. Chem. Phys., 64, 4226 (1976).
15. G. Bodenhausen, R. Freeman and D.L. Turner, J. Chem. Phys., 65, 839 (1976).
16. A.A. Maudsley and R.R. Ernst, Chem. Phys. Lett., 50, 368 (1977).
17. A.A. Maudsley, L. Muller and R.R. Ernst, J. Magn. Reson., 28, 463 (1977).
18. G. Bodenhausen and R. Freeman, J. Magn. Reson., 28, 471 (1977).
19. A. Bax and G.A. Morris, J. Magn. Reson., 42, 501 (1981).
20. K. Nagayama, K. Wuthrich and R.R. Ernst, Biochem. Biophys. Res. Commun., 90, 305 (1979).
21. A. Bax, R. Freeman and G.A. Morris, J. Magn. Reson., 42, 164 (1981).
22. K. Nagayama, A. Kumar, K. Wuthrich and R.R. Ernst, J. Magn. Reson., 40, 321 (1980).
23. G. Wagner, A. Kumar and K. Wuthrich, Eur. J. Biochem., 114, 375 (1981).



24. S. Macura and R.R. Ernst, *J. Magn. Reson.*, 43, 259 (1981).
25. A. Kumar, G. Wagner, R.R. Ernst and K. Wuthrich, *J. Am. Chem. Soc.*, 103, 3654 (1979).
26. B.H. Meier and R.R. Ernst, *J. Am. Chem. Soc.*, 101, 6441 (1979).
27. J. Jeener, B.H. Meier, P. Bachmann and R.R. Ernst, *J. Chem. Phys.*, 71, 4546 (1979).
28. U. Piantini, O.W. Sorenson and R.R. Ernst, *J. Am. Chem. Soc.*, 104, 6800 (1982).
29. A.J. Shaka and R. Freeman, *J. Magn. Reson.*, 51, 169 (1981).
30. M.H. Levitt and R.R. Ernst, *Chem. Phys. Lett.*, 100, 119 (1983).
31. D.M. Doddrell, D.T. Pegg and M.R. Bendall, *J. Magn. Reson.*, 48, 323 (1982).
32. P. Meakin and J.P. Jesson, *J. Magn. Reson.*, 10, 290 (1973).
33. P. Meakin and J.P. Jesson, *J. Magn. Reson.*, 11, 182 (1973).
34. P. Meakin and J.P. Jesson, *J. Magn. Reson.*, 13, 354 (1974).
35. P. Meakin and J.P. Jesson, *J. Magn. Reson.*, 18, 411 (1975).
36. A.D. Bain, *J. Magn. Reson.*, 39, 335 (1980).

37. A.D. Bain, J. Bognais and S. Brownstein, *Can. J. Chem.*, 59, 723 (1981).
38. A.D. Bain, private communication.
39. O.W. Sorenson and R.R. Ernst, *J. Magn. Reson.*, 51, 477 (1983).
40. O.W. Sorenson, G.W. Eich, M.H. Levitt, G. Bodenhausen and R.R. Ernst, *Prog. NMR Spectrosc.*, 16, 163 (1983).
41. K.J. Packer and K.M. Wright, *Mol. Phys.*, 50, 797 (1983).
42. A.C. Hearn, "REDUCE2 Implementation Guide for the General Computer", University of Utah Symbolic Computation Group Technical Report No. TR-7, June 1978.
43. P.L. Corio, "Structure of High-Resolution NMR Spectra", Academic Press, New York, 1966.
44. A. Bax, *J. Magn. Reson.*, 52, 76 (1983).
45. D.M. Doddrell, J. Staunton and E.D. Laue, *J. Magn. Reson.*, 52, 523 (1983).
46. R. Freeman, S.P. Kempell and M.H. Levitt, *J. Magn. Reson.*, 38, 453 (1980).
47. R.R. Ernst, *J. Chem. Phys.*, 45, 3845 (1966).
48. J.B. Grutzner and R.E. Santini, *J. Magn. Reson.*, 19, 173 (1975).

49. W.A. Anderson and F.A. Nelson, *J. Chem. Phys.*, 39, 183 (1963).
50. V.J. Basus, P.D. Ellis, H.D.W. Hill and J.S. Waugh, *J. Magn. Reson.*, 35, 19 (1979).
51. M.H. Levitt, T.A. Frenkiel and R. Freeman, *J. Magn. Reson.*, 47, 328 (1982).
52. D.T. Pegg, M.R. Bendall and D.M. Doddrell, *J. Magn. Reson.*, 49, 32 (1982).
53. M.H. Levitt, G. Bodenhausen and R.R. Ernst, *J. Magn. Reson.*, 53, 443 (1983).
54. M.H. Levitt, O.W. Sorenson and R.R. Ernst, *Chem. Phys. Lett.*, 94, 540 (1983).
55. M.R. Bendall and D.T. Pegg, *J. Magn. Reson.*, 53, 144 (1983).
56. D.T. Pegg and M.R. Bendall, *J. Magn. Reson.*, 55, 114 (1983).
57. T.T. Nakashima, B.K. John and R.E.D. McClung, *J. Magn. Reson.*, 57, 149 (1984).
58. A. Bax, R. Freeman and T.A. Frenkiel, *J. Am. Chem. Soc.*, 103, 2102 (1981).
59. A. Bax, R. Freeman and S.P. Kempell, *J. Am. Chem. Soc.*, 102, 4849 (1980).
60. D.P. Burum and R.R. Ernst, *J. Magn. Reson.*, 39, 163 (1980).
61. G.A. Morris, *J. Magn. Reson.*, 41, 185 (1980).

62. O.W. Sorenson, R. Freeman, T.A. Frenkiel, T.H. Mareci and R. Schuck, *J. Magn. Reson.*, 46, 180 (1982).
63. A. Bax, R. Freeman, T.A. Frenkiel and M.H. Levitt, *J. Magn. Reson.*, 43, 478 (1981).
64. A. Bax, S.P. Kempell and R. Freeman, *J. Magn. Reson.*, 41, 349 (1980).
65. K.J. Packer, *Prog. NMR Spectrosc.*, 3, 87 (1967).
66. A. Abragam, "The Principles of Nuclear Magnetism", Oxford Clarendon Press, 1961.
67. F. Bloch, *Phys. Rev.*, 70, 460 (1946).
68. J.R. Lyerla, Jr. and G.C. Levy, *Topics in Carbon-13 NMR Spectroscopy*, 1, 79 (1974).
69. H.W. Spiess, *NMR Basic Principles and Progress*, 15, 55 (1978).
70. H.G. Hertz, *Prog. NMR Spectrosc.*, 3, 159 (1967).
71. T.C. Farrar, A.A. Maryott and M.S. Malmberg, *Ann. Rev. Phys. Chem.*, 23, 193 (1972).
72. D.E. Woessner, *J. Chem. Phys.*, 37, 647 (1962).
73. D.E. Woessner, B.S. Snowden, Jr. and G.H. Meyer, *J. Chem. Phys.*, 50, 719 (1969).
74. H.W. Spiess, D. Schweitzer, U. Haeberlen and K.H. Hausser, *J. Magn. Reson.*, 5, 101 (1971).
75. A.A. Maryott, T.C. Farrar and M.S. Malmberg, *J. Chem. Phys.*, 54, 64 (1971).

76. J. DeZwaan, R.J. Finney and J. Jonas, *J. Chem. Phys.*, 60, 3223 (1974).
77. R.G. Gordon, *J. Chem. Phys.*, 44, 1830 (1966).
78. M. Fixman and K. Rider, *J. Chem. Phys.*, 51, 2425 (1969).
79. R.E.D. McClung, *J. Chem. Phys.*, 51, 3842 (1969).
80. R.E.D. McClung and H. Versmold, *J. Chem. Phys.*, 57, 2596 (1972).
81. J.B. Lambert, R.J. Nienhuis and J.W. Keepers, *Angew. Chemie*, 20, 487 (1981).
82. J.G. Powles, in "Magnetic Resonance and Relaxation", R. Blinc, Ed., North Holland Publishing Company, Amsterdam, 1967.
83. H.C. Torrey, *Phys. Rev.*, 92, 962 (1953).
84. P.S. Hubbard, *Phys. Rev.*, 131, 275 (1963).
85. I. Oppenheim and M. Bloom, *Can. J. Phys.*, 39, 845 (1961).
86. P.S. Hubbard, *Phys. Rev.*, 131, 1155 (1963).
87. D.K. Green and J.G. Powles, *Proc. Phys. Soc.*, 85, 87 (1965).
88. C.H. Wang, *J. Magn. Reson.*, 9, 75 (1973).
89. W.H. Flygare, *J. Chem. Phys.*, 41, 793 (1964).
90. P. Debye, "Polar Molecules", Dover Publications, Inc., New York, 1945.

91. N. Bloembergen, E.M. Purcell and R.V. Pound, *Phys. Rev.*, 73, 679 (1948).
92. W.A. Steele, *J. Chem. Phys.*, 36, 2404, 2411 (1963).
93. H. Shimizu, *J. Chem. Phys.*, 43, 2453 (1965).
94. H. Shimizu, *Bull. Chem. Soc. Japan*, 39, 2385 (1966).
95. R.E.D. McClung, *J. Chem. Phys.*, 54, 3248 (1971).
96. R.E.D. McClung, *J. Chem. Phys.*, 55, 3459 (1971).
97. R.D. Mountain, *J. Chem. Phys.*, 51, 3243 (1971).
98. R.E.D. McClung, *J. Chem. Phys.*, 57, 5478 (1972).
99. A.G. St. Pierre and W.A. Steele, *J. Chem. Phys.*, 57, 4638 (1972).
100. F. Bliot, C. Abbar and E. Constant, *Mol. Phys.*, 24, 241 (1972).
101. F. Bliot and E. Constant, *Chem. Phys. Lett.*, 18, 253 (1973).
102. T.E. Eagles and R.E.D. McClung, *Chem. Phys. Lett.*, 22, 414 (1973).
103. J.C. Leicknam, Y. Guissani and S. Bratos, *J. Chem. Phys.*, 68, 3380 (1978).
104. M. Bloom, F. Bridges and W.N. Hardy, *Can. J. Phys.*, 45, 3533 (1967).
105. R.E.D. McClung, *Adv. Mol. Rel. Int. Processes*, 10, 83 (1977).
106. J. Homer, A.R. Dudley and W.R. McWhinnie, *J. Chem. Soc. Chem. Commun. No. 23*, 893 (1973).

107. P.G. King and S.N. Deming, *Anal. Chem.*, 46, 1476 (1974).
108. R.L. Streever and H.Y. Carr, *Phys. Rev.*, 121, 20 (1961).
109. Dinesh, M.T. Rogers and G.D. Vickers, *Rev. Sci. Instrum.*, 43, 555 (1972).
110. Dinesh and M.T. Rogers, *J. Chem. Phys.*, 56, 542 (1972).
111. H.T. Edzes, *J. Magn. Reson.*, 17, 301 (1975).
112. H.Y. Carr and E.M. Purcell, *Phys. Rev.*, 94, 630 (1954).
113. D.E. Woessner, *Rev. Sci. Instrum.*, 31, 1146 (1960).
114. D.M. Cantor and J. Jonas, *J. Chem. Phys.*, 28, 157 (1977).
115. E.O. Stejskal and J.E. Tanner, *J. Chem. Phys.*, 42, 288 (1965).
116. E. von Meerwall, R.D. Burgan and R.D. Ferguson, *J. Magn. Reson.*, 34, 339 (1979).
117. S. Meiboom and D. Gill, *Rev. Sci. Instrum.*, 29, 688 (1958).
118. L.A. Wolf, *J. Chem. Soc. Faraday Trans. I*, 71, 784 (1975).
119. M.A. McCool, A.F. Collings and L.A. Wolf, *J. Chem. Soc. Faraday Trans. I*, 68, 1489 (1972).

120. J.M. Le Carpentier, R. Schlupp and R. Weiss, *Acta Cryst.*, B28, 1278 (1972).
121. W.H. Flygare and J. Goodisman, *J. Chem. Phys.*, 49, 3122 (1968).
122. J.A. Ibers and J.D. Swalen, *Phys. Rev.*, 127, 1914 (1962).
123. J.A. Pople, W.G. Schneider and H.J. Bernstein, "High Resolution Nuclear Magnetic Resonance", John Wiley & Sons, Inc., New York, 1959.
124. P.B. Davis, R.M. Neuman, S.C. Wofay and W. Klemperer, *J. Chem. Phys.*, 55, 3564 (1971).
125. L. Krause and M.A. Whitehead, *Mol. Phys.*, 23, 547 (1972).
126. D.E. Woessner, *J. Chem. Phys.*, 42, 1855 (1965).
127. A.I. Andreeva, V.L. Matukhin, D.Ya. Osokin and I.A. Safin, *Sov. Phys. Solid State*, 15, 2270 (1974).
128. J.P. Jacobsen and K. Schaumburg, *J. Magn. Reson.*, 28, 191 (1977).
129. W.J. Caspary, F.S. Millet, M. Reichbach and B.P. Dailey, *J. Chem. Phys.*, 51, 623 (1969).
130. P.K. Bhattacharya and B.P. Dailey, *J. Chem. Phys.*, 63, 1336 (1975).
131. F.S. Millet and B.P. Dailey, *J. Chem. Phys.*, 56, 3249 (1972).



132. H.H. Mantsch, H. Saito and I.C.P. Smith, *Prog. NMR Spectrosc.*, 11, 211 (1977).
133. K.F. Kuhlmann and D.M. Grant, *J. Chem. Phys.*, 55, 2998 (1971).
134. J.R. Lyerla, Jr. and D.M. Grant, *J. Phys. Chem.*, 76, 3213 (1972).
135. B.K. John and R.E.D. McClung, *J. Magn. Reson.*, 50, 267 (1982).
136. D.W.G. Smith and J.G. Powles, *Mol. Phys.*, 10, 451 (1966).
137. Y. Margalit, *J. Chem. Phys.*, 55, 3072 (1971).